Limitations and advancements in soft x-ray spectroscopy

A Thesis Submitted to the
College of Graduate Studies and Research
in Partial Fulfillment of the Requirements
for the degree of Doctor of Philosophy
in the Department of Physics and Engineering Physics
University of Saskatchewan
Saskatoon

By
T. Z. Regier

Permission to Use

In presenting this thesis in partial fulfilment of the requirements for a Postgraduate degree from the University of Saskatchewan, I agree that the Libraries of this University may make it freely available for inspection. I further agree that permission for copying of this thesis in any manner, in whole or in part, for scholarly purposes may be granted by the professor or professors who supervised my thesis work or, in their absence, by the Head of the Department or the Dean of the College in which my thesis work was done. It is understood that any copying or publication or use of this thesis or parts thereof for financial gain shall not be allowed without my written permission. It is also understood that due recognition shall be given to me and to the University of Saskatchewan in any scholarly use which may be made of any material in my thesis.

Requests for permission to copy or to make other use of material in this thesis in whole or part should be addressed to:

Head of the Department of Physics and Engineering Physics
Physics Building
116 Science Place
University of Saskatchewan
Saskatoon, Saskatchewan
Canada
S7N 5C9

Abstract

Soft x-ray absorption spectroscopy (XAS) is a widely used method for probing the electronic structure of materials, yet it suffers from many complications related to the reliable measurement of absorption spectra and the proper theoretical modelling of spectral features. Problems due to different experimental aspects, such as sample charging, surface contamination and saturation effects, often introduce artifacts or distortions into a measured absorption spectrum. Even when measured accurately, the interpretation of absorption spectra is complicated by the absence of rigorous theoretical methods that properly account for the effect of the core hole on the remaining electronic structure, leading to inaccurate spectral simulations. This dissertation explores several of the limitations of soft x-ray methods and presents new data to demonstrate how these deficiencies can be overcome.

The limits of the one electron model of core excitation were explored through a high resolution XAS study of the linear polyacenes. When measured at high resolution, the linear polyacenes exhibited a fine structure that could be assigned to excitation of non-equivalent carbon atoms in the molecules. The energies and intensities of these transitions were extracted and compared to transition intensities calculated from density functional theory, where the multi-electronic effects were approximated using a full core hole and half core hole model. The full core hole model was found to better approximate the trends in the spectra for the smaller molecules, but neither model was able to properly calculate the changes in the absorption spectra of the larger molecules. These results demonstrated the deficiencies of the one electron picture of core hole excitation and highlighted the need for incorporating multi-electronic effects into XAS simulations.

To extend the capabilities of XAS, the use of partial fluorescence yields (PFY) was explored. One of the primary experimental limitation of XAS is that absorption spectra are measured by monitoring the total yield of electrons or photons from the sample. In both of these methods, a direct relationship between the measured spectra and the linear attenuation coefficient of the sample is not guaranteed. To overcome this drawback, the partial fluorescence yield measurement technique, employing a silicon drift detector, was used. By measuring partial fluorescence yields (PFY), as opposed to total yields, the effects of background fluorescence could be avoided. The inverse of the partial fluorescence yield was also demonstrated to be an effective way of avoiding saturation effects in some samples. The utility of the inverse partial fluorescence yield (IPFY) method was demonstrated in a study of several iron oxide minerals that were not possible to measure using conventional total yield methods. IPFY was also demonstrated for liquid samples where differences between the Fe PFY and IPFY were noted and attributed to resonant scattering effects in the PFY.

In both the iron oxide study and the polyacene study, the experimental limitations related to the measurement of XAS were evaluated by comparison to x-ray Raman spectroscopy (XRS). XRS is a hard x-ray based method that probes core excitation in low-Z elements by measuring the energy loss of the scattered photons. Both XRS and XAS involve the same electronic transitions allowing for a direct comparison of

spectra measured using the two methods, but the limitations of XAS related to the short penetration depth of soft x-rays are not encountered in XRS. While XRS measurements do not suffer from saturation or surface effects, the experimental resolution and count rates of this technique are limited.

This dissertation demonstrated that, while XAS is an established method, there are many aspects of the technique that require additional development. Emerging calculation methods that can incorporate the interaction between the electron and core hole will improve data interpretation capabilities. New detector systems that can measure partial yields with high resolution and can be placed in specific geometries will continue to improve measurement quality and allow for the development of novel techniques, like IPFY. A growing use of XAS and XRS in concert will also improve the general applicability of core level excitation spectroscopies and help to advance our understanding of the materials around us.

Acknowledgements

I would like to thank my supervisors, especially John Tse, for the many valuable discussions and the ongoing support with the development of the concepts in this work. I'd also like to thank all of the staff at the Canadian Light Source, past and present, for their hard work and dedication to making the facility a success. It is important to acknowledge all of the SGM user community over the past 8 years because they have all contributed to my education in one way or another. I also want to thank my entire family, especially my wife, Andrea, for the encouragement over the years.

The work presented in this thesis was performed at the Canadian Light Source which is funded by the Natural Sciences and Engineering Research Council, National Research Council, the Canadian Institutions of Health Research and other federal government agencies. Some measurements were performed at the Advanced Photon Source which is an Office of Science User Facility operated for the U.S. Department of Energy (DOE) Office of Science by Argonne National Laboratory, and is supported by the U.S. DOE under Contract No. DE-AC02-06CH11357.

To Ivan, Lucy and Physics Girl.

Contents

List of Tables

List of Figures

List of Abbreviations

SGM	Spherical Grating Monochromator
NEXAFS	Near Edge X-ray Absorption Fine Structure
SXAS	Soft X-ray Absorption Spectroscopy
XAS	X-ray Absorption Spectroscopy
DOUS	Density of Unoccupied States
PDOUS	Partial Density of Unoccupied States
LPDOUS	Local Partial Density of Unoccupied States
EY	Electron Yield
TEY	Total Electron Yield
FY	Fluorescence Yield
TFY	Total Fluorescence Yield
MCP	Micro Channel Plate
SDD	Silicon Drift Detector
LUMO	Lowest Unoccupied Molecular Orbital
XRS	X-ray Raman Scattering
EXAFS	Extended X-ray Absorption Fine Structure
DDSCS	Double Differential Scattering Cross Section
CLS	Canadian Light Source
ALS	Advanced Light Source
APS	Advanced Photon Source
NSLS II	National Synchrotron Light Source II
DCM	Double Crystal Monochromator
PMT	Photo-Multiplier Tube
STXM	Scanning Transmission X-ray Microscope
LERIX	Lower Energy Resolution Inelastic X-ray scattering
PNC	Pacific Northwest Consortium
LDA	Local Density Approximation
GGA	Generalized Gradient Approximation
PBE	Perdew-Burke-Ernzerhof
BO	Born-Oppenheimer approximation
EELS	Electron energy loss spectroscopy
BNL	Brookhaven National Lab
HCH	Half Core Hole
FCH	Full Core Hole
FEL	Free Electron Laser
LNSCO	$La_{1.475}Nd_{0.4}Sr_{0.125}CuO_4$

Chapter 1

Introduction

1.1 Overview

The electronic structure of matter determines the magnetic, electrical and chemical properties of the materials around us. The reactivity of a catalyst, the charge transfer properties of a semiconductor or the bio-availability of nutrients in soils are all direct results of electronic configuration [1–4]. Improving our understanding of many important natural systems requires experimental tools that can probe electronic arrangement. The same methods are also important in the development of novel material applications and industrial innovation.

Core level excitation spectroscopies are one powerful way in which electronic structure information can be accessed experimentally. Using a suitable excitation source, electrons from a given core level can be promoted into an unoccupied or virtual orbital with a transition probability that is highly sensitive to the configuration of the valence electrons around the atom. By recording the transition probability as a function of the source excitation energy, one obtains a fine structure or spectrum that is specific to the bonding environment of the target atom. The fine structure from an unknown material can be compared to that of well known compounds to identify the composition, a process called 'fingerprinting' [5]. The spectrum can also be compared to one that has been modelled using electronic structure calculations to evaluate the accuracy of theoretical and computational methods [6].

X-ray Absorption Spectroscopy (XAS) and X-ray Raman Scattering (XRS) are two core level spectroscopies that employ the brilliant x-ray beams produced at synchrotron facilities. In x-ray absorption spectroscopy (XAS), the energy of an incident x-ray beam is scanned across a particular electron core level binding energy for a specific element in the sample. The attenuation of the photon beam is monitored as a function of incident photon energy by recording the intensity of the beam transmitted through the sample or by measuring the intensity of secondary processes associated with the decay of the generated core holes [7]. In x-ray Raman spectroscopy (XRS), x-rays with greater energy than the core level binding energies are scattered from a sample and the intensity and energy of the scattered photons is examined. During the scattering process, some of the x-rays transfer sufficient energy to core level electrons as to transition the atom into an excited state. By measuring the intensity of the scattered photons as a function of the energy lost, a core level excitation can be recorded [8]. As shown in Fig. 1.1, the distinction between the two methods is that in XRS, the excitation occurs due to the transfer of some of the incident photon momentum to the core excited

atom, while in XAS the photon is completely absorbed. In both spectroscopic methods, it is the energy dependence in the cross section of the respective process that is used to probe the local electronic structure of the excited atom.

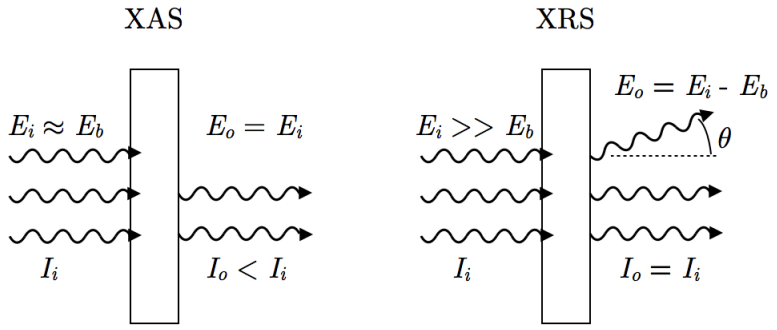

Figure 1.1: An illustration of the distinction between x-ray absorption spectroscopy and x-ray Raman spectroscopy. E_i and I_i indicate the incident energy and intensity of the photon beam and E_o and I_o indicate the energy and intensity of the outgoing photon beam. E_b represents a core level electron binding energy of the atom of interest. Θ is the angle through which an incident photon is scattered.

XAS and XRS can be particularly useful for studying electronic structure of materials with core level transitions energies from a hundred to several hundreds of eV. This energy range encompasses the binding energies of the 1s electrons in C, N and O, the 2p binding energies of the first row transition metals and the 3d electron binding energies of some of the rare earths. Core level excitation of C has been shown to be an extremely versatile method that has been used to classify organic matter in soils [9], examine the orientation of sub-monolayer organic thin films [10] and to probe the effects of high pressure on organic molecules [11]. Electronic structure studies of transition metal containing compounds, using excitation of the 2p or 3d electrons, have also been very successful. Improvements in Li battery cathodes and catalyst performance have resulted from an improved understanding of their electronic structure [12, 13]. In-situ studies of these important materials have also been performed [14].

Despite the successful application of XAS and XRS to many important scientific problems, there are numerous difficulties associated with the acquisition and analysis of core excitation data. Absorption experiments on the light elements can only be achieved through excitation with x-rays in the 100 to 1000 eV energy range, which are known as 'soft x-rays' due to their limited penetration capabilities. Performing Soft X-ray Absorption Spectroscopy (SXAS) experiments, therefore, requires that the sample as well as the entire x-ray beam path be under vacuum during measurement This makes SXAS methods incompatible with many types

of in-situ measurement apparatus. The short penetration depth also complicates the measurement of the attenuation length of the photons in the sample. As will be discussed in Chapter 2, transmission measurements are often not possible and the attenuation of the photons has to be measured by secondary processes related to the core hole decay. Using the intensities of these secondary processes, specifically electron emission and photon emission, as a probe of the attenuation length is often not straightforward and requires consideration of additional factors like sample composition and electrical properties.

XRS involves the scattering of high energy x-rays so the penetration depth of the x-rays is not a factor. The excitation energy can be chosen independently of the core level binding energy that is being probed. Typically, photon energies around 10 keV are used because they have good penetration capability and the scattering cross section is optimized. This makes XRS compatible with many sample handling apparatus like high pressure cells and equipment for in-situ measurement. But XRS also has drawbacks that limit its usefulness. As will be discussed in Chapter 2, limitations related to the instrumental resolution and signal count rates reduces the amount of spectral detail that can be extracted from the measurements.

Finally, both XAS and XRS suffer from analysis limitations related to the incomplete theoretical treatment of the core excitation process. Agreement between measured XAS/XRS spectra and those calculated using Density Functional Theory (DFT) often disagree, limiting the utility of the electronic structure models. While DFT has shown to be a reliable method for modelling ground state electronic properties, the complicated many body interactions that occur due to the strong perturbations involved in core hole formation are not properly approximated. The utility of XAS and XRS are limited by this inability to accurately calculate theoretical spectra because a direct comparison between the modelled cross section and the measurement are not possible. This issue will be explored more fully in Chapter 1.4, where calculated transition intensities and energies will be compared to the measured values for tetracene.

In this thesis, an examination of the major limitations that currently restrict the application of x-ray based core level excitation spectroscopies will be provided. The development of new methodologies related to the measurements and the analysis of core excitation spectroscopy will be presented along with relevant examples. The thesis is structured in the following manner: In the remainder of Chapter 1, the two major x-ray based spectroscopic methods, SXAS and XRS, used for electronic structure studies will be introduced. Chapter 2 presents details on the instrumentation used for the measurements in the thesis and describes some of the technical developments that were made in relation to the acquisition of soft x-ray absorption spectroscopy. Chapter 3 describes the measurement and analysis of the high resolution XAS of the polyacene series and discusses the role of the core hole on the formation of their absorption spectra. Interpretation of these spectra will be performed with the aid of calculation and the limitations of DFT with respect to the modelling of core hole effects will be examined. Chapter 4 presents the measurement of three iron oxide minerals using the inverse partial fluorescence yield (IPFY) and XRS and comments on the IPFY method, the effects of self absorption and the potential for IPFY in future XAS work. The final chapter will discuss the current standing of core level excitation spectroscopies and presents a road-map for ongoing development

of the techniques.

1.2 Soft x-ray absorption spectroscopy

The advent of x-ray absorption spectroscopy (XAS) dates back to the early 20th century when tunable x-ray sources first became available [15]. The first example of a x-ray absorption spectroscopy was provided by Wather Kossel is his 1919 paper entitled *Zum Bau der Röntgenspektren*, where the 3d to 4f transitions in uranium and thorium are shown [16]. After this, the power of XAS for studies of atomic structure was quickly recognized and a great deal of progress was made in understanding the interaction or dispersion of light by matter. But it wasn't until the 1960's, when synchrotron light sources that could produce intense and tunable x-rays were developed, that the material characterization capabilities of XAS were harnessed in a wide variety of scientific disciplines. Since that time, the fine structure in absorption spectra has been shown to be an invaluable tool for the study of electronic, magnetic and chemical properties.

In this chapter, a theoretical description of the x-ray absorption process will be provided and the crucial parameter, the linear attenuation coefficient, will be defined. Using the quantum mechanical treatment of the photo-excitation process, the density of unoccupied states in a material will be shown to be uniquely related to its x-ray absorption cross section. The definition of the cross section will then be used to show how electronic structure information is intimately connected to attenuation of x-rays in the material. Finally, these concepts will be used to show how the features in an x-ray absorption spectrum can be interpreted to determine oxidation state, crystal symmetry and molecular orientation.

1.2.1 The absorption cross section and the linear attenuation coefficient

An x-ray absorption spectroscopy experiment involves the measurement of the energy dependence of the linear attenuation coefficient, $\mu(E)$, of a solid, liquid or gas sample. $\mu(E)$ is related to a property of the atoms in the sample called the absorption cross section, $\sigma(E)$, which is defined as the ratio of the power absorbed by an atom to the incident power per unit area. The absorption occurs due to the interaction between the radiation field and the electrons in the sample through the excitation of the system from an initial quantum state i to some final state f. Probing $\mu(E)$ provides information on the local electronic environment of the atoms in the sample, specifically the energy difference between i and f and the density of the unoccupied states in f. While it is the density of unoccupied states in the core excited system that is probed by XAS, details on the ground state, such as the oxidation state or crystal environment, can often be determined by comparison between the measurement and calculation or by comparison with the absorption spectra of standard compounds.

The relationship between the absorption cross section (and hence the linear attenuation coefficient) and electronic structure can be defined quantum mechanically. Using first order perturbation theory, Dirac [17]

described the probability of exciting an electronic transition from state i to state f by

$$P_{i\to f} = \frac{2\pi}{\hbar} \left|\langle i \left| H' \right| f \rangle\right|^2 \delta(E_f - E_i - \hbar\omega), \tag{1.1}$$

where H' is the perturbing Hamiltonian

$$H' = H_o + V(t). \tag{1.2}$$

Here, H_o is the ground state Hamiltonian and $V(t)$ is a time dependent perturbation due to the incident electromagnetic wave.

For a plane wave with a unit vector $\mathbf{e}$, the vector potential $\mathbf{A}$ is

$$\mathbf{A} = \mathbf{e}\frac{A_o}{2}\left(e^{i(\mathbf{k}\cdot\mathbf{x}-\omega t)} + e^{-i(\mathbf{k}\cdot\mathbf{x}-\omega t)}\right), \tag{1.3}$$

and the time dependent perturbation can be written as

$$V(t) = \frac{e}{mc}\sum_i \mathbf{A}\cdot\mathbf{p}_i, \tag{1.4}$$

where $\mathbf{p}_i$ is the linear momentum operator of the ith electron.

Substitution of Eqs. 1.4 and 1.3 into Eq. 1.1 gives

$$P_{i\to f} = \frac{\pi e^2}{2\hbar m^2 c^2}\left|A_o\right|^2 \left|\left\langle i \left| e^{i\mathbf{k}\cdot\mathbf{x}}\mathbf{e}\cdot\mathbf{p}\right| f\right\rangle\right|^2 \delta(E_f - E_i - \hbar\omega). \tag{1.5}$$

Only the $e^{-i\omega t}$ term in Eq. 1.3 is considered in the case of absorption spectroscopy because it describes the removal of radiation from the electric field. For soft x-ray excitation, the wavelengths are long compared to the size of the electron orbitals and so the electric field can be considered constant over the spatial distribution of the excited electrons ($\mathbf{x} \ll \lambda/2\pi$). This allows for the application of the dipole approximation, $e^{i\mathbf{k}\cdot\mathbf{x}} = 1$, which simplifies the transition probability to

$$P_{i\to f} = \frac{\pi e^2}{2\hbar m^2 c^2}\left|A_o\right|^2 \left|\langle i \left|\mathbf{e}\cdot\mathbf{p}\right| f\rangle\right|^2 \delta(E_f - E_i - \hbar\omega). \tag{1.6}$$

The absorption cross section, σ, which was defined as the amount of energy absorbed per unit area per unit time over the amount of energy incident per unit area per unit time, can be related to the transition probability through

$$\sigma(\omega) = \frac{P_{i\to f}}{\Gamma}, \tag{1.7}$$

where

$$\Gamma = \frac{A_o^2\omega}{8\pi\hbar c}, \tag{1.8}$$

is the number of incident photons per unit time per unit area. Substitution of Eqs. 1.6 and 1.8 into Eq. 1.7 gives

$$\sigma(\omega) = \frac{4\pi e^2}{m^2 c\omega}\left|\langle i \left|\mathbf{e}\cdot\mathbf{p}\right| f\rangle\right|^2 \delta(E_f - E_i - \hbar\omega), \tag{1.9}$$

In a soft x-ray absorption experiment $\sigma(\omega)$ is measured by monitoring the attenuation of a monochromatic x-ray beam in a material as a function of energy. For an incident beam with intensity I_o, the x-ray intensity as a function of depth into the medium is given by the Beer-Lambert law:

$$I(x,\omega) = I_o e^{-\mu(\omega)x}. \tag{1.10}$$

The linear attenuation coefficient, $\mu(\omega)$, can, in turn, be related to $\sigma(\omega)$ through

$$\mu(\omega) = \sigma(\omega)\frac{\rho N_A}{m_a} \tag{1.11}$$

where m_a is the atomic molar mass and N_A is Avogadro's number. It is important to note that $\mu(\omega)$ is the *total* linear attenuation coefficient, which is the sum of the linear attenuation coefficients of all of the components of the material such that

$$\mu(\omega) = \mu_A(\omega) + \mu_B(\omega) + \ldots. \tag{1.12}$$

For compounds and mixtures it is often more useful to evaluate the mass absorption coefficient, which is simply $\mu(\omega)\ \rho$. Tabulated values for the mass absorption coefficients of most elements are available from [18].

1.2.2 Interpretation of soft x-ray absorption spectra

In general, the energy dependence of μ has three distinct regions as shown in Fig. 1.2: the pre-edge, near-edge and post-edge. The pre-edge region represents the portion of the spectra where $\hbar\omega$ is less than the binding energy of the core level electrons. In this region the excitation of valence electrons and outer core electrons into the continuum result in a relatively small and slowly decreasing value for μ. The near-edge region, often called the X-ray Absorption Near Edge Structure (XANES), begins as $\hbar\omega$ becomes close to the binding energy of the core level electrons, E_{core}, and the excitation of the atom from the ground state i into a core hole excited state f is possible. In this region, μ strongly varies with photon energy with a structure that mimics $\rho'(E_f)$, the core hole modified density of unoccupied states (DOUS). In the post-edge region, where $\hbar\omega$ exceeds the binding energy of the core electrons, direct photoionization is possible the final state corresponds to a core excited atom with an electron ejected from the atom. μ is once again slowly decreasing with increasing energy but exhibits slight oscillations due to interference between the ejected photo electron and the photo electrons scattered by neighbouring atoms. This is known as the extended x-ray absorption fine structure (EXAFS) and can be used to determine the number of scatter atoms, their proximity to the target atom and, given data of sufficient quality, the atomic number of the scattering atoms [19].

While EXAFS on low Z elements has been shown to be useful for certain studies [20], the acquisition of accurate post-edge measurements at soft x-ray energies is experimentally challenging and the technique is not commonly used for low Z atoms. The primary reason for this is that the scattering of photoelectrons from the light atoms is much weaker than it is for the heavier elements, resulting in EXAFS oscillations with a smaller amplitude, which are harder to measure. In addition, electronic transitions from other low Z elements are not well separated in energy so it is not always possible to collect EXAFS with a sufficient range. Because the reliability of the EXAFS analysis relies heavily on obtaining data with a high signal to noise ratio, as well as acquiring a large energy range, in many cases it is not a feasibly technique for low Z atoms.

To obtain local electronic structure information using soft x-ray absorption the near-edge or XANES region of the spectrum is generally more valuable then the EXAFS. Soft x-ray XANES tend to show a much finer

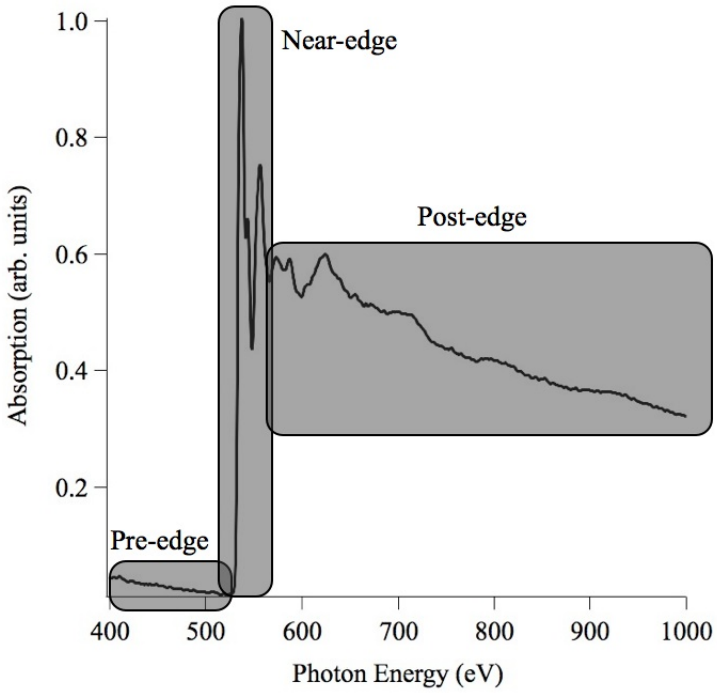

Figure 1.2: The oxygen x-ray absorption spectrum on ZnO.

structure than hard x-ray XANES due to the reduced lifetime broadening encountered in the measurement. The core hole lifetime and transition energy exhibit an uncertainty relationship resulting in the Lorentzian broadening of the discrete transitions that make up the absorption spectrum. The 1979 work by Krause and Oliver showed that this lifetime broadening increases with the square of Z [21][1]. Consequently, XANES spectra taken with soft x-rays show much less lifetime broadening and are able to resolve much finer spectral detail than those taken with hard x-rays. The additional fine structure can be useful when 'fingerprinting' a sample for spectral comparison with known materials and the high resolution features are also important when comparing measured spectra to those simulated using core excitation calculates. Fine details are often critical when evaluating the merits of one model versus another, as will be discussed further in Sec. 3.

Photo-absorption can occur due to excitation of electrons from different core level electrons in an atom, giving rise to the K, L, M and N edges. The K edge, corresponding to excitation of the n=1 electrons, typically consists of a strong single peak with some fine structure, as shown in Fig. 1.2. The L, M and N edges, corresponding to excitations from the n=2, 3 and 4 electrons and show distinctly split peaks. This splitting, shown in Fig. 1.3 for the Ce M edge of CeO_2, arises due to interaction between the electron spin and the magnetic field caused by the electron's motion around the nucleus. Aside from the obvious effects of spin orbit coupling, the L, M and N-edge absorption spectra differ from the K-edge spectra because different

[1]The Z^2 relationship holds for excitation of the $n = 1$ level only. It is decreased for excitation of the less tightly bound core levels due to improved screening of the nuclear charge by the remaining electronic structure.

selection rules govern the excitation process for p, d and f electrons[2].

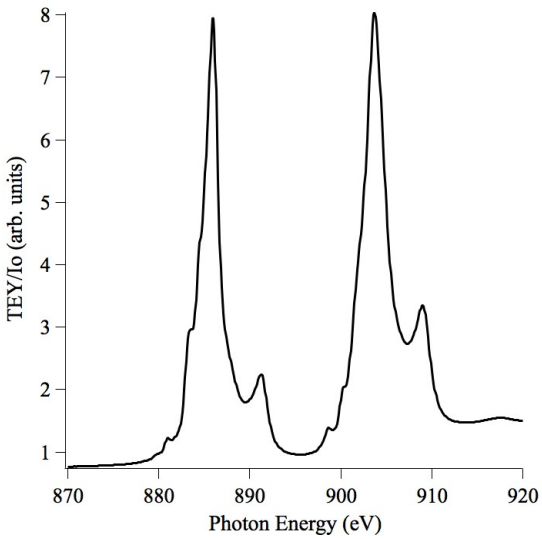

Figure 1.3: The M-edge XANES of CeO_2.

Soft x-ray excitation can be used to probe the L and M-edges of the transition metals, and the M and N-edges for the lanthanides and actinides. The excitation of 2p electrons into the unoccupied orbitals of d type symmetry, in conjunction with ligand field theory, has been demonstrated to be an indispensable tool for probing bonding in the transition metal complexes [6]. This method will be demonstrated in Chapter 4, where the ability to distinguish oxidation state and co-ordination geometry of the iron oxides using the L-edge will be discussed. Investigation of the chemical environment in lanthanide and actinide complexes through M and N-edge studies is also an important capability provided by soft x-rays. Hard x-ray absorption studies of these systems often do not show the detail available in the soft x-ray absorption spectra due to the limited spectral resolution available and because excitation from the 1s orbitals into the orbitals with d symmetry is forbidden. Similar effects are seen in the actinides and lanthanides, where transitions into the unfilled f-orbitals can be studied at high resolution with soft x-ray absorption spectroscopy.

An example of how x-ray absorption spectroscopy can be utilized to determine oxidation state, and electronic spin state can be found in the article by Wadati et. al. [22] on the electronic structure of $LiMnO_2$ and similar structure with Cr and Ni substituted for the Mn. These materials have layered structures that make them suitable candidates for use as electrodes in Li based rechargeable batteries. The valence states and local electronic configurations of the transition metals are highly relevant to the charge-discharge rates of batteries generated from these materials. Wadati et al. measured the absorption spectra of $LiMn_{0.5}Ni_{0.5}O_2$,

[2]The value of the transition operator will vanish if the symmetry of the transition moment function is symmetric with respect to the origin. In absorption spectroscopy, the angular momentum must be transferred from the absorbed photon to the excited atom, meaning the angular momentum of the initial state must differ from that of the ground state for the transition operator to be non-zero.

$LiMn_{0.65}Cr_{0.35}O_2$ and $LiMnO_2$ at the Mn, Cr and Ni L-edges and compared their measurements to previously measured standards with known oxidation states.

At the Mn L-edge, the incident x-rays are tuned across the Mn 2p electron binding energy, exciting electrons from the p orbitals into unoccupied d orbitals. These electronic configuration of these d orbitals are sensitive to both the oxidation state of the Mn, but also the degree of interaction with the O p orbitals in the structure. When the absorption spectra of the battery materials are compared to the spectra of Mn containing compounds with known oxidation state, a strong similarity between the absorption signature of the Mn^{4+} compound is observed. Similar tests at the Ni and Cr L-edges showed their oxidation states to be 2+ and 3+, respectively.

The work by Waditi et al. is just one example of how absorption spectroscopy can be used to identify the oxidation state of unknown transition metal compounds. The ability to probe the electronic structure of the partially unoccupied 3d orbitals, which are highly sensitive to the crystal symmetry and oxidation state, make the technique quite powerful. High resolution capabilities are also important here: more well defined structure that is observed in the measurements results in a more confident comparison to the spectra of reference compounds. The value of the high resolution structure will be highlighted in Chapter 3, where the high resolution XAS of the polyacenes will be presented. Comparision of the Fe L-edge XAS of ferrihydrite, a nanocrystalline iron oxy-hydroxide, and known iron oxides will also be used in Chapter 4 to determine the crystal environment of the Fe in ferrihydrite.

1.3 X-ray Raman scattering

In 1928, C.V. Raman and K.S. Krishnan published a very short article entitled "A new type of secondary radiation" wherein they detailed the observation of scattered light that, unlike the normal diffuse scattering, is shifted in wavelength from the incident radiation [23]. They determined two important things about the new type of radiation. The first was that the shift was constant regardless of the wavelength of the incident radiation used. The second was that the magnitude of the shift was dependent on the scattering material. It was apparent that some portion of the incident light was losing energy to the excitation of the sample through the process of being scattered.

This type of inelastic scattering, which became known as Raman scattering, had been predicted in 1923 [24] and quickly became an important tool for the study of chemical composition. The true value of Raman scattering lay in the fact that you could use the scattering of one wavelength of light to get information from the sample that was previously only obtainable with another. The typical applications involved using an optical laser as an excitation source and looking for wavelength shifts in the scattered light that corresponded to the excitation of vibrational modes in the sample. By using inelastic scattering one could use optical light to investigate properties typically associated with infrared absorption.

In the 1960's the Raman effect was first observed at x-ray wavelengths [25]. This was primarily due

to the fact that the in-elastic scattering cross section for x-ray wavelengths was so small that it required a very intense light source and a good detection efficiencies. It was quickly determined that, for X-ray Raman Scattering (XRS), the energy shift in the inelastically scattered x-rays corresponded to the core level binding energies. Subsequent investigation showed that information analogous to the information provided by x-ray absorption spectroscopy, could indeed be obtained using XRS [26]. This was a substantial discovery because it indicated that some of the restrictions associated with soft x-ray measurements, such as the vacuum requirements and preclusion of certain *in-situ* apparatus, could be overcome. In particular, questions related to the surface sensitivity of SXAS could be answered with XRS, which is undeniably bulk sensitive.

In this section, a basic overview of XRS theory will be provided. The specific focus will be on how the data obtained from an XRS experiment can be compared to XAS data obtained from the same sample. This will be used to interpret the IPFY and XRS data for the iron oxide minerals in Sec.4. If the reader wishes to study XRS in more detail, they are invited to examine the book by Schülke [8] which provides an excellent review of the technique and recent applications.

1.3.1 The Kramers-Heisenberg equation

In 1925, Kramers and Heisenberg modelled the dispersion of photons in matter as a second order optical process and developed an equation that relates the intensity of photon scattering as a function of the incident and scattered photon energies [27]. The Kramers-Heisenberg equation was able to predict the observation of both elastic scattering, where the energy of the incident and scattered photons are the same, and in-elastic scattering, where the scattered photon can have more or less energy than the incident photon. This section will briefly introduce the Kramers-Heisenberg equation and describe its relation to XRS. It will also be useful in our later discussion of the fluorescence yields in XAS in Sec.2.3.3 where the fluorescence efficiencies are concerned.

For an incident photon of energy $\hbar\omega_a$ with wavevector k_a scattered off of an atom into some solid angle Ω_b, where the scattered photon has energy $\hbar\omega_b$ and wavevector k_b, the Kramers-Heisenberg equation gives the cross section as the following [6]:

$$\begin{aligned}\frac{d\sigma^2}{d\Omega d\hbar\omega_b} &= r_o^2 \frac{\omega_a}{\omega_b} \sum_j \delta\left(E_g + \hbar\omega_a - E_j - \hbar\omega_b\right) \left|\langle j \left|\rho_{k_a - k_b}\right| g\rangle (\mathbf{e_a} \cdot \mathbf{e_b})\right. \\ &+ \frac{1}{m} \sum_i \left(\frac{\langle j|\mathbf{p}(\mathbf{k_b})\cdot\mathbf{e_b}|i\rangle\langle i|\mathbf{p}(-\mathbf{k_a})\cdot\mathbf{e_a}|g\rangle}{E_i - E_g - \hbar\omega_a} + \frac{\langle j|\mathbf{p}(\mathbf{k_b})\cdot\mathbf{e_b}|i\rangle\langle i|\mathbf{p}(-\mathbf{k_a})\cdot\mathbf{e_a}|g\rangle}{E_i - E_g + \hbar\omega_a} \right) \Bigg|^2 . \end{aligned} \tag{1.13}$$

This is the double differential cross section, defined as the probability that an incident photon with energy $\hbar\omega_i$ and wavevector k_i will be scattered with energy $d\hbar\omega_f$ and detected in the solid angle $d\Omega$. Here $|g\rangle$, $|i\rangle$ and $|j\rangle$ are the initial, intermediate and final states of the scattering medium, E_g, E_i and E_j are their energies and $\mathbf{e_a}$ and $\mathbf{e_b}$ are the polarization unit vectors of the incident and emitted photons. The transition operators contain the terms $p(k)$, defined as

$$\mathbf{p}(\mathbf{k}) = \sum_n \mathbf{p}_n e^{-i\mathbf{k}\cdot\mathbf{r}} \tag{1.14}$$

and ρ_k, defined as

$$\rho_k = \sum_n e^{-i\mathbf{k}\cdot\mathbf{r}}. \tag{1.15}$$

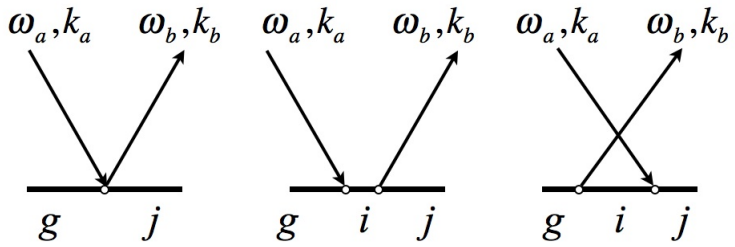

Figure 1.4: The three possible processes involved in photon scattering as described in the Kramers-Heisenberg equation. In the first, the photon is elastically scattered without transferring energy with the atom. In the second and third, energy is transferred into and out of the scattered photon, respectively.

The Kramers-Heisenberg equation describes all possible outcomes for photon in-photon out spectroscopies. Resonant x-ray emission spectroscopy (RXES) and Resonant in-elastic x-ray scattering (RIXS) involve the scattering of photons through the excitation of intermediate states in a sample. For these methods, excitation energies are chosen to resonantly populate the intermediate states. Fluorescence yield based XAS is also governed by this the Kramers-Heisenberg equation, although the resonance effects are often overlooked. This will be examined further in Sec. 2.3.3 and Sec. 4.3.2.

XRS, in contrast to XAS, RXES and RIXS, involves using excitation energies much greater than the resonant excitation energies, where the terms in the sum over i become negligible. In this regime ($\hbar\omega >> E_i - E_g$), only the first term in Eq. 1.13 is important and the scattering is known as Thomson scattering. Under these conditions the scattering intensities are determined by a property of the scattering system known as the dynamic structure factor. As will be discussed in the following section, the dynamic structure factor is useful probe of the electronic structure of a system and provides information analogous to x-ray absorption spectroscopy.

1.3.2 The dynamic structure factor

The dynamic structure factor is the spatial and temporal Fourier transform of a two-particle density correlation function and relates the electron density at time $t = 0$, to the electron density at some later time $t > 0$ [28]. Making use of the fluctuation dissipation theorem, which relates fluctuations in a system to applied perturbations, the structure factor can be expressed a transition matrix element summed over all possible initial and final states

$$S(\mathbf{q},\omega) = \sum_{i,f} p_i \left| \left\langle f \left| \sum_j e^{i\mathbf{q}\cdot\mathbf{r}_j} \right| i \right\rangle \right|^2 \delta(E_f - E_i - \hbar\omega), \tag{1.16}$$

where p_i is the probability of the initial state $|i\rangle$. So within the time correlation formalism, the inelastic scattering of an x-ray can be viewed as a perturbation to the ground state of a system that results in a modification of the electron density which can take the form of plasmon excitation, valence electron excitation or core level electron excitation.

To access $S(\mathbf{q},\omega)$ experimentally, a measurement of the scattering intensity into well defined solid angle Ω is required. It is also necessary to know the energy, $\hbar\omega$, of the scattered photons so that the momentum transfer $\mathbf{q}$ can be calculated. This is shown in Fig. 1.5. If these conditions are met, the double differential scattering cross section (DDSCS)

$$\frac{d^2\sigma}{d\Omega_2 d\hbar\omega_2} = \left(\frac{d\sigma}{d\Omega}\right)_{Th} S(\mathbf{q},\omega), \tag{1.17}$$

can be generated, where

$$\left(\frac{d\sigma}{d\Omega}\right)_{Th} = \frac{e^2}{mc}(\mathbf{e}_1\cdot\mathbf{e}_2)^2\left(\frac{\omega_2}{\omega_1}\right) \tag{1.18}$$

is the Thomson scattering cross section. Substitution of 1.16 in to 1.17 gives

$$\frac{d^2\sigma}{d\Omega_2 d\hbar\omega_2} = \left(\frac{d\sigma}{d\Omega}\right)_{Th} \sum_{i,f} p_i \left|\left\langle f \left| \sum_j e^{i\mathbf{q}\cdot\mathbf{r}_j} \right| i \right\rangle\right|^2 \delta(E_f - E_i - \hbar\omega). \tag{1.19}$$

The experimental setup for measuring the DDSCS and other experimental considerations will be discussed in Sec.2.4.

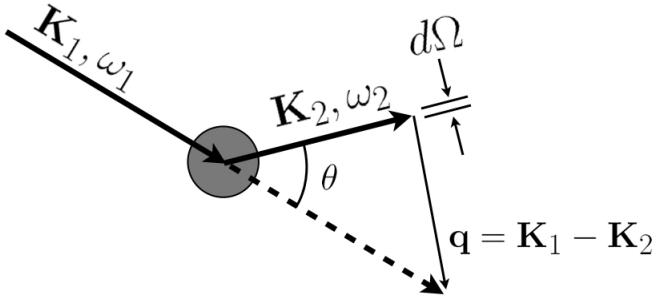

Figure 1.5: A vector diagram showing the momentum transfer $\mathbf{q}$, resulting from inelastic scattering. The incremental acceptance angle $d\Omega$ is also indicated.

The similarity of the DDSCS as expressed in Eq. 1.19 and the XAS cross section in Eq. 1.9 is clear. In both cross sections, the same energy conservation rule applies and the transition matrix elements are similar.

The two things making the matrix elements different are: a) the polarization vector ϵ in 1.9 has been replaced by the momentum transfer. $\mathbf{q}$ in 1.19 b) the dipole approximation has been applied to the XAS cross section where $\epsilon \cdot \mathbf{r}$ is always small.

Unlike SXAS, the conditions required for the dipole approximation ($\mathbf{q} \cdot \mathbf{r} \leq 1$) are not always met in XRS experiments. Depending on the selection of Ω, the momentum transfer $\mathbf{q}$ can be adjusted. For small scattering angles, $\mathbf{q} \cdot \mathbf{r}$ is small and the dipole rule applies. For large scattering angles, $\mathbf{q} \cdot \mathbf{r}$ becomes large and the expansion of the exponent in the transition matrix has to include the quadrupolar terms. This is an important distinction between XAS and XRS. In XRS, the experiment can be configured so that the quadrupole terms can be included or suppressed. This allows for measurement of $S(\mathbf{q}, \omega)$ with and without contribution from dipole forbidden transitions, providing a way to probe the symmetry of the DOUS.

1.4 Electronic structure calculation

The analysis of x-ray absorption data is often enhanced by the comparison of the measured spectra to one that has been simulated using electronic structure calculations. In many cases, this process facilitates a more complete assignment of spectral features than an analysis based on comparison to measured standards. Agreement between measurement and calculation can often be used as confirmation of a particular structure or electronic configuration, greatly enhancing the scientific impact of the measurement.

DFT has become one of the most commonly applied calculation methods for theoretical investigations because of its success in modelling ground state electronic structure in molecules and solids. In DFT, the multiple independent wave functions of interacting electrons are replaced by a single functional of the electron density, reducing the number of unknown spatial co-ordinates in an N electron system from 3N to 3. This simplification is justified because, as shown by Hohenberg and Kohn in 1964, the ground state properties of an electronic system can be uniquely described by a electron density functional [29]. Moreover, the work by Hohenberg and Kohn showed that the energy of the system could also be defined as a functional of the electron density, which was minimized for the correct ground state electron density. This meant that, using an initial guess as a starting point, the electronic structure could be calculated using an iterative procedure that minimized the energy of the system.

One of the primary difficulties encountered in all electronic structure calculations is the proper treatment of the multi-electron effects. Within the DFT framework, all many body interactions are grouped into a single term in the Hamiltonian called the exchange-correlation potential, V_{XC}. While V_{XC} is known for the free electron gas, it can only be approximated for molecules and solids. Proper approximation of V_{XC} has a large effect on the reliability of electronic structure calculations.

The two most common approximation are the local density approximation (LDA) and the generalized gradient approximation (GGA). In LDA, the exchange term at a position $\mathbf{r}$ is equal to that of a free electron gas of the same density at $\mathbf{r}$. GGA includes the gradient of the electron density in an attempt to incorporate

the effects of inhomogeneities in V_{XC}. GGA has been incorporated into the revised Perdew-Burke-Ernzerhof (PBE) exchange model which is used in the calculations found in Sec. 3.

The approximations used in the estimation of the exchange-correlation potential can often be accurate for the calculation of ground state properties but they do not properly account for the many body interactions that are expected in a core excited atom [30–32]. This causes problems in the simulation of x-ray absorption spectra where multi-electron excitations, collectively described as shake-up, are known to affect transition energies and intensities. If the excitation energies are well above the electron binding energies, as is the case for photoemission or EXAFS measurements, the core hole screening effects may be modelled within the one electron picture, where the remaining electronic structure is allowed to relax around the core hole. This is referred to as the sudden approximation. But when the excitation energy is tuned near the resonance absorption energy, such as in an x-ray absorption experiment, the excited electron energy is small, allowing it to interact more strongly with the remaining electrons in the atom and the core hole. In this case, the V_{CX} is large and the exchange-correlation energy is not properly represented by the GGA.

The lack of a suitable exchange-correlation model means that DFT can never properly account for the multi-electronic effects that occur upon core excitation. But core hole screening effects can be estimated by allowing for relaxation of the electronic structure around a core hole that is partially occupied. While this model does not incorporate any of the many body effects (it is still based on the one electron picture and the sudden approximation), it has shown some success in improving agreement between measured and simulated SXAS. As will be shown in Sec. 3, the Half Core Hole (HCH) and Full Core Hole (FCH) approximations can be used to produce simulated spectra that can help in the assignment of spectral features. These methods allow for the relaxation of the electronic structure in the final state around the fully vacant core hole or a core hole with a half electronic charge. While the HCH method is certainly not physical, it corresponds to the Slater transition state method for determining ionization potentials. But overall, the results highlight the need for caution when using theory to simulate fine structure.

Another effect that is not captured in the DFT calculations used in this thesis is the effect of inter-nuclear vibrations on the absorption cross section. Vibronic excitations occur as a result of the coupling of the nuclear and electronic degrees of freedom and result in a series of sidebands on the high energy side of the adiabatic transition in an absorption spectrum. Typical vibrational energies are in the tens to hundreds of meV so they are only apparent in SXAS when measuring at high resolutions. While it is possible to approximated the vibronic structure through calculation of the Franck-Condon factors, this capability is not part of most electronic structure codes and was not used for the calculations in this thesis. The result is that only the adiabatic transition energies and intensities are captured in the included calculations.

Lastly, the effects of lifetime broadening and instrumental line broadening are not explicitly calculated from DFT. These effects are typically estimated and then incorporated into the discrete calculation results using a convolution procedure. Lifetime broadening results from the required uncertainty in the measurement of the energy of an electronic transition into a short lived excited state. Instrumental broadening is introduced

due to the finite bandwidth produced by excitation sources.

The broadening of calculation results will often help facilitate the comparison of calculation results and measured spectra. This is particularly true when there are a large number of transitions in a very narrow energy band. Without broadening, these transitions may appear much less significant than after broadening. But in some cases, broadening is not helpful and can make comparison between theory and measurement more difficult. When there are only a few, well spaced transitions, in a sample where vibronic effects are expected to be significant, broadening is not meaningful. In these cases, comparison between the measurement and the discrete transitions can be more effective.

1.5 Conclusions

In this chapter two methods for measuring core level excitation spectra were introduced. The first section showed that the absorption of photons occurs with a probability that is determined by the electronic structure of the absorbing medium. If the absorption can be measured as a function of the energy of the incident photons, the absorption spectrum can be constructed and can be analyzed to determine features of the electronic structure such as the oxidation state and crystal structure. The second section showed that the same information that is captured in an absorption spectrum can also be found in the intensity distribution of inelastically scattered hard x-rays. This occurs because hard x-rays that undergo inelastic scattering can transfer energy into the sample that can excite the same core to bound state transitions as those involved in direct photo-absorption.

The distinctions between the two measurement methods have also been discussed in this chapter. While both methods use beams of intense x-rays to generate their spectra, the x-ray energies involved are very different. Each method has its advantages and drawbacks that stem from the excitation energy used and the relative cross sections of the two excitation processes involved. The following chapter (2) will discuss details related to the measurement of XAS and XRS spectra and the differences in the two methods will become even more apparent. Then in Chapter 4, a direct comparison between XAS and XRS will be performed.

The DFT method for calculation of core level excitation spectra was briefly outlined in this section. DFT methods are very useful for assignment of absorption spectra but the assumptions used accounting for the excited states involved in core excitation introduce error into the transition intensities and energies that may be important in the analysis of XAS and XRS data. Tests of the limits of these assumptions are important and will provide valuable reference for more modern calculations that implicitly take core hole interactions into account. These concepts will be expanded on in Chapter 3.

Chapter 2

Instrumentation and methods

2.1 Introduction

In this chapter the instrumentation and specific methods used in the measurement of XAS and XRS will be discussed. The chapter is divided into three main sections that discuss the generation of x-rays and the measurement of the principle observable quantities in each of the respective techniques.

Both XAS and XRS require the intense and tunable x-ray beams generated using synchrotron storage rings so some discussion of the the operation of these facilities will be provided. A description of the instrumentation required to take the x-rays produced in the synchrotron storage rings and prepare them for measurement is included. This will involve a description of beamline 11ID-1 at the Canadian Light Source (CLS) and beamline 20ID at the Advanced Photon Source (APS), where the measurements shown in Chapters 3 and 4 were performed.

For XAS measurements, the quantity of interest is the linear attenuation coefficient, which is effectively the energy dependence of the penetration depth of the incident x-ray beam. For XRS, the measurement of the double differential cross section, or the intensity of scattered x-rays as a function of both energy and scattering angle, is required. This chapter attempts to summarize the important factors involved in the measurement of these two quantities as the technical challenges associated with both methods.

In addition, this chapter will also contain details of instrumentation development done for XAS measurements on 11ID-1 at the CLS. Since 2003 I have served as a staff member on this beamline and I have been privileged to be involved in many technical projects that have greatly improved the measurement capabilities of this facility. A description of the key advancements made to the sample handling infrastructure, operational procedures and detection methods will be provided. The instrumentation involved in the measurement of XRS will also be discussed, but in much less detail.

Of primary importance in this chapter is the description of the use of silicon drift detectors for the measurement of XAS using partial fluorescence yields. This development has already led to many exciting discoveries that were previously not possible using the standard XAS detection methods. Another important development included in this thesis is the development of a fast scanning mode for the beamline which is important for optimizing beamline efficiency. The discussion of these and other technical aspects of XAS are important as the highlight the issues associated with properly measuring core level excitation spectra.

2.2 X-ray generation and preparation

2.2.1 Synchrotron storage rings

Synchrotrons make the ideal excitation light source for XAS and XRS experiments. They use the acceleration of high energy electrons produce extremely brilliant light over a wide photon energy range, from the infra-red to the hard x-ray wavelengths. Modern synchrotrons are equipped with devices called wigglers and undulators, which are able to increase the brightness of the radiation by several orders of magnitude. There are many excellent resources that can provide details on synchrotron operational principles and characteristics, so this information is not contained as part of this thesis [7, 33–35].

The XAS measurements shown in this thesis were performed at the Canadian Light Source (CLS) synchrotron on the University of Saskatchewan campus in Saskatoon, Saskatchewan. The CLS is a third generation light source commissioned in 2003 and 2004 [36]. At the CLS, electrons are accelerated to 2.9 GeV in a linear accelerator and booster ring, then injected into a 171 m circumference storage ring. 250 mA of beam are stored in an injection cycle with a $1/e$ lifetime of around 25 hours. The stored beam has an emittance of 18.2 nm-rad, making it suitable as a source for SXAS when combined with the appropriate beamline.

XRS measurements require an x-ray source with substantially different characteristics than a source for XAS so the XRS measurements for this thesis work were performed at the Advanced Photon Source (APS) at Argonne National Laboratory (ANL) in Argonne Illinois. The preferred photon source for XRS is a synchrotron with an undulator or wiggler insertion device, a high stored electron beam energy (>5 GeV) and a low emittance. This type of source provides a high brilliance (photons per 0.1% bandwidth, per second, per mm^2, per $mrad^2$) at 10 keV, maximizing count rates for a given spectral resolution setting. Small storage rings like the Canadian Light Source (CLS) or the Advanced Light Source (ALS) could be used for XRS, but the larger rings like Spring-8, the Advanced Photon Source (APS) or the National Sychrotron Light Source II (NSLS II) are preferred. Storage rings with larger circumferences can be built using bending magnets with lower magnetic fields, resulting in less disruption to the electron beam (betatron oscillations), and a lower overall emittance [33]. These large rings also operate at higher electron energies (7.5 GeV), giving them better performance at 10 keV.

2.2.2 Beamlines

Synchrotron light has to be filtered and focused for used in an absorption experiment. The instrumentation required for this purpose is known as the 'beamline' and consists of a series of apertures and x-ray optics as well as the vacuum chambers and beam pipes that contain them. Because of the wavelengths involved, soft x-ray beamlines use diffraction gratings to disperse the 'white' light coming from the synchrotron. An aperture, placed between the grating and the sample position, defines the photon energy E, and the bandwidth ΔE, that passes to the sample. Using this arrangement, E can be selected by changing the angle of incidence

of the light on the grating and ΔE can be selected by opening or closing the aperture. This arrangement of apertures (an entrance aperture should be placed between the synchrotron and the diffraction grating to define the source) and a grating is called the beamline monochromator. The positions of the grating and the slits, as well as the grating line spacing and/or curvature, are determined from the well known Rowland circle geometry. There are several well established monochromator designs based on these concepts [37–39].

The most important performance criteria of a monochromator is the resolving power as it determines the instrumental resolution of the spectra acquired on the beamline. The resolving power, $R = E/\Delta E$, characterizes how well the beam is filtered by the monochromator, or more specifically, the energy bandwidth of the photons that are incident on the sample. The level of detail that can be extracted from an absorption spectrum is determined, in part, from R. In order to resolve the fine structure in a spectrum, the photon bandwidth ΔE has to be smaller than the energy difference between the spectral features that are being probed.

Beamline 11ID-1 at the Canadian Light Source

The beamline used for the SXAS in this thesis was beamline 11ID-1 at the CLS. This beamline is also known as the Canadian Dragon and commonly referred to as the SGM (spherical grating monochromator) beamline. The SGM beamline design utilizes spherically polished diffraction gratings to focus x-rays through a movable exit slit [37]. The Canadian Dragon uses three selectable gratings to provide highly monochromatic x-rays in the energy range of 250 to 2000 eV (0.6 to 5 nm). The optical layout of the beamline is shown in Fig. 2.1. Two independent endstation areas are arranged in-line, each with its own measurement chamber. The first endstation area houses an X-ray Photo-electron spectrometer (SES-100) in a UHV chamber and the second endstation area houses the absorption chamber. It is possible to easliy remove the absorption endstation so that other endstations can be accommodated. The beamline is able to produce highly monochromatic light with a resolving power greater than R=12000 at the N K edge [40]. Excellent high resolution performance, in excess of $R = 12000$, has been demonstrated for CO gas and tetracene at the C K edge [41]. This capability makes the Canadian Dragon ideal for applications requiring the resolution of fine structure in absorption spectra. A great deal of the instrumentation development described in this thesis took part on this beamline.

Beamline 20ID at the Advanced Photon Source

The XRS measurements in this thesis were performed on the insertion device beamline of sector 20 at the APS. This beamline employs a liquid nitrogen cooled double crystal monochromator with a fixed exit slit. Photon energies between 3 and 55 keV can be achieved using the Si (111) and Si (311) reflections. For XRS operations, the 311 reflection is used to obtain photon energy resolving powers of 30000 with a flux of 10^{12}/s [42, 43].

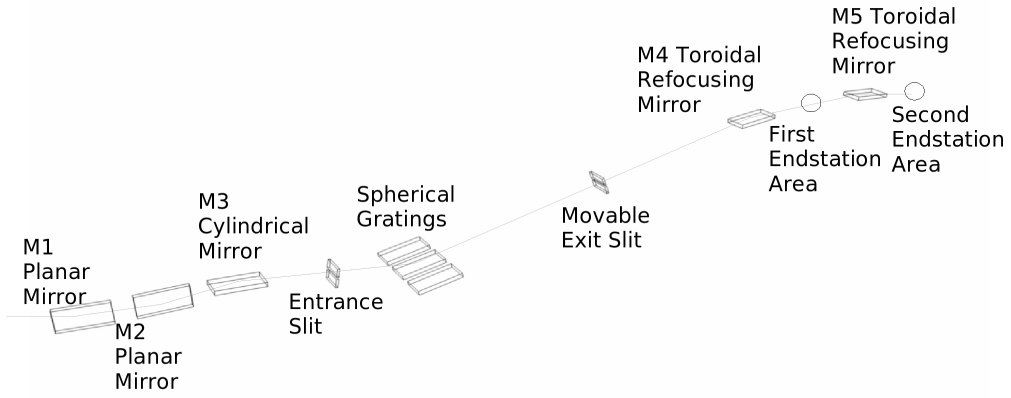

Figure 2.1: The optical layout of the SGM beamline at the CLS. Figure taken from Ref. [41].

2.3 Measurement of the linear attenuation coefficient

2.3.1 Transmission measurements

Transmission measurements are performed by comparing the incident flux to the flux remaining after the beam is passed through a thin sample. This measurement method is very useful because it probes the linear attenuation coefficient directly though Eq. 1.10. If the incident and transmitted flux are measured with calibrated detectors, the absorption cross section can be obtained without complication.

The transmission method relies on the ability to produce samples that are of a uniform thickness over the size of the beam spot used in the measurement. Changes in sample thickness or the presence of pin holes introduce distortions in the measured absorption spectra. The required sample thickness x is on the order of the penetration depth of the photons used for the measurement, which for the soft x-ray wavelengths is on the order of a hundred nanometers. Producing samples that have a uniform thickness of 100 nm and a size of more than a few hundred nanometers in width and height is often not possible, so transmission measurements generally require very small beam spot sizes. Also, it is often desirable to look at samples that are deposited on substrates or have some thickness distribution. In these cases, transmission measurements are also not possible.

Despite the stringent sample thickness requirements, transmission measurements have found a very important application in x-ray microscopy. In a scanning transmission x-ray microscope (STXM), a fresnel zone plate is used to focus the x-ray beam to as small as 30 nm in width and height [44]. Using interferometry, the sample position is controlled on the order of 10's of nanometers and the spatial structure of samples dispersed on thin membrane supports (typically silicon nitride) can be explored. By raster scanning the sample it is possible to find and study portions of the sample where the thickness requirements for transmission measure-

ments are met. Transmission intensity is then measured using highly sensitive photo-multiplier tubes (PMT) coated with a x-ray sensitive phosphor. STXM beamlines have proven themselves invaluable investigating electronic structure at the nanoscale with powerful applications in biology [45] and chemistry [46].

For looking at bulk composition or at samples that cannot be prepared for the STXM (like thin films on substrates), transmission methods are not possible. In these studies a secondary yield method, like electron yield or fluorescence yield, can be employed to indirectly probe the attenuation coefficient. These secondary methods probe the attenuation coefficient by detecting the decay of core excited atoms. While quite valuable, both electron yield and fluorescence yield measurements are only valid when certain sample conditions can be met. Electron yield and fluorescence yield were used to measure the spectra found in Chapter 3 and Chapter 4 and will be discussed in detail in the next sections. Another measurement method, the inverse partial fluorescence yield, is a type of fluorescence yield measurement that was developed on the SGM beamline at the CLS, and regains some of the simplicity seen in transmission measurements. The concepts behind IPFY will also be discussed in the following sections.

2.3.2 Electron yield measurements

Electron yield measurements involve probing the attenuation coefficient by measuring the intensity of the electrons emitted from the sample. The energy distribution of the emitted electrons can be ignored, as in the case of the total electron yield (TEY), or can be examined using an electron energy analyzer, as is done for measurements of the partial electron yield (PEY) or Auger electron yield (AEY). Electron yield measurements, primarily the TEY, are often extremely easy to perform and can be very useful for studying the surface of many conducting samples where bulk sensitivity is not required. The surface sensitivity and the effects of sample charging are the primary drawbacks of electron yield measurement, making the method unsuitable for the study of many systems. Another drawback of TEY and PEY is that there is no adequate theory that can accurately describe the ratio of incident photons to emitted electrons, making the methods unsuitable for some types of quantitative analysis [7].

Electron yield intensities are generally considered to be proportional to the attenuation coefficient at the sample surface because of the extremely short escape depth of the electrons compared to the penetration depth of the photons. Soft x-ray photons have penetration depths on the order of a hundred nanometers, while the photoelectrons and Auger electrons they generate have mean free paths of just a few nanometers [47]. Photoelectrons generated within the bulk of the sample are inelastically scattered and generate electron cascades that typically do not reach the sample surface. At the surface, Auger electrons, directly emitted photoelectrons and inelastically scattered electrons can leave the sample and be detected. Energy dependant changes in the x-ray attenuation coefficient affect the number of electrons liberated in the surface region: as the attenuation coefficient increases at an absorption edge, more photons are absorbed very near the surface, resulting in more electrons being able to leave the sample and increasing the electron yield.

The relationship between the electron yield and the attenuation coefficient can be described by consid-

ering the attenuation of the incident x-ray beam and the inelastic scattering of the electrons resulting from photoemission and Auger emission. This is done, in a fairly rigorous way in the classic book by Stöhr [7]. Following his derivation, the normalized TEY intensity for incident energy E_i as the integral of the intensity coming from some increment dz at a depth z inside the sample can be described as

$$\frac{I(E_i)}{I_o(E_i)} = C \int_0^\infty \frac{\mu_{tot}(E_i)}{\sin\alpha} G_e(E_i) e^{-\left(\frac{\mu_{tot}(E_i)}{\sin\alpha} + 1/L\right)z} dz, \tag{2.1}$$

where $C = \frac{\eta(E_i)}{4\pi}$ is a constant associated with the detector efficiency, $\mu_{tot}(E_i)$ is the attenuation coefficient of the sample, L is the effective electron escape depth and α is the angle of incidence of the radiation. Here, $G_e(E_i)$ is the gain factor for the conversion of photoelectrons and Auger electrons into low energy electrons. Eq. 2.1 can be broken into three main parts based on the following:

- The attenuation of the incident photon beam before it reaches a depth z

$$e^{-\frac{\mu_{tot}(E_i)}{\sin\alpha} z}$$

- The absorption of a photon in dz and the subsequent emission of a photo-electron

$$\frac{\mu_{tot}(E_i)}{\sin\alpha} dz$$

- The formation of an electron cascade or avalanche

$$G_e(E_i)$$

- The re-absorption of the emitted photo-electrons as they move through the sample

$$e^{-\frac{z}{L}}$$

In the total absorption regime, i.e. where the sample is sufficiently thick that all photons are absorbed, Eq. 2.1 becomes

$$\frac{I(E_i)}{I_o(E_i)} = C \frac{\mu_{tot}(E_i)}{\mu_{tot}(E_i) + \frac{\sin\alpha}{L}} G_e(E_i). \tag{2.2}$$

From Eq. 2.2, one can see that the normalized TEY intensity is related to the total attenuation coefficient in the second order. $\mu_{tot}(E_i)$ occurs in both the numerator and denominator which leads to loss of contrast, or signal saturation, if $\frac{1}{L}$ is small compared to $\mu_{tot}(E_i)$. Because the mean free path of electrons is always much smaller than the penetration depth of soft x-ray photons, this will only occur if the sample is a very thin film. In that case, most or all photo-electrons can escape the sample, and the TEY intensity does not reflect the attenuation coefficient. A similar situation is found for fluorescence yield, leading to a saturation effect that is commonly (but incorrectly) referred to as *self absorption*. This will be discussed in the following section. It is also worthwhile to note the inherent inefficiency of the electron yield method: because the signal is coming from a small surface region, only a small fraction of the incident photon beam is involved in

generating the signal. Most photons pass through the surface and generate photo-electrons that are not able to escape the sample.

Even though saturation effects in TEY are not commonly observed, quantitative modelling of TEY is difficult because of a lack of a theoretical model for L and $G_e(E_i)$. These two terms, which together describe the electron scattering process, may be determined empirically for a given material, but because of the inherent difficulty, this is seldom done in practise. These terms are also affected by the electric field across the sample, which is, in turn, related to the electrical properties of the sample. If the sample is not conducting, the transfer of charge through the sample may not occur fast enough to neutralize the charge removed from the sample through photoionization. These factors complicate the theoretical interpretation of the electron yield and will often result in spectral artifacts.

Depth sensitivity in electron yield can be achieved by looking at the energy distribution of the electrons leaving the sample. By monitoring the intensity of a photoelectron peak or an Auger peak using an energy discriminating electron yield detector, surface sensitivity is enhanced. If the intensity of just the low energy electrons is monitored, the measurement becomes slightly more bulk sensitive, down to a few nanometers. Thus, AEY is highly surface sensitive and PEY can be made sensitive to the surface or the bulk depending on the energy window used in the measurement. The TEY signal is dominated by the large number of low energy electrons generated through inelastic scattering so it is more bulk sensitive[1] .

The electron yield measurements shown in this thesis were measured using TEY that was recorded using sample drain current method. A sketch of the SGM sample holder used for the TEY measurements is shown in Fig. 2.2. The sample is affixed to the sample block with a conductive adhesive, typically double sided carbon tape or silver epoxy. The sample block can be inserted into the in-vacuum sample holder through a vacuum load-lock using a transfer arm equipped with a pincer. To ensure good thermal contact, the block is screwed into the holder with an in-vacuum screwdriver. A cold finger is used to bring liquid nitrogen or helium close to the sample holder but it is electrically isolated from the sample holder with a 1 mm thick sapphire plate. Electrical contact is made with the sample holder using a 32 gauge wire that is connected to an electrical feedthrough at the top of the manipulator. The wire is heat sunk on the cold finger at several points to optimize cooling. An optional shroud (not shown) is also used to reduce the effects of infrared heating.

This sample holder system provides a simple, yet effective, method for determining the attenuation coefficient in conductive samples using TEY. As photo-electrons leave the sample, a small positive charge is generated at the sample surface. This charge is neutralized by electrons coming through the sample, the sample holder and the TEY wire, setting up a small current as shown in Fig. 2.3. In order for a drain current to be established, a conductive path between the sample surface and the sample holder must exist. For this reason, electron yield measurements of strong insulators are not possible with out some type of charge

[1] In the context of this discussion, bulk sensitivity refers to approximately the top 5 nanometers of the sample which can still be considered the surface in many applications

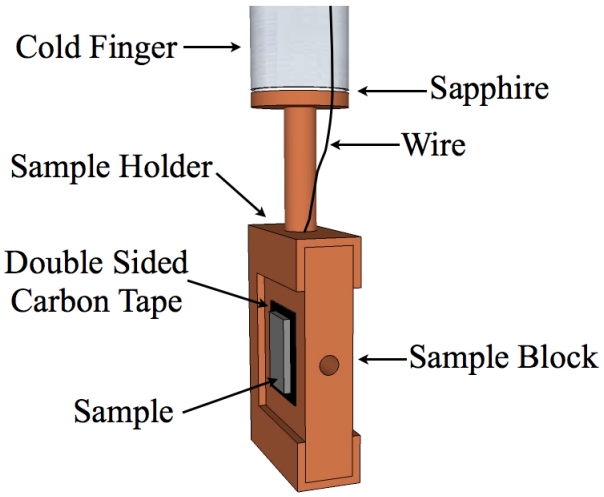

Figure 2.2: In-vacuum sample system for collection of total electron yield at low temperatures. The sapphire provides electrical isolation while still allowing for thermal conduction. The wire connects the sample holder to a vacuum feedthrough.

compensating apparatus. Fortunately, for the samples studied as part of this work, sample charging was not a factor.

2.3.3 Fluorescence yield measurements

Fluorescence yield, like electron yield, allows for the measurement of the total attenuation coefficient in thick samples by monitoring a by-product of photon absorption. Fluorescence yield measurements involve the use of a photon sensitive detector to determine the change in the number of photons emitted by the sample resulting from core hole decay as the incident energy is scanned through an absorption edge. Measurement of the fluorescence yield offers some distinct advantages over the electron yield methods, specifically bulk sensitivity and quantitative yields. The main drawback to fluorescence yield is a strong saturation effect that has prohibited its use in all but the most dilute samples. Another complication related to using fluorescence yields to probe the attenuation coefficient is that the fluorescence efficiency, that is the number of fluorescence photons emitted as a function of the number of core holes created, is not a constant.

In the following subsections, a model of the fluorescence yield intensity will be presented and saturation effects will be discussed. In the third subsection, a recently developed method for directly probing the linear attenuation coefficient using fluorescence yields will be described. The fourth subsection will build on the discussion of the Kramers-Heisenberg equation that was introduced in Sec. 1.3.1 and use a coherent picture of the fluorescence process to discuss fluorescence efficiencies near resonance.

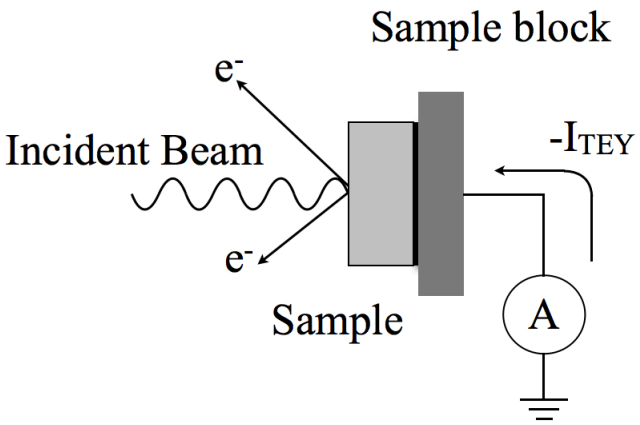

Figure 2.3: A sketch of the electrical circuit that is established in a TEY measurement on a conductive sample. For an insulating sample a charge barrier between the front and the back of the sample will exist.

Fluorescence intensities

Fluorescence photons are produced by the spontaneous decay of core excited atoms. When a core hole is formed by the absorption of an x-ray, the atom is left in a highly unstable state that will decay to the ground state on the femtosecond time scale. An electron from a lower energy orbital moves into the unoccupied core level and the energy difference between the two orbitals is shed as a fluorescence photon. The fluorescence efficiency, $\omega(E_i, E_f)$, is defined as the probability that a core hole created by absorption of a photon with energy E_i will decay by the emission of a photon of energy E_f, where

$$E_f = E_{core} - E_{outer}. \tag{2.3}$$

$\omega(E_i, E_f)$ is typically only a few percent for the light elements with the predominant decay method being the emission of an Auger electron. Although fluorescence is an inefficient decay process at soft x-ray energies, the yields are still quite useful because, unlike the electron yield where a complex scattering process takes place, the fluorescence yield intensities can be modelled.[2]

The fluorescence yield of a sample can be measured by using a suitable detector that is sensitive to x-ray photons. Typically a micro-channel plate (MCP) or photodiode, placed close to the sample is used. To avoid

[2]Fluorescence yield also has an inherent advantage over transmission measurements for dilute samples. Transmission measurements have a contrast that is determined by the optical density of the material being studied. For dilute systems the overall contrast is not affected strongly by the presence of the low concentration atom resulting in a limited sensitivity. Although fluorescence efficiencies are weak for the light elements, each detected fluorescence photon with the appropriate energy E_f corresponds to a core excitation event.

measuring a signal comprising of both the electron and fluorescence yield, a biased mesh or grounded thin filter is placed between the sample and the detector. If the sensitivity is roughly even across all fluorescence energies, the output of the detector as a function of the incident photon energy will be called the total fluorescence yield (TFY). If the detector is able to select out only some bandwidth of the fluorescence yield, using either a grating based spectrometer, a thin film filter or through an energy discriminating detection method, the partial fluorescence yield (PFY) can be measured.

Fluorescence yields are considered bulk sensitive because they probe depths up to the penetration depth of the incident photon beam, which for soft x-rays, is on the order hundreds of nanometers.[3]. This useful characteristic of fluorescences yields arises because the fluorescence process always generates a photon with a similar or lower energy than the incident photon. The absorption cross sections for the fluorescence photons are therefore similar to the incident photons, so they have a reasonable chance of reaching the surface of the sample and making it to the detector.

Under the proper conditions the fluorescence yield can be considered to be proportional to the linear attenuation coefficient of the sample. But this is often not the case. To examine the limitations of the fluorescence yield method, a theoretical model for the normalized fluorescence yield intensity is useful.

The normalized fluorescence intensity can be modelled in a similar way as was done for the TEY in Sec. 2.3.2, but without the need to introduce the poorly defined electron cascade parameters $G(E_i)$ and L. The emission from element X with energy E_f when excited by photons with energy E_i, that comes from a region of the sample with an incremental thickness dz at a depth z is given by

$$\frac{I(E_i, E_f)}{I_0(E_i)} = C \sum_X \int_0^\infty \omega_X(E_i, E_f) \frac{\mu_X(E_i)}{\sin\alpha} e^{-\left(\frac{\mu_{tot}(E_i)}{\sin\alpha} + \frac{\mu_{tot}(E_f)}{\sin\beta}\right) z} dz, \tag{2.4}$$

where we have introduced the angle β to describe the direction of emission. Like the equation for TEY, Eq. 2.4, can be broken down into a series of discreet events:

- The attenuation of the incident photon beam before it reaches a depth z

$$e^{-\frac{\mu_{tot}(E_i)}{\sin\alpha} z}$$

- The absorption of a photon of energy E_i in a thickness dz and the subsequent emission of a fluorescence photon with energy E_f

$$\omega_X(E_i, E_f) \frac{\mu_X(E_i)}{\sin\alpha} dz$$

- The attenuation of the fluorescence photons by the sample on their way to the detector

$$e^{-\frac{\mu_{tot}(E_f)}{\sin\beta} z}$$

These steps are shown graphically in Fig. 2.4.

[3]There are many different definitions of the surface and the bulk of a material. For the purposes of the discussion in this thesis, measurements are considered to be representative of the bulk of the sample when they are not influenced by the first few atomic layers where surface interactions can be significantly modifying electronic structure. As soft x-ray penetration depths are on the order of 100Å, they are generally considered to be reaching the bulk of the sample.

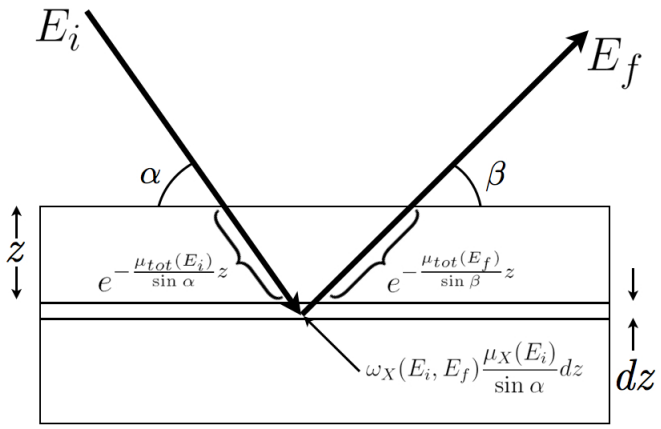

Figure 2.4: The steps involved in the generation and detection of fluorescence. To detect a fluorescence photon from a depth z in the sample, the incident photon has to reach that depth before being absorbed. The excited atom then has to decay through emission of the fluorescence photon, which then has to traverse the sample before it can reach the detector.

Integration of Eq. 2.4 gives

$$\frac{I(E_i,E_f)}{I_0(E_i)} = \mathrm{PFY}_X = C\frac{\omega_X(E_i,E_f)\mu_X(E_i)}{\mu_{tot}(E_i)+\mu_{tot}(E_f)\frac{\sin\alpha}{\sin\beta}}, \tag{2.5}$$

which can be interpreted as the partial fluorescence yield (PFY) at E_f that results from the excitation of element X in the sample. The total fluorescence yield is then the sum of the partial yields

$$\mathrm{TFY} = \mathrm{PFY}_X + \mathrm{PFY}_Y + \mathrm{PFY}_Z \tag{2.6}$$

where emission from each element in the sample is assumed to only occur at one energy, E_f. Note that the total attenuation coefficient $\mu_{tot}(E_i)$ is the sum of the mass attenuation coefficients of each component in the system:

$$\mu_{tot}(E_i) = \mu_X(E_i) + \mu_Y(E_i) + \mu_Z(E_i). \tag{2.7}$$

Saturation in fluorescence yields

Saturation in the context of a fluorescence yield measurement is the loss of contrast in the absorption spectrum that is observed in concentrated samples. An example of saturation effects are shown for Cu metal in Fig. 2.5. It is often incorrectly labelled 'self absorption', which is a misleading term that has caused a great deal of confusion in the field. Saturation effects severely limit the use of fluorescence yield as a useful detection method and has been a major obstacle to the wide spread applicability of XAS.

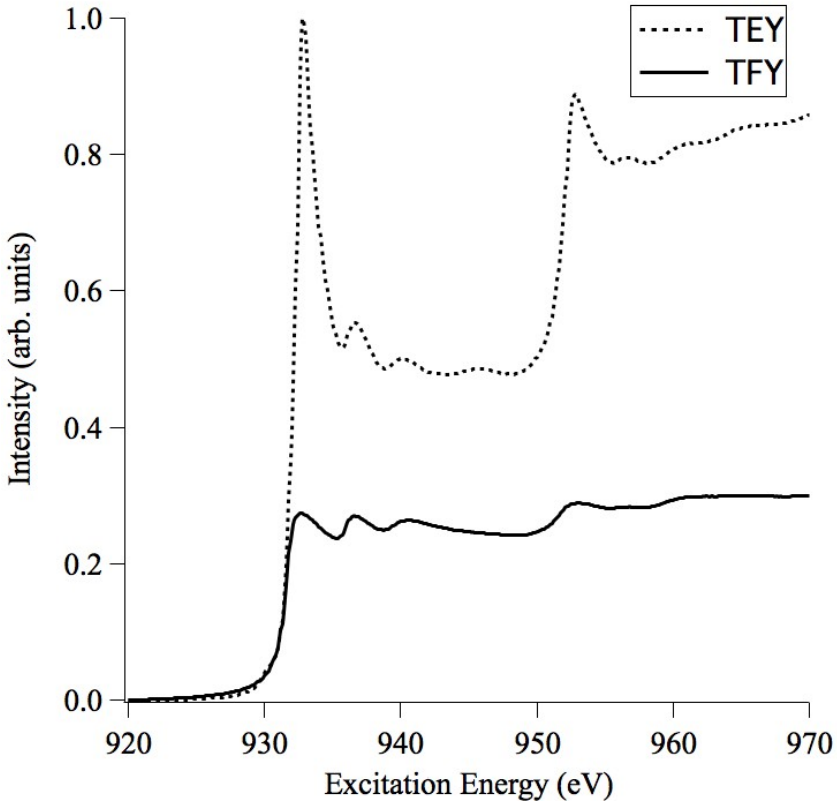

Figure 2.5: The x-ray absorption of Cu metal measured with total electron and total fluorescence yields. The intensities have been normalized to the incident flux and scaled for comparison. Saturation is clearly observed in the TFY spectrum as the attenuation of the height of the main $L_{3/2}$ and $L_{1/2}$ peaks.

Saturation occurs in concentrated samples because the attenuation lengths of the incident x-rays and the fluorescence x-rays are comparable. A qualitative description of the saturation effect in fluorescence yield follows: As the incident x-ray energy reaches the absorption resonance in an absorption measurement, the attenuation coefficient is maximized and all of the incident x-rays are absorbed close to the surface. Because the attenuation length of the fluorescence is less than that of the incident photons, every fluorescence photon emitted towards the surface is able to escape the sample[4]. At that point the electronic properties of the sample are no longer influencing the intensity of the detected signal and contrast is lost. Although it seems contradictory, it is the re-absorption, or *self* absorption of the fluorescence by the sample that makes fluorescence yield work as a probe of the attenuation coefficient! This concept is explained in detail by Eisebitt and his collaborators in their 1993 work, where they also explain that the optimum geometry for minimizing self absorption is normal incidence and grazing pick-off [48].

The origin of saturation in fluorescence yields is further examined using Eq. 2.5, which can be rewritten

[4]The attenuation coefficient of the fluorescence photons is necessarily less than the attenuation length of the incident photons because the incident photons are at the resonance, where absorption is maximized.

with Eq. 2.7 substituted into the denominator, to give

$$\frac{I(E_i, E_f)}{I_0(E_i)} = \text{PFY}_X = C\frac{\omega_X(E_i, E_f)\mu_X(E_i)}{\mu_X(E_i) + \mu_Y(E_i) + \mu_Z(E_i) + \mu_{tot}(E_f)\frac{\sin\alpha}{\sin\beta}}. \tag{2.8}$$

The presence of $\mu_X(E_i)$ in both the numerator and denominator is responsible for the saturation effect. As $\mu_X(E_i)$ increases at an absorption threshold, the partial fluorescence yield, which would ideally increase proportionally to the attenuation coefficient, is damped by the energy dependence of the terms in the denominator. Only when $\mu_X(E_i)$ is small compared to $\mu_Y(E_i) + \mu_Z(E_i) + \mu_{tot}(E_f)$ (the sample is dilute), does PFY_X resemble the attenuation coefficient.

Nonlinear backgrounds in fluorescence yields

Another important, but often overlooked, problem with total fluorescence yield measurements is the potential for a strong energy dependence in the fluorescence background arising from other elements in the sample. This effect can lead to considerable distortions in the total fluorescence yield that further restrict the use of this detection method. While total fluorescence yields may still be useful in some cases, the background emission issues highlight the value of energy resolved fluorescence yield detectors that facilitate the measurement of partial yields.

The effects of the non-resonant background can be illustrated by considering the non-resonant emission from element Y in a sample that is being excited across the absorption edge of element X. The partial yield of element Y is given by

$$\frac{I(E_i, E_f)}{I_0(E_i)} = \text{PFY}_Y = C\frac{\omega_Y(E_i, E_f)\mu_Y(E_i)}{\mu_X(E_i) + \mu_Y(E_i) + \mu_Z(E_i) + \mu_{tot}(E_f)\frac{\sin\alpha}{\sin\beta}}. \tag{2.9}$$

This expression contains $\mu_X(E_i)$, which is the strongly varying term, in *only the denominator*. The other energy dependent terms will typically only exhibit a weak energy dependence for incident photon energies around the resonance excitation energy of element X. This implies that PFY_Y will be inversely proportional to the absorption spectrum of element X. As the TFY is the sum of all the partial yields, it will also contain an additional energy dependent term from coming from the fluorescence of each element in the sample. The strength of this background effect is dependent on the relative intensity of the mass attenuation coefficients and fluorescence efficiencies of the elements involved and can be shown to actually generate sub-background effects in the TFY under certain conditions [49].

The effect of the nonlinear background can be clearly observed when using an energy resolving fluorescence yield detector to measure partial fluorescence yields. This issue will be explored fully in Chapter 4 where the XAS of the iron oxides will be analyzed in detail. For the iron oxides, the strong fluorescence background from the O K_α emission strongly distorts the TFY, making the use of partial yields mandatory for measurement of these samples.

The inverse partial fluorescence yield

The energy dependence in the background fluorescence is major limitation in XAS measured using TFY. But this background effect can also be exploited to measure saturation (self absorption) free XAS using a recently developed method called inverse partial fluorescence yield (IPFY) spectroscopy. This method, developed on the SGM beamline at the Canadian Light Source, requires a detector capable of measuring partial fluorescence yields so that only the background fluorescence is detected. The inverse of this background signal can then be used as a bulk sensitive measurement of the linear attenuation coefficient, without the saturation effects commonly observed in concentrated samples.

The IPFY method is based on the idea that the background fluorescence in the sample is inversely related to the linear attenuation coefficient. Conceptually, IPFY is simple to understand: the non-resonantly excited atoms in the sample can act as 'by-standers' and detect how deep the incident photon beam penetrates into the sample. In the pre-edge region, the incident x-rays do not have sufficient energy to excite the atom of interest, so the photons will penetrate more deeply into the sample and an intense background fluorescence can be measured from the by-stander atoms. At the absorption resonance, the penetration depth is minimized and the much of the photon flux that had been used to excite by-stander atoms is now being used to resonantly excite the target atoms. Therefore, the background fluorescence is reduced proportionally to the reduction in penetration depth.

The theoretical justification for IPFY arises by an examination of the expected partial fluorescence yield from a by-stander atom in the sample. Taking the inverse of Eq. 2.9 one obtains

$$\frac{I_0(E_i)}{I(E_i,E_f)} = \frac{1}{\mathrm{PFY}_Y} = \frac{1}{C}\frac{\mu_X(E_i)+\mu_Y(E_i)+\mu_Z(E_i)+\mu_{tot}(E_f)\frac{\sin\alpha}{\sin\beta}}{\omega_Y(E_i,E_f)\mu_Y(E_i)}. \tag{2.10}$$

Here, the attenuation coefficients of non-resonantly excited elements Y and Z will typically have only a weak dependence on E_i that can be easily accounted for using tabulated values. $\mu_{tot}(E_f)$ and $\omega_Y(E_i,E_f)$ will both be constants, as will the geometry terms, leaving $\mu_X(E_i)$ as the only term that has a strong energy dependence. The IPFY for element X is then defined as

$$IPFY = \frac{1}{\mathrm{PFY}_Y} \tag{2.11}$$

which is expected to be proportional to $\mu_X(E_i)$.

IPFY was first demonstrated for the Cu L-edge and Nd M-edge of $La_{1.475}Nd_{0.4}Sr_{0.125}CuO_4$ (LNSCO) in the 2010 work by Achkar et al. [50]. In Fig. 2.6, the TEY, IPFY and TFY are shown. In this study, the samples were in-situ cleaved surfaces, so the TEY is representative of the bulk. The agreement between the TEY and the IPFY suggests that the saturation effects, visible in the TFY, have been overcome in the IPFY. The distinction between the TEY and the IPFY is that the IPFY signal is generated in the bulk of the sample while the TEY signal is only sensitive to the surface.

Another feature of the IPFY is that there is an offset to the intensity that is completely determined by the geometry of the experiment. This effect is useful because it allows for angle dependent IPFY measurements

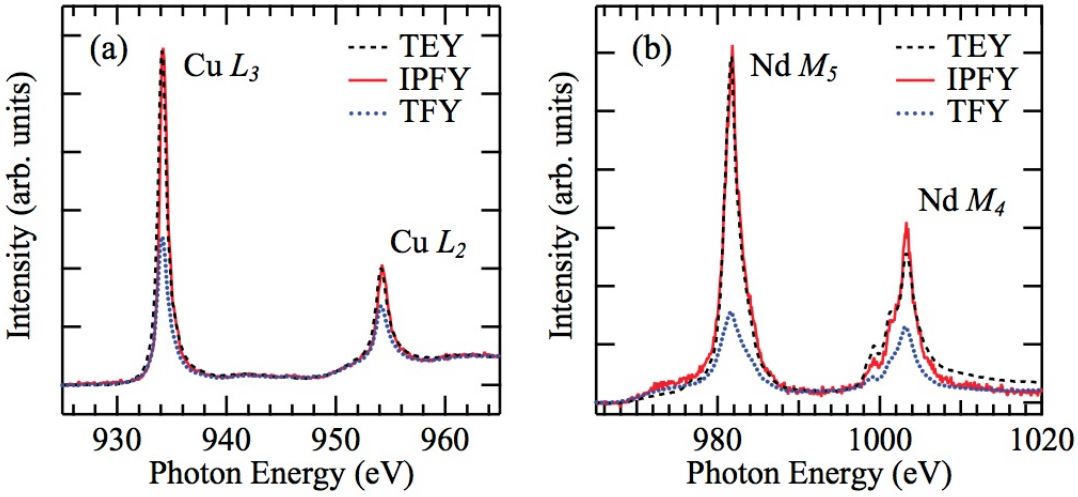

Figure 2.6: The first demonstration of the IPFY method showing the Cu L-edge and the Nd M-edge of LNSCO. Reproduced with permission from [50].

to be used for determination of x-ray absorption cross sections. Eq. 2.10 can be rearranged to give

$$\frac{I_0(E_i)}{I(E_i,E_f)} = \frac{1}{C}\frac{\mu_X(E_i)+\mu_Y(E_i)+\mu_Z(E_i)}{\omega_Y(E_i,E_f)\mu_Y(E_i)} + \frac{\mu_{tot}(E_f)\frac{\sin\alpha}{\sin\beta}}{\omega_Y(E_i,E_f)\mu_Y(E_i)}. \tag{2.12}$$

In this form, the variables describing the geometry, α and β, are both contained in the right hand term. The other members of this term, $\mu_{tot}(E_f)$, $\omega_Y(E_i,E_f)$, and $\mu_Y(E_i)$ are all roughly constant with respect to E_i. This implies that by varying the geometry of the experiment one will expect to see only a change in the baseline of the IPFY and no modification of the intensity of the absorption features.

The geometry dependence of the IPFY was explored by Achkar et al. in an XAS study of NiO and $NdGdO_3$ [51]. Fig. 2.7 shows that changing $\frac{\alpha}{\beta}$ resulted in the expected variation in the offset of the IPFY. This behaviour was then exploited to normalize the intensity of the absorption resonance and determine the absolute intensity of the attenuation coefficient.

The development of the IPFY method has broad implications for the field of x-ray absorption spectroscopy. The primary advantage of IPFY over TFY or PFY is that bulk sensitive XAS of concentrated samples is possible. IPFY is also valuable because it provides a way of directly probing the linear attenuation coefficient with out arbitrary offsets. This last point is important for studies where the absolute magnitude of the absorption resonance is required such as resonant scattering experiments [52, 53].

IPFY has also shown potential for studies where TEY is not possible as in the study of concentrated liquid samples where the sample is separated from the vacuum chamber by a thin membrane and a photon in-photon out detection method is required. It is also important because it is a true measure of the linear attenuation coefficient and does not depend on the fluorescence efficiency of the resonantly excited atom. This point is important because, as will be discussed in the following section, fluorescence efficiencies at resonance are not constant and introduce errors in the PFY and TFY [54].

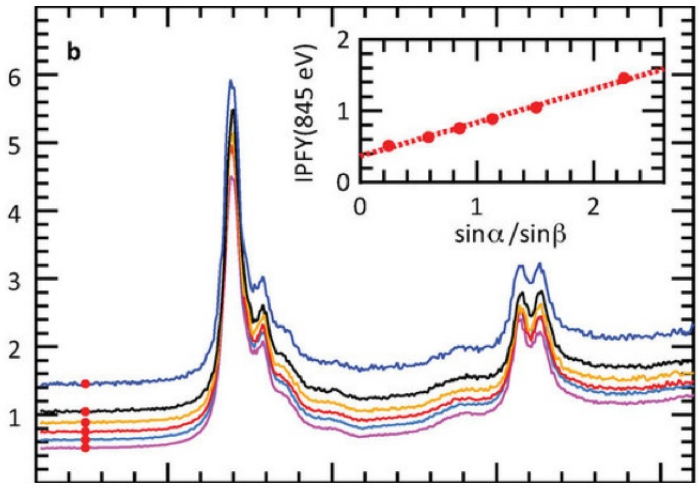

Figure 2.7: The IPFY of NiO as a function of the angle of incidence of the x-ray beam. The detector is in a fixed position. Reprinted with permission from [51].

While IPFY has great potential, there are several limitations to the method that restrict its application. A prerequisite for the use of IPFY is the presence of a suitable by-stander atom in the sample. This by-stander has to have a reasonable absorption cross section at the excitation energies used for the resonant excitation of the target atom. It has been determined that O works well as a by-stander for studies of the transition metals and rare earths [50, 55–57]. Another prerequisite is that the sample be sufficiently thick to satisfy the total absorption requirement. Without total absorption, the integration in Eq. 2.5 is not valid and the IPFY relationship breaks down. Finally, for the angle dependent IPFY, the sample surface must be sufficiently flat (on the order of the attenuation length) or the relationship between the geometry and the IPFY intensity is not valid.

More discussion on the IPFY and other effects of non-resonant emission will be provided in Chapter 4 with specific application to iron oxide minerals and aqueous Fe complexes. In addition, more details on the detection systems needed for IPFY will be introduced in Sec. 2.5.1 along with information on the data processing procedures used to extract IPFY.

Fluorescence efficiencies

Up to this point, the discussion of x-ray fluorescence as a two step process, where the core excitation and core hole decay are considered two incoherent processes, has been sufficient. Indeed, the two step picture is generally suitable for describing the emission of non-resonant photons from the sample, where the fluorescence is not originating from a resonantly excited atom. In this picture, the fluorescence efficiency, $\omega(E_i, E_f)$, is a property of the core excited atom and it is constant across all of the excitation energies used in an absorption spectrum. This implies that the amount of fluorescence yield from a sample is linearly related to the number

of core holes created in the sample, allowing for a direct measurement of the linear attenuation coefficient (in dilute samples) by measurement the intensity of the fluorescence from the sample. But, as was discussed in Sec. 1.3.1, fluorescence is accurately modelled as a coherent second order optical process. It then follows that the intensity of the fluorescence is not constant across an absorption edge, but has some dependence on the intermediate states involved in the absorption process [54].

The relationship between the intermediate states and the fluorescence intensity stipulates that the linear attenuation coefficient is not directly probed by the fluorescence yield measurements. Instead, we must expect some deviation between the measured fluorescence intensity and the x-ray absorption cross section. While these deviations are generally small and may not change affect the overall interpretation of the x-ray absorption data, they do pose a problem for the development of quantitative applications of x-ray absorption spectroscopy. The application of XMCD, for example, requires very accurate polarization dependent measurements of the linear attenuation coefficient. Small changes in the fluorescence efficiencies due to changes in the coherent scattering cross sections could introduce error into the analysis [54].

While the measurement of the true x-ray absorption cross section using fluorescence yields may be impeded due to the coherent nature of the x-ray absorption and emission process, IPFY measurements do not experience these deviations. Since IPFY utilizes the *non-resonant* emission (NXES) from the sample, the intermediate state effects are not a factor in producing the observed spectrum. Although NXES is still a coherent second order optical process, the coherence is found to play no significant role in the emission spectrum [6]. The IPFY, therefore, does not suffer from the distortions experienced by the traditional fluorescence yield measurements. This feature of IPFY will be discussed in more detail in Chapter 4 where a direct comparison between the IPFY and PFY for a dilute aqueous Fe solution will be made.

2.3.4 Measurement of the incident flux

In a typical XAS experiment, the incident flux is monitored by using the electron yield from a fine gold mesh that is placed between the last beamline component and the sample. The mesh will absorb some fraction of the incident beam and eject a number of electrons that is proportional to the flux of the incident beam and the incident photon energy. The electron yield from the mesh can be monitored by measuring the drain current coming into the mesh in order to neutralize the positive charge left behind by the emitted electrons. Typical drain currents are on the order of nano-amps and can be measured with a suitable ammeter. This mesh current, or I_{mesh}, can be measured simultaneously with the signals coming from the sample and can be used to normalize out time or energy dependent fluctuations in the incident beam flux.

The constant of proportionality that relates I_{mesh} to the incident photon flux, Γ_o, can be determined experimentally using a calibrated photo-diode. These devices output a current, I_{PD}, that is related to the incident photon flux according to

$$I_{PD} = \Gamma_o \times \frac{\hbar\omega \times S_{e^-}}{e}, \tag{2.13}$$

where S_{e^-} is the number of electron-hole pairs produced per eV of energy deposited in the diode [58]. The

simultaneous measurement of I_{mesh} and I_{PD} can be made with the photo-diode in place of the sample, allowing one to write

$$I_{mesh} = L\Gamma_o \times \frac{\hbar\omega \times S_{e^-}}{e} \tag{2.14}$$

where L is a constant relating I_{mesh} to I_{PD}. While L and S_{e^-} will have some energy dependence, it does not change significantly over a typical XAS scan range.

One problem associated with using a mesh for determining incident flux is the tendency for the mesh to become contaminated over time. Although the mesh is typically made from Au and is maintained under high vacuum, it is possible for small organic molecules to be physically and chemically absorbed [59, 60]. Measurements of the electron yield of the mesh at the C K edge show that, at pressures of 10^{-8} Torr and with an incident photon flux of 10^{12} photons per second, C contamination will occur within minutes. Moving the mesh so the beam is incident on a different part of the mesh shows less contamination, suggesting that the interaction of the beam with the Au is prompting the condensation of C containing molecules from the vacuum onto the mesh. This is consistent with interfacial electrochemistry studies that show CO adsorption rates could be affected by the surface charging in the mesh resulting from electron ejection [61].

Mesh contamination has a dramatic effect on the incident flux measurement, particularly when measuring the C K edge where C adsorption on the beamline optics has strong effects on the beamline transmission. Electron yield of the mesh is severely affected by the presence of even a very thin layer of contamination, resulting in a incident flux measurement that reflects the C K edge of the adsorbed C species [62]. To remedy this problem, *in-situ* Au evaporators are used to periodically refresh the Au surface. This method is only moderately successful as the clean Au surfaces of the mesh will quickly be recontaminated. Better normalization results from using a silicon photodiode to measure the incident flux in a second scan. While this prohibits simultaneous measurement of the incident flux and the sample absorption, it can be used to improve the normalization, particularly for low concentration samples. Because the photodiode is measuring the energy deposited in a carbon free region of depleted Si [58] it is immune to small amounts of C contamination at its surface.

Calibrated photodiode measurements were performed over the entire photon energy range of the SGM beamline at the CLS and are shown in Fig. 2.8. The overall shape of the flux profile reflects the efficiency of the optics in the beamline and the power output of the insertion device. Flux is maximized around 500 eV, where the output of the SGM undulator peaks and the optical efficiency is highest. At higher energies, the flux decreases due to a reduction in the reflectivity of the optics for a given angle of incidence. Several sharp absorption lines can be observed in the flux profile at the C K, O K, Cr L and Ni L edge energies. The C and O features are due to contamination of the beamline optics from general use. The Cr absorption lines arise due to absorption by the Cr binding layer used in the mirror coating process. Ni absorption is suspected to be present due to migration of the Ni (used to coat the low energy grating) from the low energy grating to the medium and high energy gratings.

Measurement of the incident flux for XRS measurements is simplified substantially by the use of ioniza-

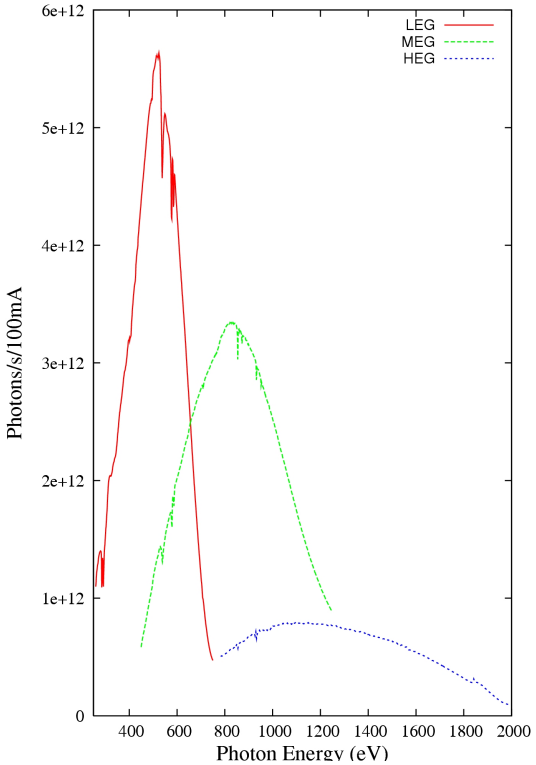

Figure 2.8: The calibrated photon flux of the SGM beamline at the CLS.

tion chambers. Because the attenuation length of hard x-ray photons is much larger than for soft x-rays, the attenuation of the beam by a atmospheric pressure gas and thin kapton windows is negligible. The photoionization of the gas produces a small current in a slightly biased anode which can be considered to be proportional to the photon flux [63]. Tabulated atomic cross section data can be used along with the gas pressure and chamber length to calculate absolute values for the flux.

2.4 Measurement of the dynamic structure factor

2.4.1 The double differential cross section

XRS experiments involve the measurement of the double differential scattering cross section (DDSCS) in order to determine the dynamic structure factor. This implies three separate experimental requirements: First, the sample must be excited by a well collimated monochromatic, hard x-ray photon beam with a known photon flux. Second, the detector must have a well defined solid angle, $d\Omega$, so that the momentum transfer $\mathbf{q}$ can be determined. For $\mathbf{q}$ dependent XRS measurements, this solid angle has to be selectable over a wide range. Third, the energy of the scattered radiation entering $d\Omega$ has to be analyzed with the appropriate resolution $d\omega$. The following subsections will discuss the instrumentation and methods used in

the measurement of the DDSCS.

Excitation source

The excitation source for XRS experiments consists of a suitable hard x-ray beamline equipped with a high resolution monochromator. The energy of the incident beam E is typically chosen in the 5 keV to 10 keV energy range to achieve the desired $\mathbf{q}$ value and penetration capabilities. The excitation energy is also chosen to maximize the incoherent scattering cross section. At lower energies the coherent scattering and absorption cross sections dominate, while at higher energies the incoherent cross section decreases [64]. The ideal excitation energy is a function of the atomic number of the target atom and the DDSCS drops off at high Z [65].

The energy resolution, $\Delta E/E$, of the beamline monochromator is very important because, as is the case for XAS, it determines the level of detail that will be observed in the measured spectra. Double crystal monochromators (DCM) use Bragg scattering from a pair of identical silicon crystals to achieve resolving powers better than 10^{-4}. For more demanding experiments, the output of a DCM can be passed through another set of crystals or set to use diffraction from higher orders. This type of arrangement has been used to achieve resolutions on the order of 10^{-7} [66]. The drawback to using higher diffraction orders and multiple monochromators is that the flux on the sample is reduced.

Scattered photon energy analysis

A spectrograph with energy resolution capabilities similar to the incident beam monochromator is required to analyze the scattered photon energy. Analyzer spectrometers are constructed around the Rowland circle geometry (see Sec. 2.2.2) and can be used with a real or virtual entrance slit[5]. As shown in Fig. 2.9, x-rays can be scattered from a sample and diffracted from a focusing crystal. The diffracted photons pass through an exit aperture before being counted by a suitable detector.

For optimal efficiency and resolution, the Rowland geometry must be maintained as the incident photon energy, scattered photon energy or scattering angle are varied. This requires the co-ordinated rotation of the detector and the analyzer crystal around the Rowland circle and rotation of the entire analyzer around the sample position.

The XRS measurements contained in Chapter 4 of this thesis were made on the lower energy resolution inelastic scattering (LERIX) spectrometer on the 20ID beamline at the Pacific Northwest Consortium (PNC) sector of the (APS) [67]. The layout of this instrument is shown in Fig. 2.10. In order to avoid complicated motion of the analyzer components, 19 separate analyzer units, each consisting of a spherically bent Si analyzer and a NaI scintillation detector, are mounted in a semicircular frame around the sample. Using

[5] A virtual entrance slit corresponds to using the size of the beam as the entrance aperture with the position of the analyzer crystal determining the scattering angle

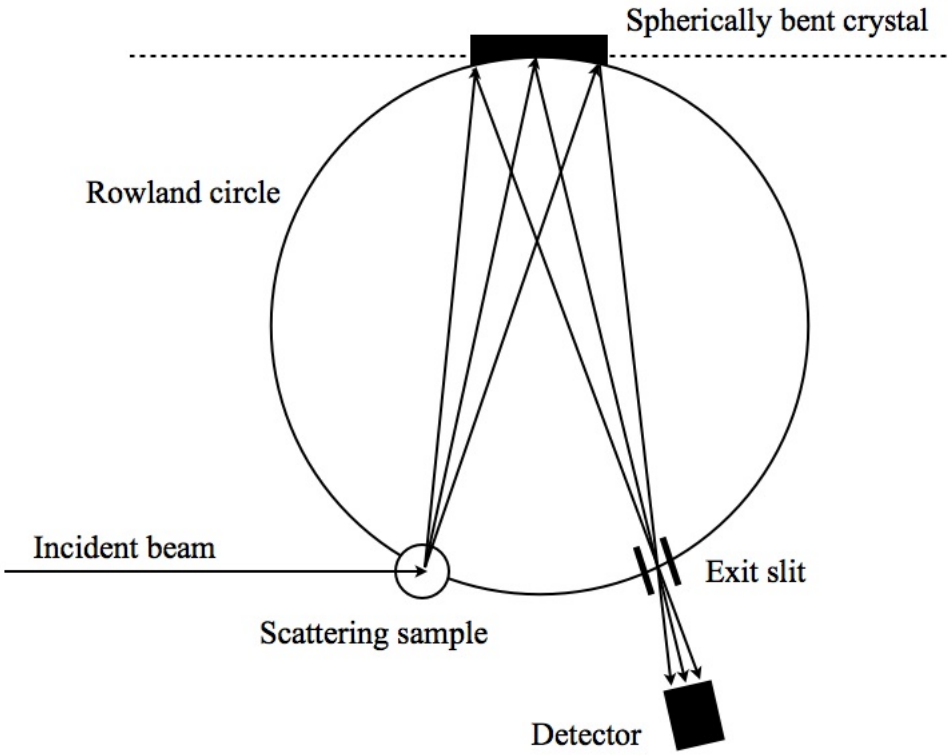

Figure 2.9: Layout of a spherically bent crystal analyzer for measurement of XRS.

LERIX, simultaneous measurement of XRS at 19 different **q** values are possible. If the particular transition is independent of **q**, all of the detectors signals can be summed to improve signal levels.

2.5 Soft x-ray absorption instrumentation and methods development

2.5.1 Silicon drift detectors

A silicon drift detector was added to the x-ray absorption endstation of the SGM beamline to facilitate the acquisition of partial fluorescence yields. As discussed in Sec. 2.3.3, there are great advantages to measuring the partial fluorescence over the total fluorescence yields. The key benefits have been the ability to eliminate energy dependent background effects and enable the acquisition of inverse partial fluorescence yield measurements. The following sections discuss the operation and performance of SDD detectors for soft x-ray absorption spectroscopy applications.

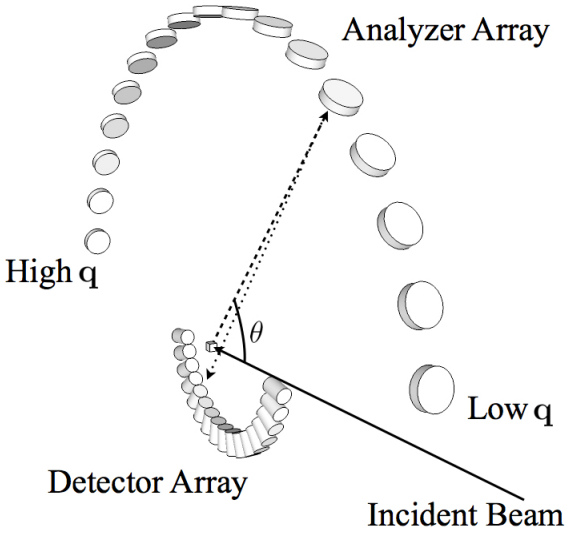

Figure 2.10: A schematic diagram of the LERIX spectrometer at the APS demonstrating the spectrometers ability to measure low and high **q** data at the same time. For scale, the distance between the sample and analyzers is approximately 1m.

Operation

SDDs are a class of solid state detector that measures the energy of photons by determining the amount of ionization they produced when they are absorbed within a detection medium. Detectors of this type consist of a highly resistive, n-type diode that is operated under a large bias, as shown in Fig. 2.11. When charge is liberated in the semiconductor, it is pulled toward the anode of the detector and collected for pulse processing. The pulse is amplified and shaped to determine the energy of the incident photon.

The performance of energy discriminating solid state detectors is determined by the amount of electrical noise in the system. The noise is characterized by the equivalent noise charge (ENC) which is a derived term that incorporates the noise in the signal, the capacitance at the input and the effects of the pulse processor. The overall effect of the noise is to broaden the distribution of measured photon energies, reducing the energy resolution of the detector. Standard solid state detectors (SiLi, Ge) are not suitable for soft x-ray fluorescence spectroscopy because their energy resolution is on the order of 100's of eV, which is not sufficient for resolving soft x-ray emission lines. Cooling the detector is used to reduce the number of thermally generated carriers in the semiconductor, improving the resolution, but the limiting factor was the output capacitance of the diode.

SDDs overcome the noise problems associated with other solid state detectors by reducing the size of the anode, thus minimizing the output capacitance of the diode [68]. As shown in Fig. 2.11, an array of negatively biased ring electrodes are used to generate a radial electric field inside the diode. Charge generated inside

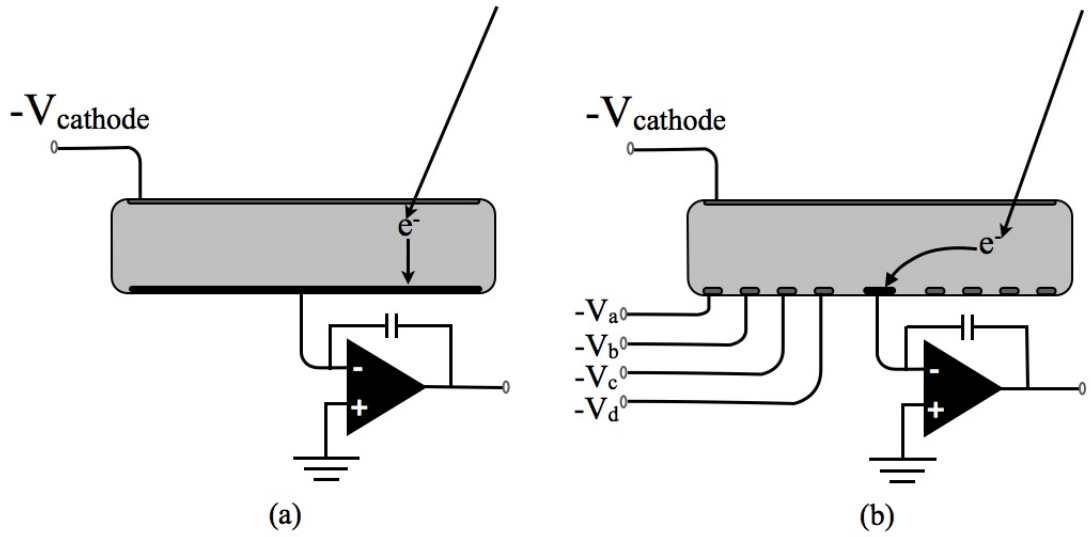

Figure 2.11: The distinction between silicon drift detectors (b) and standard diode based energy discriminating detectors (a). In SDDs, the large anode has been replaced by a small central anode surrounded by negatively biased ring electrodes. The ring electrode channel any ionized electrons toward the anode. Because the anode can be made small, the input capacitance of the amplifier is reduced, improving detector resolution.

the active region of the diode is guided by this field toward the small anode, typically placed at the center of the diode. Using this design, detectors capable of resolutions (FWHM) of 70 eV have been constructed [69].

Window material

One of the limiting factors in the application of SDDs for use in the soft x-ray region has been, until recently, the lack of an appropriate entrance window material. The entrance window is required to seal the detector under vacuum and still allow x-rays to reach the diode. Because the penetration depth of soft x-rays is so short, the development of an appropriate window material was not trivial. In the last decade, thin polymers or silicon nitride windows have become the standard for soft x-ray applications.

SDD detectors need to be operated under vacuum to avoid the accumulation of water and other contaminants on the diode surface. During operation, the diode is cooled to -35^{o}C in order to reduce the drain current of the diode. If exposed to air under these conditions, condensation would form on the detector, affecting its efficiency and eventually damaging the diode. Therefore, the detectors are hermetically sealed in TO8 transistor packages while under vacuum.

It would be possible to operate the SDDs in a windowless fashion inside an x-ray absorption chamber but it is desirable to protect the detector from potential damage by using a suitable window. If the vacuum chamber were to be inadvertently vented during windowless operation of the detector, condensation could form on the detector surface very rapidly, potentially causing irreversible damage to the diode. It is also

possible that the outgassing from samples could deposit onto the diode surface, affecting transmission into the detector and possibly causing damage to the detector, so windowed operation is preferred.

Polymer and silicon nitride are the two window materials commonly used for low energy operation of SDDs. Polymer based windows are produced by depositing layers alternating layers of polymer and aluminum. Silicon nitride windows are fabricated by depositing a thin film of the silicon nitride on a silicon frame and then etching away a portion of the frame, leaving a free standing film. Both windows are able to withstand repeated cycling between vacuum and atmospheric pressure but both are extremely fragile to contact and must be handled carefully. Silicon nitride has slightly better transmission properties than the polymer, allowing for approximately 40% transmission for C K_α emission (277 eV) and 80% for Na K_α emission (1040 eV). Polymer windows have comparable transmission for C K_α emission but they only transmit 60% for Na K_α emission. The polymer also has much lower transmission at energies just above the C K_α emission energy because of their large C content. This makes the polymer less transparent for N and O K_α and Ti, Vi, Cr and Mn L $_\alpha$ emission lines. A plot of the transmission of AP3.3 polymer from Moxtek, Inc. and the C2 silicon nitride window from Amptek, Inc. are shown in Fig. 2.12.

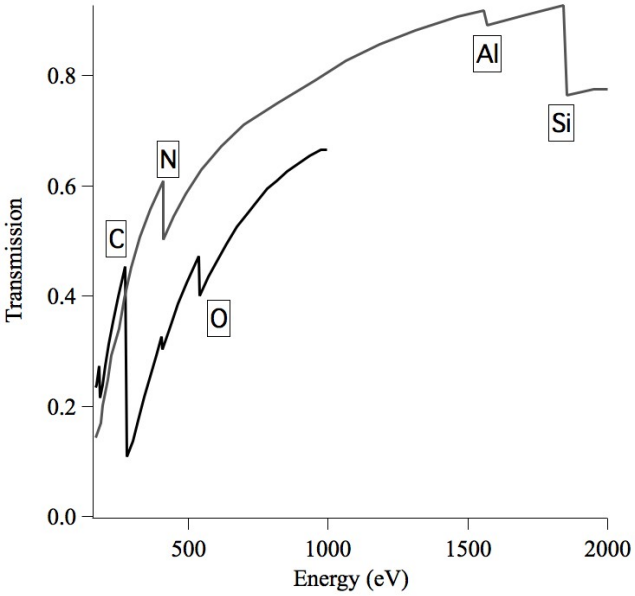

Figure 2.12: The transmission of AP3.3 polymer (black) and silicon nitride (grey) based windows used in SDDs. The absorption features arising from the different elements in the windows are highlighted.

Implementation

For use on the SGM beamline, a commercial SDD with a polymer window and a 25 mm^2 active area was purchased from Princeton Gamma Tech (PGT). The installation of the PGT unit on the SGM beamline was one of the first, if not the first, examples of the application of SDDs to soft x-ray absorption spectroscopy.

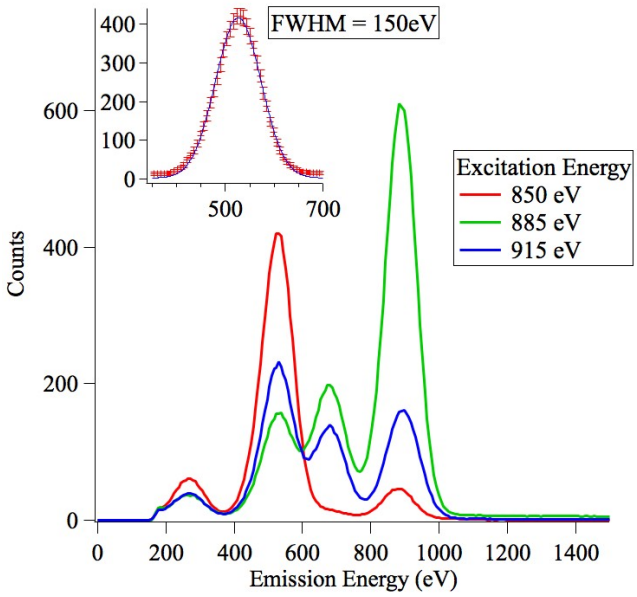

Figure 2.13: The XRF spectrum of CeO_2 measured at excitation energies in the pre-edge, at the $M_{4,5}$ absorption resonance and in the post edge. The inset shows a fit of the O K_α emission line for excitation in the pre-edge.

Configuration, triggering and readout capability for the SDD unit was integrated into the beamline control system using custom software based on the API provided by the vendor. A complete x-ray fluorescence spectra is recorded for each excitation energy in an x-ray absorption scan. The fluorecence data is then normalized to the incident photon flux and presented as an excitation-emission matrix. This is very similar to a RIXS map except that the energy resolution (FWHM) of the fluorescence photons is much worse - on the order of 100 eV. Because of the decreased resolution in the fluorescence yield RIXS analysis is not possible. But partial yields can be extracted by performing horizontal cuts through the matrix.

The excitation-emission matrix

To demonstrate the capabilities of the SDD detector at soft x-ray wavelengths, the XRF spectrum of CeO_2, measured using the PGT detector on the SGM with excitation energies below, at and above the M_5 absorption resonance is shown in Fig. 2.13. The O K_α emission in the spectrum taken with pre-edge excitation was fit with a Gaussian distribution, shown in the inset of Fig. 2.13, using a sigma of 66.1 or a FWHM of 155 eV. The total counts recorded were 64101, 124477 and 68981 for the spectra measured at 850 eV, 885 eV and 915 eV, respectively.

Each of the XRF spectra show emission at energies consistent with the presence of C K_α (277 eV), O K_α (525 eV) and Ce $M_{\alpha,\beta}$ (902 and 883 eV) and Ce M_ζ (679 eV). The C emission is attributed to the carbon tape used to hold the powder sample in place. The pre-edge emission spectrum shows the strongest O and C emission intensity but also shows some intensity at the Ce emission energies due to Ce excitation by second order light. Some portion of the intensity at the Ce $M_{\alpha,\beta}$ emission energies is also expected to arise from

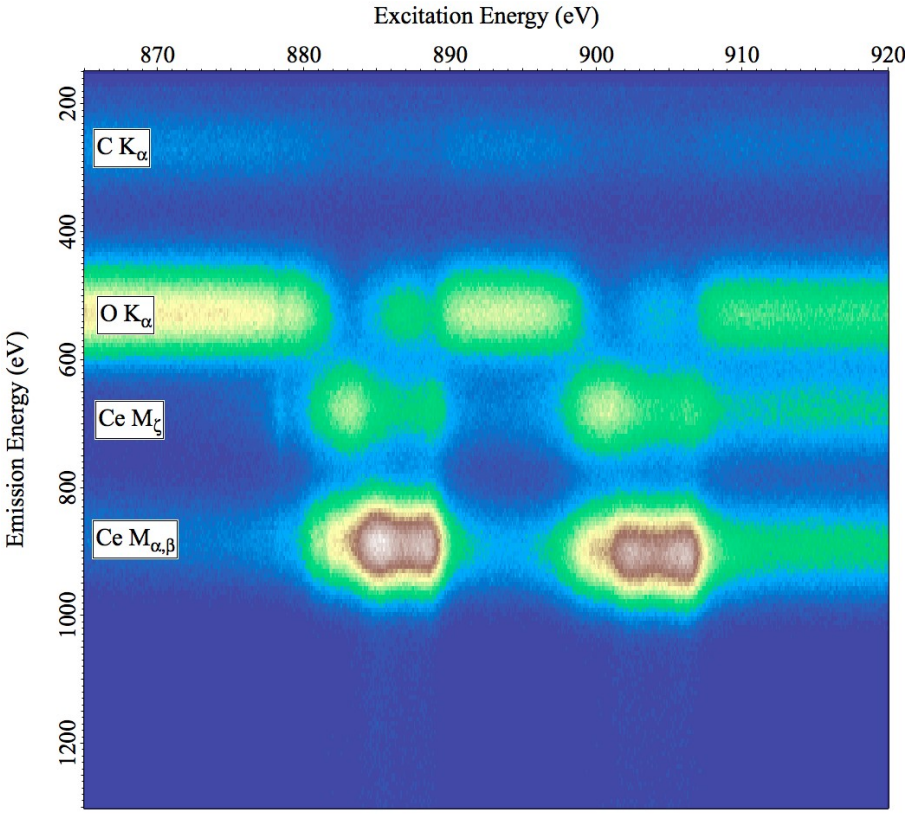

Figure 2.14: The excitation-emission matrix for CeO_2 at the Ce M-edge measured with a silicon drift detector.

elastic scattering of the incident photon beam into the detector.

For excitation at Ce M_5 resonance, the Ce M_α and Ce M_ζ emission lines are strongly enhanced and the O and C emission lines are suppressed. The suppression of these emission lines is due to fewer photons being available for excitation of the C and O because they are now being used in the excitation of Ce. For excitation energies above the resonance, the emission from Ce decreases and the emission from O increases and is, once again, more intense than the emission from Ce.

Using the SDD, the excitation-emission matrix was measured for CeO_2 and is shown in Fig. 2.14. The intensities in the matrix have been normalized with respect to the incident photon flux. The partial fluorescence yields of CeO_2 were extracted from this matrix by summing the intensities of the O K_α, Ce M_ζ Ce $M_{\alpha,\beta}$ emission lines as a function of excitation energy. The partial yields of the Ce emission lines are are shown in Fig. 2.15 along with the inverse of the O K_α emission intensity.

Another example of the capability of the SDD is shown by the a wide range excitation-emission matrix for a powdered sample of copper phthalocyanine ($C_{32}H_{16}N_8Cu$) is shown in Fig. 2.16. Several distinct features of the data set are apparent in this plot. The first is are the horizontal lines which correspond to the C K_α emission at 277 eV, the N K_α emission at 392 eV and the Cu L_α emission at 927 eV, as well as faint lines representing the emission from contamination by O at 525 eV and Al at 1560 eV. The second distinct

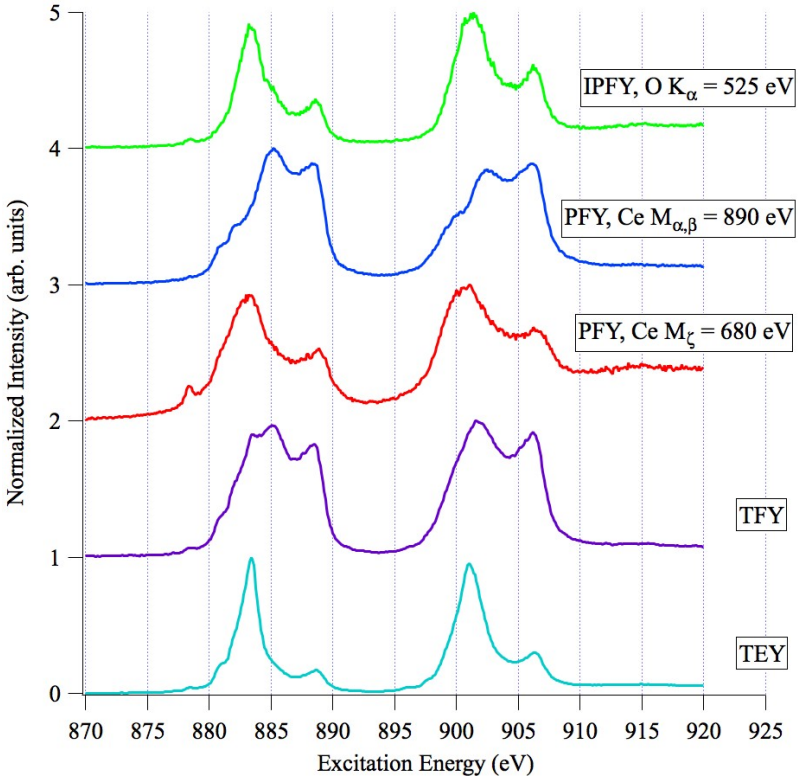

Figure 2.15: The partial yield fluorescence spectra at the Ce M-edge in CeO_2 using the Ce M_ζ and Ce $M_{\alpha,\beta}$ emission intensities. The IPFY, TEY and TFY are also shown.

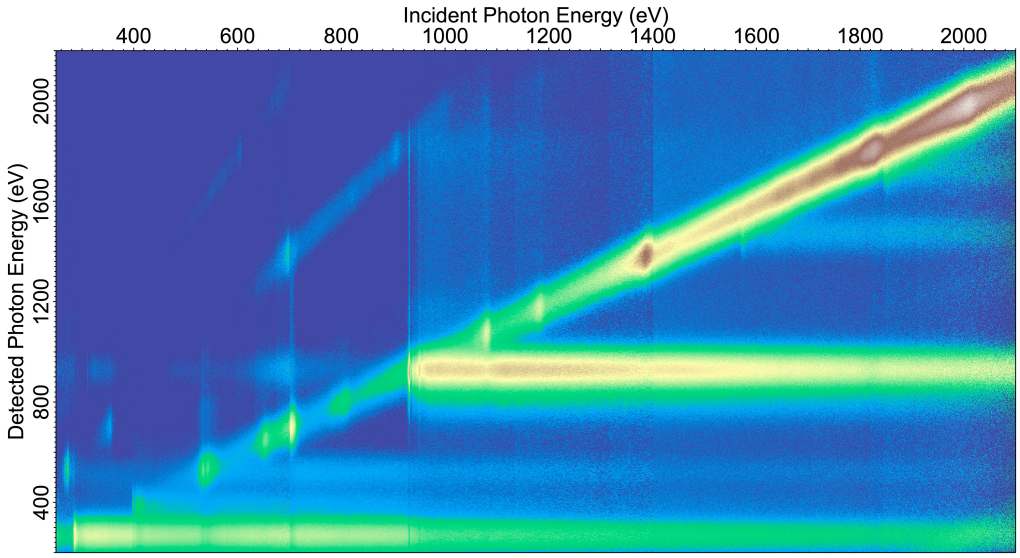

Figure 2.16: The excitation-emission matrix for copper phthalocyanine measured for a wide energy range showing fluorescence and scattering features.

feature is the line at a slope of 1 that corresponds to the elastic scattering of the incident beam from the sample. Additional intensity is seen on lines with slopes of 2 and 3 (barely visible), which is attributed to the scattering of higher order light from the sample. Strong features are seen on the first order scattering line that are attributed to high **q** Bragg scattering. Other counts are seen between the fluorescence and scattering lines and are the result of detector pile up.

Detector non-linearity

The linearity of the SDD refers to the relationship between the number of photons detected, R_{out}, and the number of incident photons R_{in} Typically, detectors that register discrete events have some maximum count rate, R_C, above which, the detector response is no longer linear with respect to the incident photon rate. For XAS measurements the detector must be operated below this count rate to ensure that the measurement of the linear attenuation coefficient does not saturate. A brief discussion of the origins and effects of detector non-linearity as they apply to the use of SDD's for XAS measurements are presented here.

The response of a solid state detector becomes non-linear above a certain count rate because of detector dead time. The dead time in a detector, T_{Dead}, is the amount of time after each event that the detector is not available to record a second event [70]. In an SDD, T_{Dead} is determined by the amount of time spent by the electronics in determining the height of each peak. If another photon is absorbed by the detector while the amplifier is shaping the pulse from the last photon, the second pulse is not correctly registered and R_{out} becomes non-linear with respect to R_{in}. In addition, the dead time restarts with the arrival of the second photon, so as the input count rate is increased further the output count rate decreases. This behaviour is

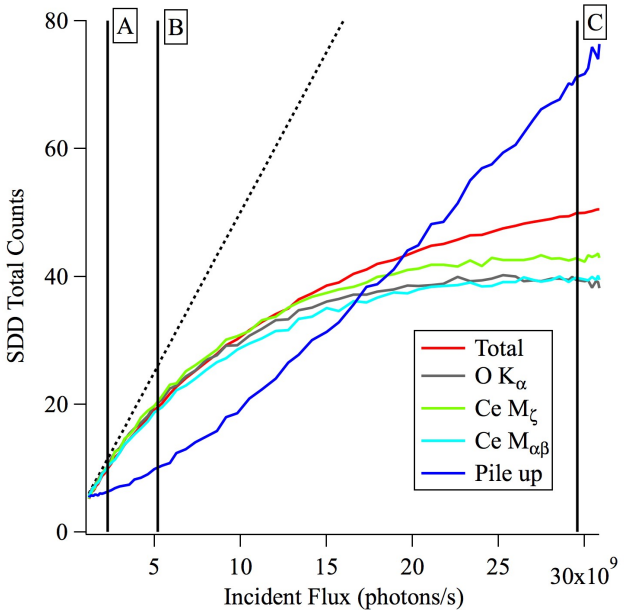

Figure 2.17: The relationship between the flux of 910 eV photons incident on a Ceria sample and the total count rate. The partial yields of the Ce $M_{\alpha,\beta}$, Ce M_{ζ} and O K_{α} emission lines are normalized to the total yield. The dotted line is used to highlight the linear count rate regime. The lines labelled A, B and C indicate the incident flux values used in the XAS measurements shown below.

called paralysis of the detector and is characterized by the following relationship:

$$R_{out} = R_{in} e^{-R_{in} T_{Dead}}. \tag{2.15}$$

When two or more photons are incident on the detector within the dead time of the detector, an effect called pile-up occurs. Pile-up is the output of the sum of the energies of all the photons that arrive within the detector dead time. For instance, if two photons with energies of 535 eV arrive within T_{Dead}, the detector registers them as a single photon of 1070 eV.

The effect of the dead time on the SDD was examined by measuring the x-ray fluorescence spectrum of CeO_2 as a function of the incident photon flux. For this measurement, the incident photon energy was kept constant at 910 eV (above the Ce M-edge) and the undulator was detuned to reduce the flux of the beamline[6]. The incident flux was measured by inserting a calibrated silicon photodiode into the beam as described in Sec. 2.3.4. The relative total fluorescence intensity and the intensities of the Ce $M_{\alpha,\beta}$, Ce M_{ζ} and O K_{α} emission lines are plotted in Fig. 2.17 as a function of the incident flux. The intensity of the pile up is also shown in the plot.

The results of the saturation test showed that the detector output became non-linear when the incident photon flux exceeded 2^9/s, corresponding to a total count rate of 10 kcps. The count rates of the individual emission lines (Ce $M_{\alpha,\beta}$, Ce M_{ζ} and O K_{α}) showed total saturation at an incident photon flux of 2.5^{10}/s.

[6]Detuning the undulator involves setting the gap between magnets to a value that does not provide optimal flux. Detuning can be used to reduce the flux of the beamline without having to modify slit settings or introduce filters.

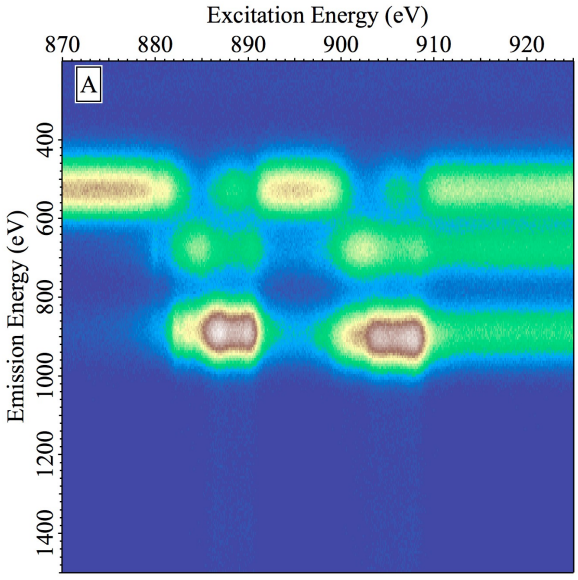

Figure 2.18: CeO_2 excitation-emission matrix measured with no detector saturation. The incident photon flux used in this measurement corresponds to the vertical line A in Fig. 2.17.

A further increase in the incident count rate would be expected to result in a decrease in the partial yield intensities as the paralysis effects become important, but this counting regime was not investigated. The total count rate was observed to continued to increase slowly at high incident flux. This increase was attributed to the growing number of pile up events.

The sensitivity of XAS to detector saturation was tested by measuring the excitation-emission matrix of CeO_2 with varying incident photon intensities. The data in figures 2.18, 2.19 and 2.20 were measured with the incident flux so that the detector count rates were maintained below 15 kcps, 25 kcps and 70 kcps, respectively. The three count rate regimes are highlighted by the vertical lines labelled A, B and C in Fig. 2.17.

The primary effects of detector saturation on the excitation-emission matrices is an increase in the amount of pile-up events that are registered at energies above the energies of the emission lines. A small amount of pile-up is observed in the lowest count rate regime at the Ce $M_{4,5}$ absorption resonances. This pile-up increases for count rates at B and becomes severe at C. At the highest count rates, the saturation appears to modify the shape of the emission profiles.

The Ce partial fluorescence yields from the $M_{\alpha,beta}$ and M_{ζ} emissions and the IPFY were extracted from each of the three excitation-emission matrices in Figures 2.18, 2.19 and 2.20 and are shown in Fig. 2.21, Fig. 2.22 and Fig. 2.23. Saturation effects are apparent indicating the importance of operation of the detector in the linear regime.

Another alternative to operating in the linear regime of the SDD would be to account for the pile up in the detector by modelling the detector response at high count rates. This could allow for pile up correction of each individual x-ray fluorescence spectrum and permit operation of the detector at higher count rates

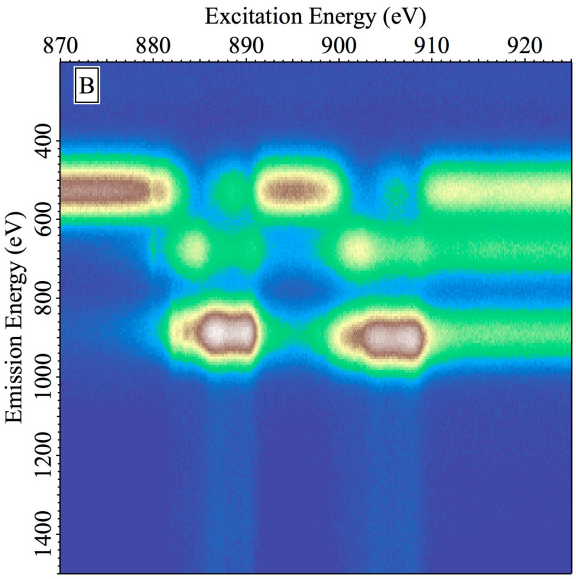

Figure 2.19: CeO_2 excitation-emission matrix measured with the detector experiencing some saturation (vertical line B in Fig. 2.17).

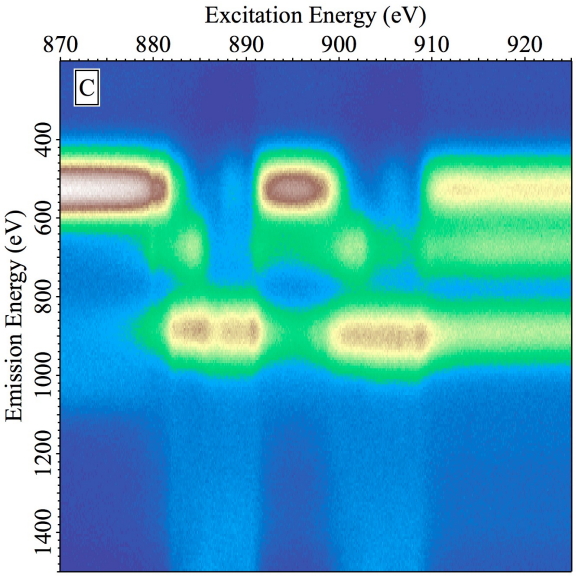

Figure 2.20: CeO_2 excitation-emission matrix measured with severe detector saturation (vertical line C in Fig. 2.17).

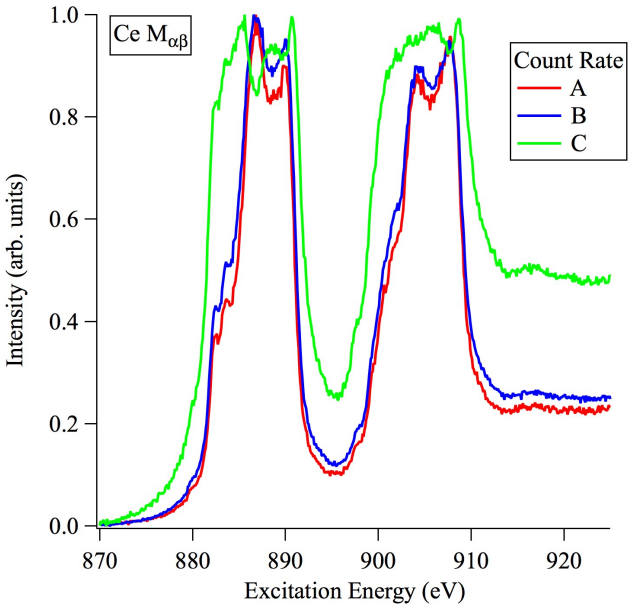

Figure 2.21: The XAS of CeO_2 measured using the Ce $M_{\alpha,\beta}$ emission with the no (A), slight (B) and severe (C) detector saturation.

improving efficiency. This type of correction scheme, well known in x-ray spectrometry [**?**], has not yet been attempted with a silicon drift detector at soft x-ray energies.

2.5.2 Fast Scanning

In order to improve overall efficiency, a fast scanning system was developed for the SGM beamline. Initial tests using the fast scanning system show that good quality absorption measurements can be obtained using continuous energy scanning in a fraction of the time taken for the standard step scanning configuration. The improvements in efficiency facilitate the acquisition of large numbers of absorption spectra in a short period of time and, more significantly, reduce the dose required for a single measurement, mitigating beam damage effects.

The traditional scanning mode for soft x-ray absorption spectroscopy involves step scanning the beamline energy through an absorption edge. On the SGM beamline this involved changing the undulator gap, the grating angle and the exit slit position. Using stepper motors, the positions of the undulator, grating and exit slit could be optimized for a particular energy, then stopped for the acquisition period, then moved again to the next energy. While the step scanning method is suitable for longer acquisition or dwell times, it is very inefficient when dwell times become short in comparison to the time taken to move the beamline components. On the SGM beamline, moving from one energy to the next would take on the order of 1 second. This is due in part to the time taken to accelerate and decelerate the mechanical components involved and in part to the communications overhead involved in ensuring that all components have reached the correct position and have settled. Because the motion took approximately 1 second, reducing the dwell time below 1 second

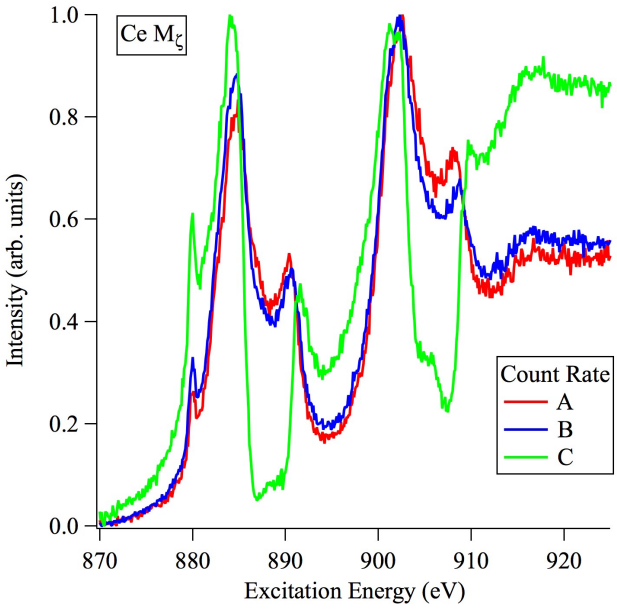

Figure 2.22: The XAS of CeO_2 measured using the Ce M_ζ emission with the no (A), slight (B) and severe (C) detector saturation.

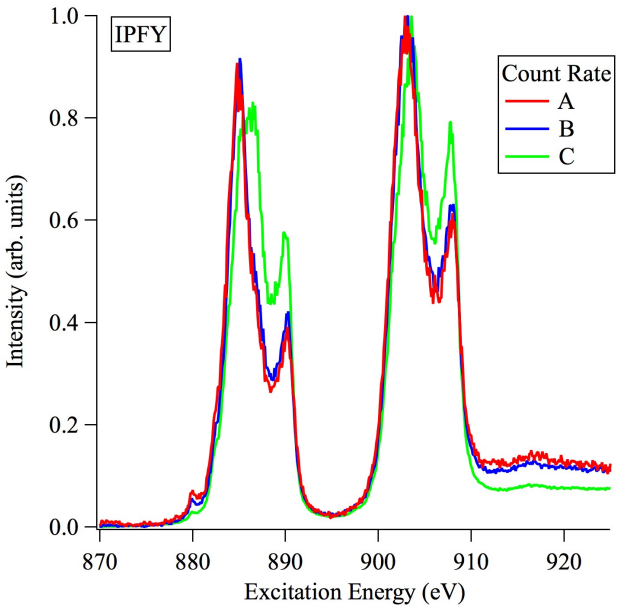

Figure 2.23: The XAS of CeO_2 measured using the O K_α IPFY with the no (A), slight (B) and severe (C) detector saturation.

would begin to reduce the duty cycle of the beamline to below 50 percent. Furthermore, samples were still being exposed to the beam while the mechanical motion was taking place, meaning that the sample was needlessly being damaged by the beam during this time period[7].

The fast scanning approach, also known as slew scanning, was originally developed for performing Quick EXAFS (QEXAFS) [71]. Fast scanning improves the duty cycle of a scan to 100 percent by continuously acquiring signal from the beamline detectors while the undulator and grating motors move at predefined velocities from positions corresponding to the start energy to the final energy positions. The motor velocities are set such that they start and stop at the same times, keeping the photon flux optimized through out the scan. During the scan, the exit slit is kept in a fixed position that corresponds to the intermediate photon energy, providing the best resolution for the intermediate energies of the scan where the finest spectral structure is typically encountered.

Data for a fast scan is acquired from the analog detectors on the beamline (TEY, TFY and photodiodes) using a current amplifier, a voltage to frequency converter and a VME based scalar (counting) card as shown in Fig. 2.24. The scalar card (SIS3820 from Struck Innovative Systeme) is set to count pulses continuously and to fill its onboard buffer with the pulses counted in an interval equal to 1/1000th of the total scan time. So after a 20 second fast scan, for instance, the scalar buffer contains 1000 values for each detector that correspond to the current output from the detector as a function of time (energy), with 20 ms time resolution. The use of the scalar card system ensures that the detector outputs are measured over exactly the same time intervals, which is critical for data normalization, where one channel is divided by another.

The most challenging aspect of the fast scanning system is properly calibrating the energy axis. As the grating motor is continuously moving, the photon energy is also continuously scanning, making it difficult to know the energy for each particular 20 ms time interval. On the SGM, energy calibration is performed by counting the pulses from the grating encoder using additional inputs on SIS3820 scalar card. The mechanical system for rotating the diffraction grating employs an optical encoder which outputs up or down pulses corresponding to rotation of the grating[8]. At the end of the scan, the number of up and down encoder pulses in each time interval is used to compute the change in grating angle, and thus photon energy, corresponding to that 20 ms time period. The new energy axis is the tabulated and output with the corresponding detector data from the scalar buffer.

To test the fast scanning system the Cu L-edge of Cu metal was measured using both the fast scan and the standard step scanning mode. The step scan used an integration time of 1 second per point and a step size of 0.1 eV over the energy range between 920 and 950 eV. The total time for the step scan was 940 seconds, while the fast scan took just 20 seconds, corresponding to a reduction in the dose received by the

[7]While the beamline elements are in motion they are not producing the optimum flux because the undulator and grating are not perfectly co-ordinated. However, for small energy changes, this reduction in flux is as small as a few percent of the total flux, so the samples are still being exposed to significant amounts of radiation during the move phase, resulting in significant levels of beam damage in some samples.

[8]The encoder measures the linear position of the grating sine arm drive which can be related to the grating angle by the length of the arm.

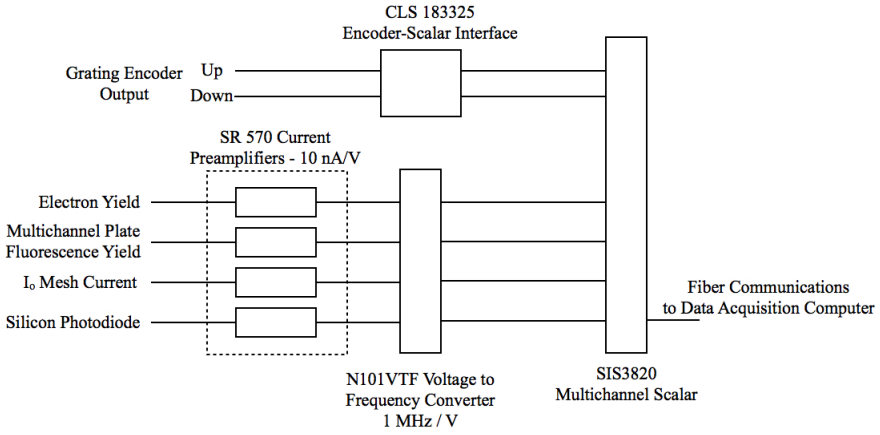

Figure 2.24: Schematic of the electronics used in the fast scanning system used on the SGM beamline at the Canadian Light Source.

sample of approximately a factor of 45.

A comparison of the fast scan and step scan are shown for Cu metal in Fig. 2.25. When the spectra are viewed in full they are indistinguishable. At close inspection, the fast scan data showed some periodic noise which was associated with electrical interference picked up by the signal cabling. This noise could be a limiting factor in the concentration limit for fast scanning but, as shown in Cu metal fast scan data, does not affect the measurement of concentrated samples.

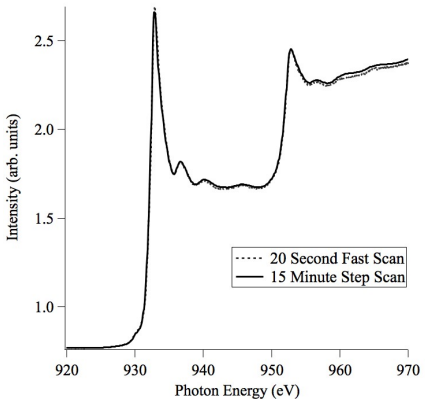

Figure 2.25: A comparison of the Cu L-edge of Cu metal measured with the fast scanning mode and the step scanning mode. Both spectra are measured using TEY.

Fast scanning has become a powerful tool for assessing beam damage effects. The dose levels associated

with standard step scans are very high (on the order of MGy to GGy) and many samples show degradation in the beam. The effects of the beam damage can be observed in the absorption spectra or as the visible modification of the sample. To look for beam damage effects in the spectroscopy, the sample is repeatedly scanned in the same position. With step scanning this is a time consuming test that only provides coarse information and does not determine the extent of the damage that occurs during the course of the initial measurement. Repeated fast scans can be performed in a reasonable amount of time and provide a time resolved picture of the chemical modification of the sample.

The effects of beam damage are shown for Cu acetylacetonate in Fig. 2.26. With increasing dose, the fast scan data shows that there is a beam induced reduction of the Cu^{2+} in the sample. These results highlight the potential for the use of fast scanning for time resolved studies of beam damage effects. They also show that it is possible to obtain good quality absorption spectra from standards before much of the beam damage occurs in a sample.

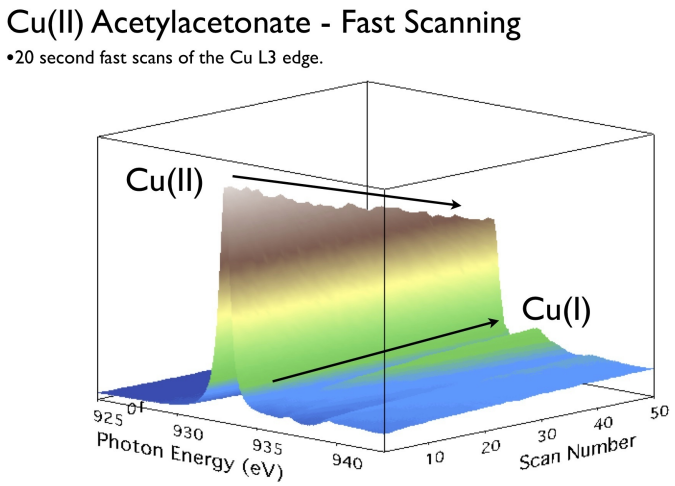

Figure 2.26: A time resolved investigation of the beam induced reduction in Cu Acetylacetonate.

The development of fast scanning modes on the SGM beamline has dramatically improved the efficiency of the beamline. This has led to a much higher sample throughput, allowing for the collection of hundreds of absorption spectra in one hour of beamtime. Plans for new developments in sample preparation methods, sample transfer mechanisms and data processing have been motivated by this improvement in efficiency. Fast scanning is also an important tool for diagnosing and avoiding beam damage effects. While the fast scanning mode is not compatible with all samples and detectors on the SGM beamline, it is quickly becoming the preferred method for measurement in many experiments.

2.6 Conclusions

This section has presented a view of SXAS and XRS and demonstrated that they are two complementary methods for studying the electronic structure through core level excitation. While the bulk of this thesis focuses on data acquired using soft x-rays, a direct comparison of the two methods is presented in Chapter 4.

SXAS allows for the study of the electronic structure by measuring the linear attenuation coefficient of a material. By understanding how the penetration depth of soft x-ray photons changes as a function of the photon energy at and absorption edge, the core hole modified density of unoccupied electronic states can be mapped, permitting the determination of oxidation states and co-ordination number as well as other details relating to the chemical environment of the target element. Transmission measurements directly measure the optical density of the sample and can be performed when a small beam spot and a thin sample are available. When transmission measurements are not possible, the attenuation coefficient can be measured by monitoring the emission of electrons and photons from the sample. Electron yield is easily performed and allows for measurements of the surfaces of conducting samples. Bulk sensitivity for dilute samples can be achieved using total fluorescence yields but saturation becomes a problem for most materials. The recently developed IPFY method allows for bulk sensitive measurements on concentrated samples by examining the non-resonant emission intensity using an energy resolving fluorescence yield detector.

Soft x-ray methods have a number of advantages over techniques that use optical or infrared photons, hard x-rays, electrons or neutrons for electronic property studies. The soft x-ray energy range is commensurate with threshold excitation of the $1s$ electrons in C, N and O and the $2p$ electrons in the transition metals. This makes soft x-rays ideal for element specific studies of many systems with biological or material science relevance. It is possible to produce brilliant soft x-ray beams with a modest synchrotron facility and it is relatively easy and affordable to build beamlines to focus and filter the light for spectroscopy. But soft x-ray techniques have an inherent limitation due to their short penetration depths. In-situ studies are often not possible because one cannot get the x-rays to the sample through the apparatus required to generate the right sample environment. There is currently considerable effort being spent on developing in-situ apparatus for soft x-ray beamlines, but certain studies, such as high pressure SXAS, will likely never be possible.

XRS is a technically challenging technique that can provide access to core level excitation spectra in situations when XAS is not possible. Because it utilizes hard x-ray radiation, the sample limitations imposed by the short penetration length of soft x-rays can be overcome. As discussed in Sec.1.3.2, $\mathbf{q}$ can be chosen to include or reject quadrupole excitations, which can provide additional information on the electronic structure.

XRS has limitations in terms of the spectra resolution and signal to noise ratios achievable. DDSCS signals are small because the inelastic scattering cross sections are small and the energy of the scattered photons must be analyzed, making XRS measurements very time consuming. While it is common to see soft x-ray spectra with resolutions determined by the lifetime broadening of the sample, XRS resolutions are

limited by the bandpass of the hard x-ray monochromators used. For these reasons, XRS is only used in situations where **q** dependent spectra are needed or the in-situ capabilities required are not compatible with soft XAS.

The following chapters discuss the application of core excitation spectroscopy to the study of two different systems. In Chapter 3, TEY measurements of the C K edge in the linear polyacenes are provided. Chapter 4 provides TEY, TFY, IPFY and XRS measurements of different iron oxide minerals. These results will demonstrate the application of the spectroscopic methods presented in this chapter and present some new developments that have been in relation to the measurement and analysis of core level excitation spectroscopy.

Chapter 3

X-ray absorption spectroscopy of the polyacenes

3.1 Introduction

The previous chapter discussed various problems associated with true measurement of the linear attenuation coefficient at soft x-ray energies and introduced several improvements. The focus of this chapter is to evaluate one of the key theoretical issues associated with the modelling of XAS: the effect of the core hole on the overall electronic structure. As discussed in Chapter 1.4, the evaluation of the effect of multi-electronic excitation on absorption structure is a major difficulty for the current modelling methods. One way to approach the problem is to systematically evaluate the absorption structure of several very similar molecules. If the experimental resolution is sufficient, subtle differences in the XAS can be unambiguously assigned to the the multi-electronic excitations in the core excited system.

The linear polyacenes represent a suitable system for such a study. The system is comprised by aromatic hydrocarbon molecules that are composed of different numbers of hexagonal carbon rings, joined in a linear arrangement. Their general chemical formula is $C_{(4n+2)}H_{(2n+2)}$ where n is the number of rings in the structure. The first five members, shown in Fig. 3.1, benzene(n=1), naphthalene(n=2), anthracene(n=3), tetracene(n=4) and pentacene(n=5), are readily isolated, while the larger members, hexacene(n=6), heptacene(n=7), octacene(n=8) and nonacene(n=9), have shown to be stable only while in a matrix [72].

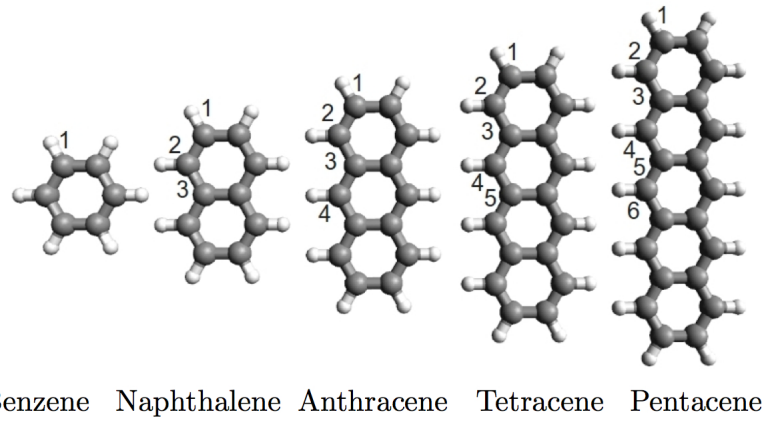

Figure 3.1: The linear PAH series. The numbers indicate the nonequivalent carbon atoms.

The PAHs have been intensely studied for their applications as precursors in industrial scale chemical synthesis and organic electronic applications [73]. Recent observation of the infrared absorption signature of anthracene has been detected in interstellar gas clouds which has led to speculation that polyacenes may represent some of the earliest building blocks of organic life forms [74, 75]. The known carcinogenic effects of the polyacenes on humans, combined with their production as a by-product of the combustion or organic material, has meant that they have been of interest from a health science and environmental perspective [76]. In addition, the polyacenes represent an interesting model series for understanding the role of conjugation length on electronic structure, which makes them interesting from a fundamental point of view [77]. They have been studied as building blocks of other unique carbon based systems like graphene and buckyballs.

Pentacene and tetracene have received considerable attention in the past decade due to their relatively high electron and hole mobilities which make them candidates for use in organic electronic devices. The possibility of using conductive organic molecules for making novel devices like "smart" windows, flexible displays, electroluminescent plastics, inexpensive solar cells and printable electronics has motivated many studies of the electronic structure of pentacene [78]. In general, these studies have been performed in order to understand or characterize the charge transport in pentacene thin films so that an improvements in organic field effect transistor (OFET) performance can be realized.

Soft x-ray absorption spectroscopy at the C K-edge has been a widely used tool for the examination of the electronic structure in the polyacenes. Early XAS work performed on diamond and graphite was able to demonstrate the sensitivity of the technique to the bonding network in carbon based materials, allowing for the clear discrimination of sp^3 and sp^2 bonding [79, 80]. At the same time, the geometry dependence in the XAS of graphite was verified to be useful for determining the orientation of the graphene sheets of which it is composed. Both the chemical and structural sensitivity of XAS have made the technique an important method for understanding the polyacenes.

In the late 1980's, x-ray absorption studies on both gas phase and condensed benzene were able to observe the density of unoccupied π states and their modification as a result of chemical interaction with surfaces [81, 82], and were accompanied by similar works on naphthalene [83]. Electron energy loss spectroscopy (EELS) measurements of benzene and naphthalene were also published in the 70's and 80's by Brion and Hitchcock [84, 85]. The development of the spherical grating monochromator class of beamline in the 1980's by C.T. Chen at Brookhaven National Laboratory (BNL) allowed for the first high resolution XAS spectra of benzene that clearly showed coupling between the nuclear and electronic degrees of freedom as a vibronic structure [81]. The work by Ma *et. al.*, and several subsequent studies, showed how vibronic structure in high resolution measurements could be used to probe the effects of the core hole on the structure of small organic molecules [86, 87].

In the 1990's, the first x-ray absorption measurements of tetracene and pentacene were published in a study on the localization in π^* orbitals [88]. Using ab initio calculations, Ägren, Vahtras and Carravetta evaluated the XAS of benzene, naphthalene, anthracene, tetracene and pyrene in an effort to characterize

the absorption spectrum of graphite [77]. This 1995 work remains as one of the only attempt to understand the x-ray absorption of the polyacenes as a function of molecule size (number of conjugated benzene rings). Several size dependent trends were discovered in the calculated spectra, as will be discussed in the following section. But the comparison between theory and experiment was hampered because of the low resolution measurements available at the time. No consideration of the effects of the vibronic structure on the absorption structure was given in this study because the fine structure could not be observed in the data used for the analysis.

In the last decade other high resolution XAS measurements of select polyacenes have appeared in the literature. From 2000 to 2005, several papers appeared that demonstrated that the vibronic structure needed to be considered in the interpretation of high resolution absorption at the C K edge. In 2004, Minkov *et. al.* were able to show that fine structure in the high resolution gas phase XAS of naphthalene was composed of the vibrationally broadened excitations of two of the non-equivalent carbon atoms (atoms 1 and 2 in Fig. 3.1) [89]. A subsequent comparison of the gas phase absorption spectrum of deuterated and non-deuterated naphthalene by Ḧubner *et. al.* provided clear evidence of the role of vibronic coupling in the formation of these spectra [90]. In Ḧubner's work, the $1s \rightarrow \pi^*$ region of the naphthalene spectra was simulated by the addition of two benzene lineshapes, showing very good agreement. This type of analysis was also successfully used by Urquhart and collaborators to reproduce the absorption spectra hydrogenated and deuterated polystyrene [91]. Work on the high resolution gas phase XAS of pentacene has also suggested that vibrational structure plays a role in the XAS of the large polyacenes [92], but a similar analysis was never applied in that case.

The recent work on the polyacenes indicates that accurate interpretation of high resolution x-ray absorption spectra requires consideration of the vibrational broadening associated with the excitation of all non-equivalent carbon atoms in the molecule. To date, this type of analysis has only been performed on naphthalene, so the role of vibronic coupling on the XAS spectra of anthracene, tetracene and pentacene is still not understood. In the first portion of this chapter, the x-ray absorption of the polyacenes will be presented and interpreted in terms of vibrationally broadened excitations. A detailed assignment of the spectra of each molecule will be performed and the energies of the adiabatic transitions from the non-equivalent carbon sites to the LUMO will be extracted.

The susceptibility of the PAHs to beam damage effects will also be discussed in detail. Beam damage effects are often a problem for accurate measurement of the XAS or organic compounds because the measured spectra will represent the combined absorption cross section of the original molecule and the damage product. The damage study of the PAHs was particularly important because, at the time the measurements were made, the fast scanning capability of the SGM beamline (see Sec. 2.5.2) was not yet available. Therefore, numerous test had to be carried out to determine that the absorption measurements were accurate. The chemical modification of the PAHs under exposure to soft x-ray radiation will be examined.

In order to evaluate the multi-electronic excitation effects the extracted transition energies and intensities

for each molecule will be compared to values calculated using DFT. The DFT calculations will employ a model of the core hole where the final state electronic structure has been allowed to relax around a full and half charge in the 1s orbital. The comparison will focus on relative changes in the measured and calculated energies and intensities for excitations from the two end carbon atoms (atoms 1 and 2 in Fig. 3.1). A discussion on how the molecule size affects the core hole screening will be presented.

The final portion of this chapter will focus on factors affecting the application of tetracene and pentacene for use in devices. While they have good electronic properties, these polyacenes have been shown to be susceptible to oxidation, particularly at the organic-electrode interface, that can deteriorate their operational characteristics [93]. An evaluation of the sample stability will be performed by comparison of the XAS spectra measured as a function of absorbed radiation dose. XAS from tetracene thin films prepared in-situ and ex-situ will also be compared to determine the effect of exposure to air. This work is provided to improve the utility of XAS for future characterization studies of tetracene and pentacene devices and to determine to what level surface oxidation can affect the samples.

3.2 Experiment

3.2.1 Sample Preparation

The polyacenes are almost pure carbon so the distortion in their fluorescence yield spectra due to saturation effects is strong. The IPFY measurement method is not an option at the C K-edge because no suitable bystander element is available. For these reason, all solid state XAS measurements had to be made using the TEY from the sample.

To ensure that the TEY method was suitable for the PAHs several different sample preparation methods were tested. Of primary concern was the potential for sample charging or chemical modification of the sample surface. Charging could result in a smearing of the spectrum and/or a large exponentially decaying background. If the surface of the sample was interacting with air the TEY measurements could be distorted by the presence of the chemically distinct C. Also of interest was the effect of the sample substrate on the spectral fine structure and the for potential sample contamination resulting from the preparation methods.

The most basic preparation method involved the direct application of the as received powdered samples to double sided carbon tape. The powder or polycrystalline samples were pressed onto the carbon tape in a thick layer to reduce or eliminate the contribution of the signal from the tape. This carbon tape method is standard practise for measuring powders on soft x-ray beamlines, but is not commonly employed when C K-edge measurements are being made because of the potential for a signal contribution from the C in the tape.

Samples were also prepared by dispersion of small amounts of powder on Au coated Si substrates. In this method, developed at the CLS for the measurement of dilute carbon samples, carbon free substrates are prepared by thermally evaporating Au onto N-type Si wafers [94]. The clean substrates show no C K-edge

signal when measured as prepared. Small quantities of anthracene, tetracene and pentacene were suspended in water and pipetted onto these substrates. The liquid was allowed to evaporate in air, leaving a thin, non-uniform layer of sample on the carbon free substrate, which was then loaded into the end station for measurement.

To obtain thick layers of naphthalene on the clean gold substrates, a liquid deposition method was used. In this method, polycrystalline naphthalene was placed on the substrate which was then placed on a hot plate. The substrate temperature was increased until the sample liquefied, at which point the substrate was removed from the heat source. The naphthalene then recrystallized on the gold surface and was loaded into the end station for measurement. The sample had to be cooled to prevent evaporation in the 10^{-8} Torr measurement chamber.

Samples of tetracene and pentacene were also prepared using both in-situ and ex-situ thermal evaporation methods. For the ex-situ measurements, a calibrated Knudsen cell was used to deposit thin films of different thickness on silicon and clean gold surfaces at high vacuum [10]. The ex-situ samples were removed from the preparation chamber and exposed to air during transportation to the CLS and storage. The in-situ measurements were executed by attaching a purpose built evaporation chamber directly to the SGM beamline. Sub-monolayer, monolayer and multi layer thin film samples of tetracene and pentacene were prepared on silicon (111) surfaces and measured without removal from the vacuum system [95].

The Knudsen cell, also referred to as an effusion cell, was specially developed for use with organic materials. Two tanatalum inserts are used to ensure that the sample is not emitted in clusters and the emission rate could be held constant. The cell and the measurement arrangement for the in-situ experiment are shown in Figure 3.2. The sample substrate is rotated to face the effusion cell for sample deposition and then rotated to face the x-ray beam for measurement.

3.2.2 Sample Purity

All samples were prepared from compounds purchased from Sigma Aldrich and measured without any further chemical treatment. For each sample, the purity quoted by the supplier was 99.9%. As XAS measurements are element specific, sample contamination was only going to be a concern if the contaminants contained carbon or were chemically interacting with the carbon in the sample. A sample could, for instance, be a physical mixture of tetracene and a non-carbon containing compound, and there would be no effect on the resulting C K edge spectra aside from a reduction in the signal intensity. Furthermore, for a carbon containing impurity to have an impact on the measured spectrum it would have to be present in significant quantities. This is due to the fact that the integrated intensities in an absorption spectrum are roughly proportional to the number of atoms of the target element that are present in the sample.

Sample purity was also confirmed using optical microscopy. The distinctive colours of the samples (naphthalene is white, anthracene is yellow, tetracene is orange and pentacene is deep purple), along with the absence of obvious inclusions, helped to confirm sample purity.

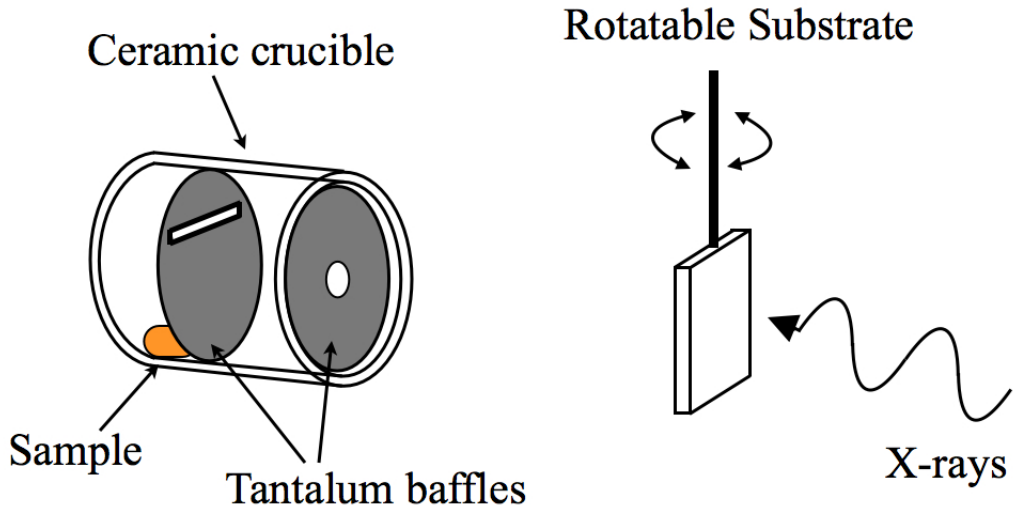

Figure 3.2: Sketch of the sample preparation setup for in-situ NEXAFS measurements of tetracene and pentacene.

Finally, the in-situ measurements results confirmed the purity of the tetracene and pentacene samples. In the in-situ measurements, the temperature of the Knudsen cell was controlled such that the vapour pressure of the sample was just below the pressure in the chamber, allowing other, more volatile contaminants to evaporate. After almost an hour, the temperature was raised to bring the vapour pressure of the sample to a level just above the chamber pressure, causing the sample to sublimate. A comparison between the in-situ and ex-situ XAS measurements, as well as the spectra reported in the literature, provided confidence that the samples as obtained from the vendors, were not contaminated.

3.2.3 X-ray absorption measurement

The XAS measurements of the polyacenes were performed on the Spherical Grating Monochromator (SGM) beamline at the Canadian Light Source. High resolution was critical to these measurements so the beamline was carefully optimized to provide a beam with a photon energy bandwidth of approximately 20 meV. This was achieved by setting the energy dispersive exit slit of the beamline to 5 μm. The energy calibration of the beamline was checked by measuring the XAS of pure carbon monoxide gas, which has a narrow C1$s \rightarrow \pi^*$ peak with a well known transition energy of 284.7 eV [96, 97].

Due to their high vapour pressures, benzene and naphthalene were measured in the gas phase using a

parallel plate gas cell. The photoionization current was used to monitor the absorption. In these measurements, the attenuation coefficients can be considered to be proportional to the photoionization occurring in the gas volume traversed by the beam, provided the gas pressure is sufficiently low so that total absorption of the x-rays does not occur. To avoid this saturation effect, gas pressures were maintained at 10^{-3} Torr in the cell.

For the gas phase samples, variation in the incident photon flux was accounted for by dividing the photoionization yields by the drain current recorded from a gold mesh immediately upstream of the gas cell. Normalization of the electron yield from the solid samples was performed by dividing the measurements by the output of a silicon photodiode [58], measured in a consecutive scan, as described in Sec. 2.3.4.

The thin film samples were measured with the x-rays incident on the sample at 54.7^o with respect to the sample normal. With this orientation (known as the magic angle), the polarization dependent effects in the absorption will vanish, leaving a spectrum that is indistinguishable from one made on a sample with random orientation [7]. The highly oriented pyrolytic graphite (HOPG), used as a reference compound, was also measured in this geometry.

3.2.4 Sample Stability

The ability for soft x-rays to cause radiation damage in organic samples is a known phenomenon that had to be considered in this study [98]. The high x-ray intensities available at third generation light sources have the potential to deposit doses in the hundreds of MGy in a single scan. At these doses, organic samples are expected to undergo chemical modification, resulting in a change in the near edge structure [99]. The resulting measurements would then be a weighted sum of the spectra of the damage product and the target molecule, complicating the interpretation of the spectra. As this study was looking for subtle effects in the fine structure of the XAS, it was important to understand if the spectrum was altered due to the presence of damage products. It was also desirable to understand how the damage proceeded within the time scale of a single scan and the chemical nature of the damage products. The stability of the sample surface when exposed to atmospheric conditions was also of interest as this may impact the performance of devices fabricated from these materials.

To evaluate the radiation damage process in the solid state polyacenes, successive XAS measurements were made at a single spot on each sample. Comparison between the spectra of 'pristine' samples and damaged samples was used to determine if chemical modification was occurring. Particular attention was paid to tetracene, where beam damage effects were examined in great detail. Liquid helium cooling was used to bring the tetracene sample to 20 K to evaluate the effect of temperature on sample stability.

To improve the relevance and the transferability of the beam damage work done here, an estimate of the dose was required. Dose, defined here as the amount of energy deposited in a given mass of sample, is difficult to calculate in soft x-ray spectroscopy, primarily due to the large modification of the linear attenuation coefficient at the absorption edge. The strong change in the penetration depth means that a much higher

dose is being delivered to the surface of the sample when excited at or above resonance, as compared to the dose delivered for pre-edge excitation. For instance, the calculated penetration depth ($1/e$) for tetracene below the $1s$ ionization potential is 4 μm, while above the ionization potential, it is 0.2 μm [18]. This means that the effective dose for a given exposure to excitation energies above the edge is 20 times greater than dose accumulated in the same exposure time below the edge. This energy dependence in the dose is illustrated in Fig. 3.3. When the sample is excited at the resonance energy, the linear attenuation coefficient is maximized and so the dose rate at the sample surface is also maximized. Therefore, in order to obtain an accurate dose estimate it was necessary to account for the energy dependence in the dose rate.

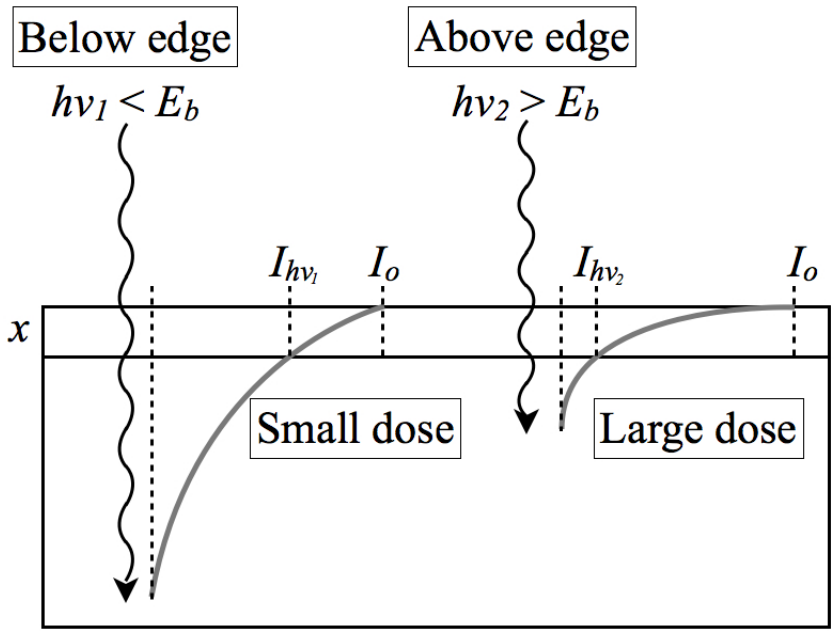

Figure 3.3: When excited below the absorption edge ($h\nu_1$), the beam penetrates much more deeply into the sample than when excited above the edge ($h\nu_2$). This leads to more energy being deposited into the same volume of sample a strong energy dependence in the dose rate.

The energy dependence in the surface (50 nm) dose was considered by combining the tabulated attenuation coefficients for tetracene below and above the C $1s$ resonance and the measured absorption spectrum. Given that the dose, D, in units of Gy, is given by

$$D = \frac{\text{Energy Absorbed}}{\text{Mass}}, \tag{3.1}$$

the dose delivered in the top x nm of sample in a t second exposure, can be written as

$$D(h\nu, x) = \frac{h\nu\, e^{-}\, (I_o - I_x)}{Ax\rho} t. \tag{3.2}$$

Here, I_o is the incident flux, I_x is the flux remaining at a depth x, A is the area of the beam and ρ is the density of the absorber. From Beer's law,

$$I_o - I_x = I_o(1 - e^{-\mu(h\nu)x}) \tag{3.3}$$

so Eq. 3.2 becomes

$$D(h\nu, x) = \frac{h\nu\, e^-\, I_o(1 - e^{-\mu(h\nu)x})}{Ax\rho}t. \tag{3.4}$$

The expression is valid for $x < 1/\mu(h\nu)$ and takes into account the sharp change in penetration depth of the photons at resonance.

Typically, XAS measurements are acquired by moving to a given photon energy and dwelling for a certain time, then moving to the next energy, and so on. So an estimate of the dose that is accumulated in a scan, can be constructed as a sum of all of the individual steps in a scan:

$$D_{tot} = \sum_{i=0}^{N} D(h\nu_i, x) = \sum_{i=0}^{N} \frac{h\nu_i\, e^-\, I_o(1 - e^{-\mu(h\nu_i)x})}{Ax\rho}t. \tag{3.5}$$

In this relationship, t is assummed to be constant for each step and N is the number of points in the XAS scan.

Finally, to account for the strong energy dependence in the attenuation coefficient $\mu(h\nu)$, absorption data was used. For each term in the sum in Eq. 3.5, the correct value for $\mu(h\nu)$ was determined from the measurement by normalizing to tabulated values for the attenuation coefficient below and above the absorption resonance. This method was used in Sec. 3.3.4 to estimate the total dose accumulated in one scan and the dose accumulated up to any point in a scan.

3.2.5 Calculation

The *ab initio* molecular orbital calculation of the transition energies and intensities were performed using DFT as implemented in the StoBe package [100]. Atomic coordinates for the polyacenes were obtained from x-ray diffraction studies [101–103]. The ground state carbon atoms were described using the Effective Core Potential (ECP) approximation [104] with Z_{eff}=4. Model core potential basis sets with 5 Gaussians were used for modelling the core potential and 6 s type Gaussians for describing the core orbitals. Huzinaga type orbital basis sets, formed from contractions of 5 s Gaussian Type Orbitals (GTO) and 4 p GTOs, were used to initiate the self consistent field (SCF) calculations. To improve convergence, auxiliary basis sets were used with 5 s and 2 *spd* functions to model the exchange-correlation functionals, as well as 5 s and 2 *spd* functions to fit the electron density. The excited carbon atom was described by the *iglo-iii* basis set of Kutzelnigg et al. [105], which is a relatively large set with 11 s and 7 p functions, plus 2 d functions, contracted to 7 s, 6 p, and 2 d for calculation.

Several alternative basis sets were tested to determine the effect of initial atomic wave function descriptions on the SCF convergence and results. Specifically, benzene and tetracene spectra were computed using

different orbital, auxiliary and core potential contractions. Variations in the transition energies and intensities were noted for different basis sets but these discrepancies were small compared to the difference between measurement and calculation.

The relaxation of the non-interacting electrons that results from core hole formation was modelled within the one electron picture, using the FCH and HCH methods. In the HCH method, equivalent to the Slater Transition State (STS) method, the screening effects of the core hole are approximated by removing half of an elementary charge from the $1s$ orbital and allowing for full relaxation of the electronic structure. In the FCH method, a full elementary charge is removed from the $1s$ orbital and the electronic structure was allowed to fully relax. Kohn-Sham orbitals determined using the HCH and FCH methods were then employed in the generation of transition energies and intensities according to Eq. 1.6.

The results of a given calculation consisted of a set of transition intensities and energies from each non-equivalent carbon atom in each of the molecules. These were then summed to give the discretized absorption spectrum for the given molecule. While it is customary to apply broadening to the calculated transition elements in an attempt to mimic the effects of lifetime and instrumental broadening, the calculation results in this study have not been broadened. This was done because strong vibronic effects, previously observed in benzene [96] and naphthalene [89], could not be adequately represented by a simple symmetric line shape approximation. A full vibronic analysis using the linear coupling model has been shown to be useful for calculating the vibrational broadening [89], but this calculation was not performed as part of this work. The DFT results are thus presented as the raw transition dipole moments.

In each of the FCH and HCH results, the energy axes were rigidly shifted so that energy of the transition from the core level of the carbon site labelled 'C2' matches with the apparent observed transition energy for this atom. The application of this energy shift was well justified given the appearance of a central, three peak motif that appears in all of the absorption spectra that is attributed to the sum of the transitions from the 'C1' and 'C2' molecules. This assignment will be explained further in the following section.

3.3 Results

3.3.1 Trends in the polyacene XAS

The normalized XAS spectra of the polyacenes are shown in Fig. 3.4 along with that of graphite. Note that only the $1s \rightarrow \pi*$ region of the graphite spectrum is visible in the energy range between 283 and 290 eV. In this region, all of the polyacenes exhibited a multi-featured and well resolved fine structure. This was contrary to graphite, where only a single broad peak was observed in the $1s \rightarrow \pi*$ region.

When viewed as a series, the polyacene XAS showed several trends that developed with the molecule size. The first was the evolution of a double manifold structure, originally described by Ägren and collaborators [77], with a steadily growing separation between the manifolds as the molecule size increased. These two manifolds were assigned to transitions of the C $1s$ electrons into the LUMO and the LUMO+1. The second

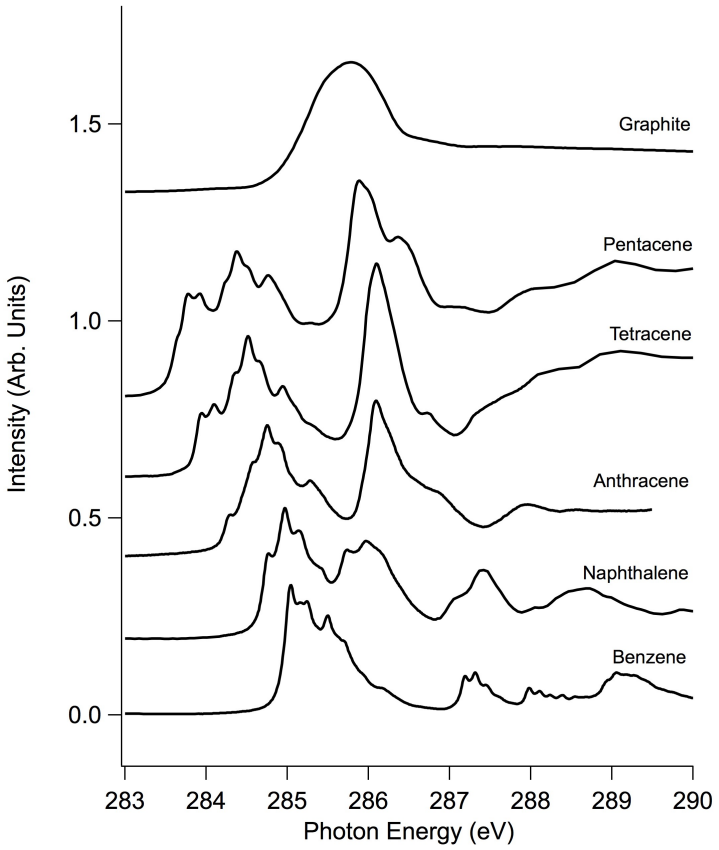

Figure 3.4: High resolution absorption spectra of the polyacenes and graphite.

trend was the observation of fine structure in the low energy manifold that grew in complexity for the larger molecules. This fine structure exhibited a three peak motif that persisted through out the spectrum of all multi-ring molecules. This three peak motif is highlighted in Fig. 3.5. The third trend was a general increase in the width of the first manifold with increasing molecule size. The fourth trend was a reduced average π^* transition intensity relative to the intensity of the post edge for increasing molecule size.

3.3.2 Lineshape simulation

To evaluate the role of vibronic coupling in the formation of the low energy π^* regions of each absorption spectrum, these spectral features in naphthalene, anthracene, tetracene and pentacene were modelled by a sum of the benzene $1s \rightarrow \pi^*$ lineshapes. The intensities, positions and number of individual transitions were manually varied to obtain the most reasonable fit with the experimental data. The simulated spectra and the results of the calculations are shown along with the measurements and a diagram of each molecule in Figures 3.6, 3.7, 3.8 and 3.9.

In Figures 3.6 thru 3.9 colour coding has been used to show the core excited site involved in each of

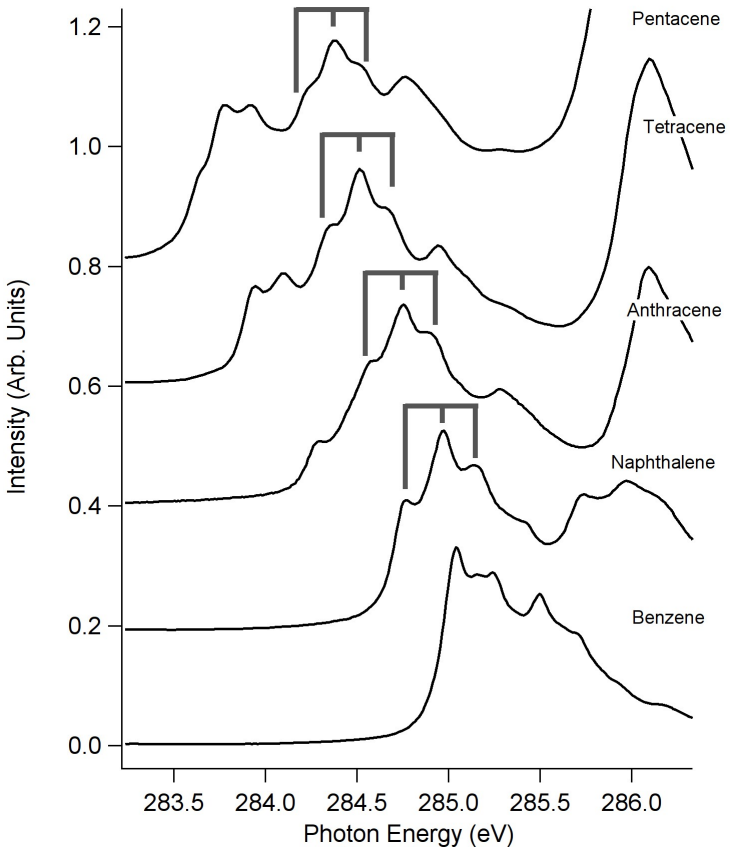

Figure 3.5: Low energy manifold of the linear polyacene NEXAFS. A three peak motif is repeated for all multi-ring structures.

the transitions(C1=black, C2=blue, C3=green, C4=cyan, C5=red, C6=pink), where the numbering scheme is shown in Fig.3.1. Note that the numbering scheme used in this study differs from the scheme used by Ågren *et al.* [77] and other subsequent studies [89, 90, 92], where the non-equivalent sites are labelled from C1 to C6(for pentacene) starting with the atom at the centre position and moving toward the atom at the end position. In the current work, the C1 label refers to the end atom, and increasing numbers are used to represent the more central atoms. This labelling scheme seems to provide a more consistent reference: C1 represents the same type of site (end atom) in all molecules in this new scheme, while in the numbering used by Ågren, C1 represents a different type of site in each molecule.

3.3.3 Lineshape fit results

The naphthalene spectrum was fit with two benzene lineshapes separated by 0.22 eV and with an intensity ratio of 1.12 (C2/C1). This agreed well with the results of Hůbner *et al.* who predicted an energy separation of 0.20 eV and an intensity ratio of 1.06. Calculated transition intensities were found to be zero for the C3 atom and non-zero for the C1 and C2 atoms. The FCH method calculated an energy separation of 0.22 eV (C2-C1) and an intensity ratio of 1.09 (C2/C1). Using the HCH approximation, the separation was calculated

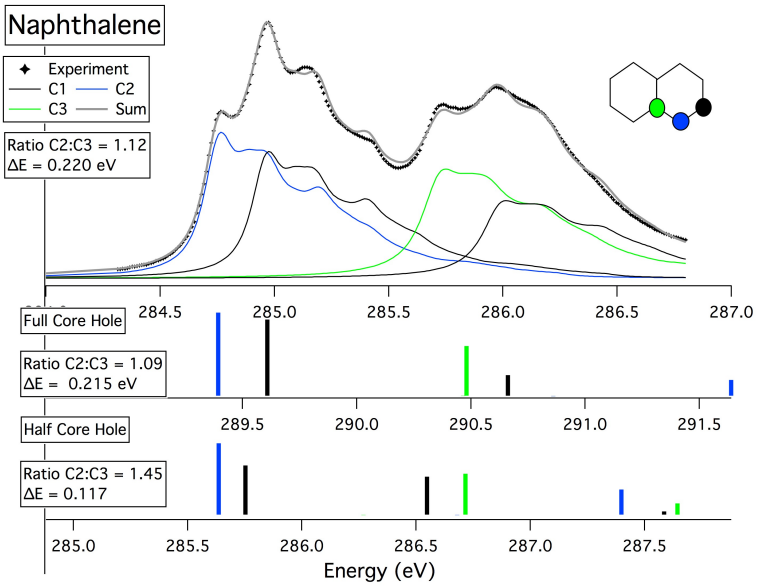

Figure 3.6: Comparison of the naphthalene NEXAFS, the simulated spectra using two benzene lineshapes and the DFT calculation results.

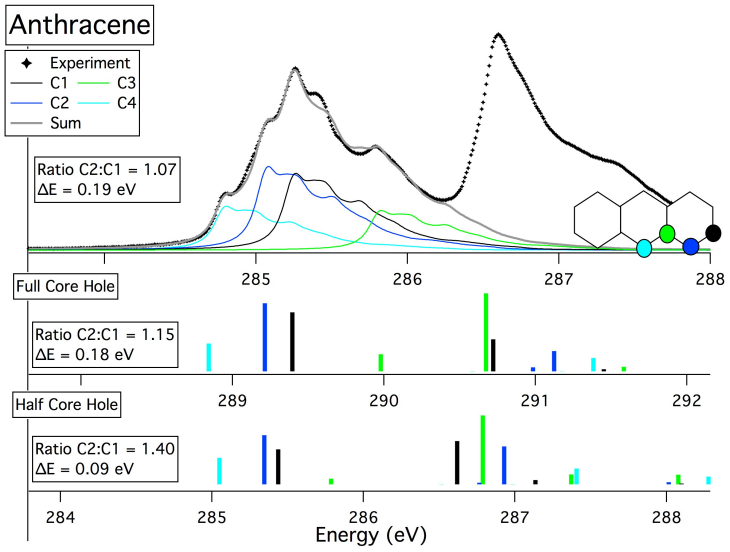

Figure 3.7: Comparison of the anthracene NEXAFS, the simulated spectra using four benzene lineshapes and the DFT calculation results.

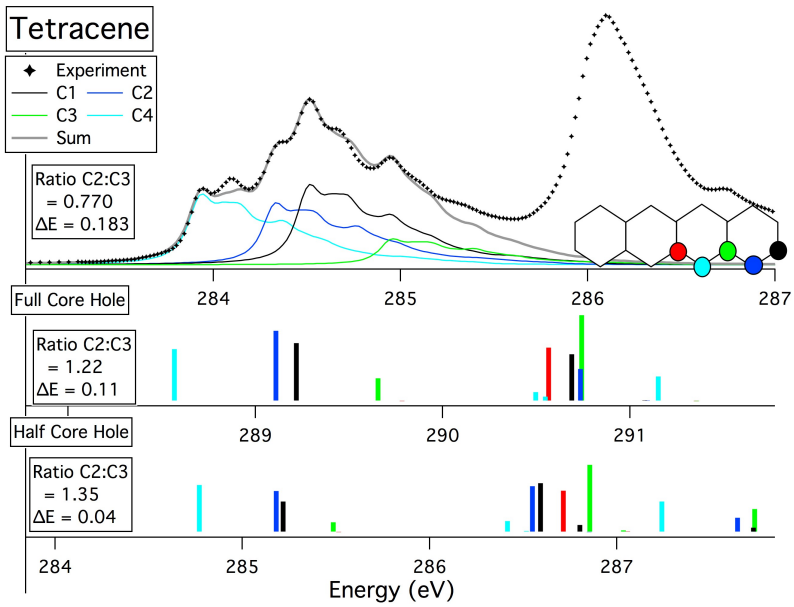

Figure 3.8: Comparison of the tetracene NEXAFS, the simulated spectra using four benzene lineshapes and the DFT calculation results.

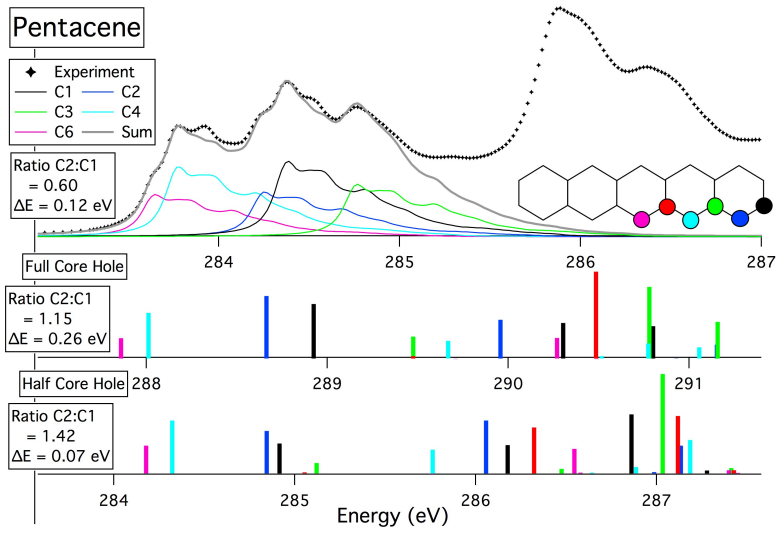

Figure 3.9: Comparison of the pentacene NEXAFS, the simulated spectra using five benzene lineshapes and the DFT calculation results.

to be 0.12 eV (C2-C1) and the intensity ratio was calculated to be 1.45 (C2/C1).

For naphthalene, the second manifold, corresponding to transitions into the LUMO+1, was also fit with two benzene lineshapes. Additional broadening was required to obtain qualitative agreement with the shape of the second manifold. Both the FCH and HCH results showed transitions from the C1 and C3 atoms, but the order was reversed. The FCH calculation showed that the C3 atom had a lower transition energy than the C1 atom, while the HCH calculation showed that the C1 atom had the lower transition energy. Note that the LUMO+1 manifold was not fit for the larger molecules because the fine structure could not be observed in those peaks.

In order to fit the anthracene LUMO manifold, four benzene lineshapes were required, corresponding to transitions from each of the four non-equivalent C sites. Particular interest was given to the the centre two transitions which generated the three peak motif, as highlighted in Fig. 3.5. The energy difference between these two transitions was measured to be 0.19 eV and their intensity ratio was 1.07. Both the FCH and HCH calculations showed non-zero transition intensity for all four non-equivalent C sites. Both methods indicated that the C4 atom resulted in the lowest energy transition, followed by the C2 and C1 atoms, in a similar arrangement as was seen in naphthalene. The C3 atom had the highest calculated transition energy. FCH calculation results agreed well with the values obtained from the fit for the centre two transitions (C1 and C2). An energy spread of 0.18 eV and an intensity ratio of 1.15 were calculated. The HCH method calculated an energy spread of 0.09 eV and an intensity ratio of 1.40.

The LUMO region of the tetracene XAS spectrum was also fit with four benzene lineshapes. While there are five non-equivalent C atoms in tetracene, fitting the spectrum with five lineshapes gave a qualitatively worse fit than when using only four. The energy separation between the two transitions giving rise to the three peak motif was 0.18 eV and their intensity ratio was 0.77. The calculation results indicated a zero intensity transition for the C5 atom. The FCH calculation results showed an energy spread of 0.11 eV and an intensity ratio of 1.22, while the HCH calculation gave a spread of 0.04 eV and a ratio of 1.35.

For pentacene, a reasonable fit of the LUMO manifold was obtained using five benzene lineshapes. The two transitions generating the three peak motif were found to be separated by 0.12 eV and had an intensity ratio of 0.60. Similar to the results for tetracene, the pentacene calculations showed zero intensity for the excitation of the C5 atom. The results of the FCH calculation produced a C2-C1 energy difference of 0.26 eV and an intensity ratio of 1.15. The corresponding values for the HCH calculation were 0.07 eV and 1.42.

The transition energies and intensities for all molecules have been tabulated in Tab. 3.1 and Tab. 3.2. A summary of the energy differences and intensity ratios of the transitions making up the three peak motif are tabulated in 3.3. The ionization energies for the non-equivalent sites in each molecule were also extracted from the DFT calculations and are shown in Tab. 3.4 and Tab. 3.5.

		Benzene	Naphthalene	Anthracene	Tetracene	Pentacene
	Exp	285.35	284.98	284.75	284.51	284.39
C1	FCH	289.84	289.61	289.40	289.22	288.93
	HCH	286.20	285.75	285.44	285.22	284.92
	Exp		284.76	284.56	284.33	284.25
C2	FCH		289.39	289.21	289.11	288.66
	HCH		285.64	285.35	285.18	284.85
	Exp		NA	285.32	284.96	284.77
C3	FCH		290.46	289.98	289.65	289.47
	HCH		286.27	285.79	285.49	285.12
	Exp			284.29	283.93	283.77
C4	FCH			288.84	288.57	288.01
	HCH			285.05	284.77	284.32
	Exp				NA	NA
C5	FCH				289.78	289.47
	HCH				285.51	285.05
	Exp					283.65
C6	FCH					287.86
	HCH					284.18

Table 3.1: Measured and calculated transition energies of the lowest energy π^* excitations in electron volts. Measured values are extracted from the spectral line shape simulations in Figures 3.6,3.7, 3.8 and 3.9. Calculated values were obtained from the DFT calculations described in Sec. 3.2.5

		Benzene	Naphthalene	Anthracene	Tetracene	Pentacene
	Exp	1.0000	1.0000	1.0000	1.0000	1.0000
C1	FCH	0.0180	0.0129	0.0105	0.0090	0.0078
	HCH	0.0170	0.0083	0.0063	0.0049	0.0039
	Exp		1.1477	1.0880	0.7692	0.5909
C2	FCH		0.0141	0.0121	0.0109	0.0089
	HCH		0.0120	0.0088	0.0067	0.0055
	Exp		0.0000	0.5162	0.3240	0.6939
C3	FCH		0.0001	0.0031	0.0035	0.0032
	HCH		0.0000	0.0010	0.0016	0.0014
	Exp			0.5718	0.8778	0.9226
C4	FCH			0.0099	0.0081	0.0065
	HCH			0.0094	0.0077	0.0068
	Exp				0.0000	0.0000
C5	FCH				0.0000	0.0004
	HCH				0.0000	0.0002
	Exp					0.5604
C6	FCH					0.0058
	HCH					0.0072

Table 3.2: Measured and calculated transition intensities. Measured values are normalized to the C1 atom transition intensities. Theoretical values are reported as the total dipole oscillator strengths in atomic units (1 a.u. $= 8.47835281 \times 10^{-30} Cm$).

	Naphthalene	Anthracene	Tetracene	Pentacene
	Energy Difference (eV)			
Exp	0.22	0.19	0.18	0.12
FCH	0.22	0.18	0.11	0.26
HCH	0.18	0.09	0.04	0.07
	Intensity Ratio			
Exp	1.12	1.07	0.77	0.60
FCH	1.09	1.15	1.22	1.15
HCH	1.45	1.40	1.35	1.42

Table 3.3: Energy differences and intensity ratios for the two transitions making up the unique three motif feature that persists through the spectra of naphthalene, anthracene, tetracene and pentacene.

	Benzene	Naphthalene	Anthracene	Tetracene	Pentacene
C1	290.96	290.65	290.47	290.36	290.20
C2		290.64	290.47	290.37	290.16
C3		291.04	290.82	290.68	290.49
C4			290.27	290.09	289.83
C5				290.69	290.47
C6					289.73

Table 3.4: The ionization energies in electron volts calculated by DFT for each of the non-equivalent C atoms in benzene, naphthalene, anthracene, tetracene and pentacene using the HCH.

	Benzene	Naphthalene	Anthracene	Tetracene	Pentacene
C1	298.12	297.40	296.95	296.62	296.18
C2		297.36	296.95	296.67	296.01
C3		297.82	297.36	297.00	296.80
C4			296.60	296.16	295.57
C5				297.04	296.81
C6					295.48

Table 3.5: The ionization energies in electron volts calculated by DFT for each of the non-equivalent C atoms in benzene, naphthalene, anthracene, tetracene and pentacene using the FCH.

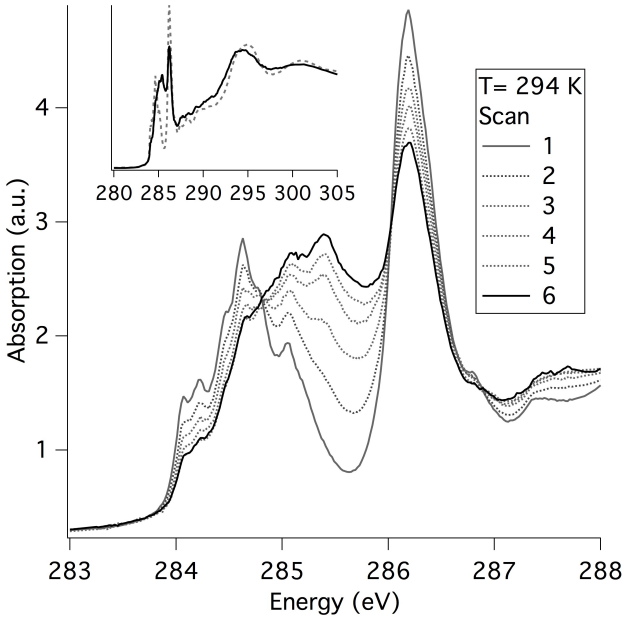

Figure 3.10: Six tetracene NEXAFS measured at the same point on the sample at room temperature. The inset compares the first and sixth scans over a wide range.

3.3.4 Radiation Damage

The stability of the samples under soft x-ray radiation was examined by measuring six subsequent XAS spectra taken on the same sample position. These results are shown for tetracene at room temperature in Fig. 3.10 and at 20°K in Fig. 3.11. The insets in each figure show wide range scans comparing the first and the sixth scans. Visible inspection of the samples after measurement revealed a brown discolouration where they had been exposed to the beam.

The XAS of the room temperature spectra show a decrease of intensity in both the LUMO and LUMO+1 manifolds accompanied by an increase in absorption in the inter-manifold region around 285.4 eV. Isosbestic points are observed at 284.8 eV, 286.1 eV and 286.9 eV. In the cooled spectra, the same trend and isosbestic points are observed but the overall change in the absorption is not as pronounced. In both the cooled and room temperature measurements there is only a small amount of change in the extended region of the spectra.

The XAS of the damage products were generated by subtracting the XAS of the first scan from each of the subsequent spectra. Before subtraction, each spectrum was normalized to the tetracene signal in the first scan by using the intensity of the first peak at 284.1 eV. The resulting difference spectra are shown in Figures 3.12 and 3.13. The XAS of polystyrene is also included in the plot to highlight the similarities between it and the damage product spectrum.

A close inspection of the lowest energy peaks in the tetracene spectrum (Fig. 3.10) revealed that the amount of tetracene producing the electron yield signal was decreasing in each scan, supporting the hypothesis that the mass fraction of tetracene in the sample was being reduced as the tetracene was being converted

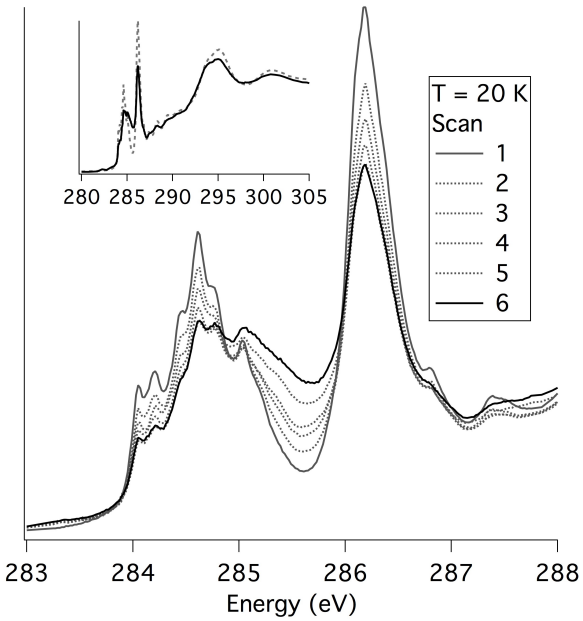

Figure 3.11: Six tetracene NEXAFS measured at the same point on the sample at 20K. The inset compares the first and sixth scans over a wide range.

into the damage product. This was determined by extracting the signal intensity at the first peak (284.1 eV) above the pre-edge signal intensity (280.3 eV). The first scan had a peak intensity of 1.22 and the last scan had an intensity of 0.70, which suggests that 40% of the tetracene is no longer present during the last scan. Note that these measurements were made in electron yield mode so they only represent what is occurring in the top 3 to 5 nm of the sample. The same analysis for the cooled sample yielded similar a result, showing a reduction of 35% in intensity from the first scan to the last. The inset spectra in Fig. 3.10 show the first and last scans with a wider energy range. As the undamaged and damaged sample spectra, in both the case of the room temperature and cooled measurements, have roughly the same intensity well above the ionization potential, it was determined that the total amount of carbon in the sample remained close to the same throughout the measurement process.

The reaction products, both for the room temperature and the cooled tetracene sample, showed a strong resonance at 285.4 eV, followed by peaks at 287.5 eV and 289 eV. A broad resonance appeared at 293 eV for the room temperature sample and at 295 eV for the cooled sample. All of the features in the difference spectra were consistent with those in the XAS of polystyrene, digitized from [106], and could be assigned to C=C and C-H π^* resonances. These main features are also present in the absorption spectra of condensed benzene [7] and poly(α-methylstyrene) [106].

The accumulated dose was estimated taking into account the sharp change in penetration depth of the x-rays at the resonance using the relationship in Eq.3.5. Because the measurements were made using the TEY they are only sensitive to the surface region of the sample and the dose calculation only needed to consider the dose delivered to the top 50 nm of the sample. For 50 nm of tetracene, the tabulated transmission was

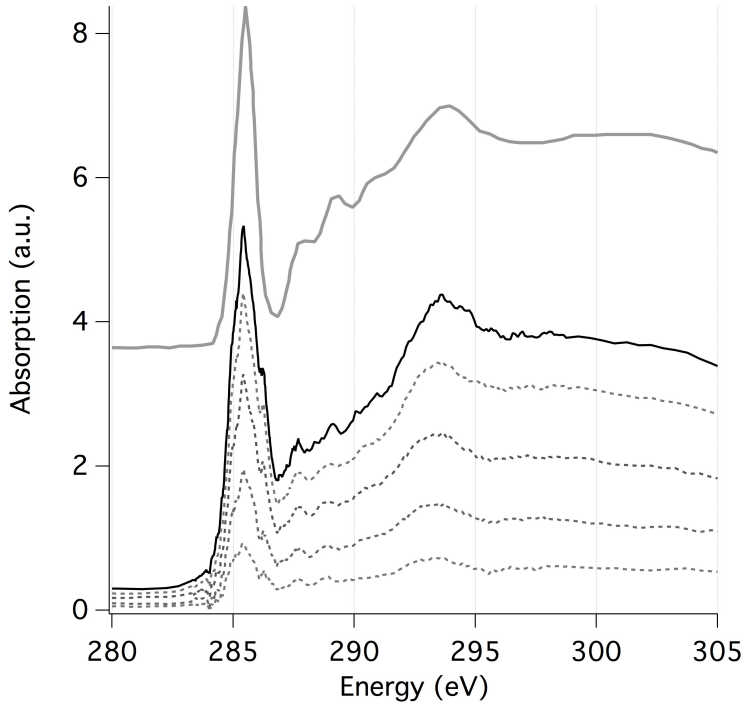

Figure 3.12: Difference spectra for the room temperature tetracene sample.

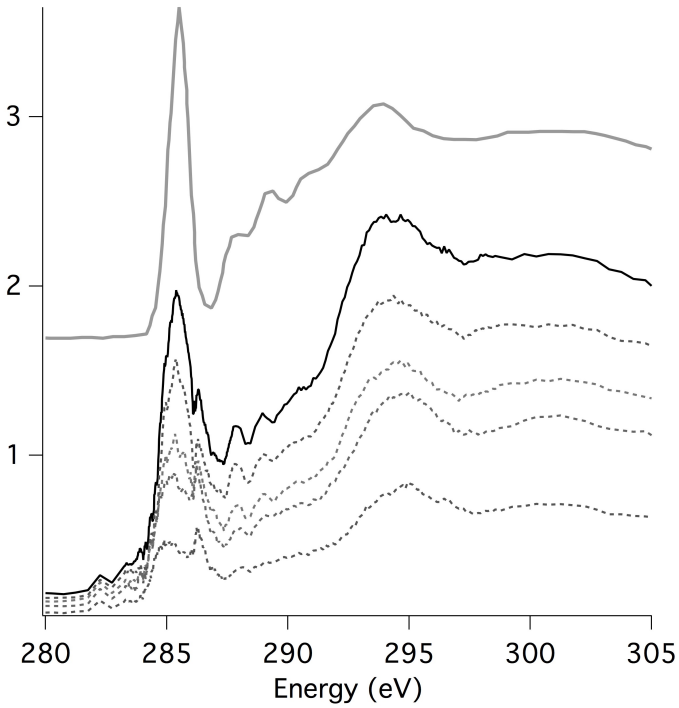

Figure 3.13: Difference spectra for the tetracene sample cooled to 20K.

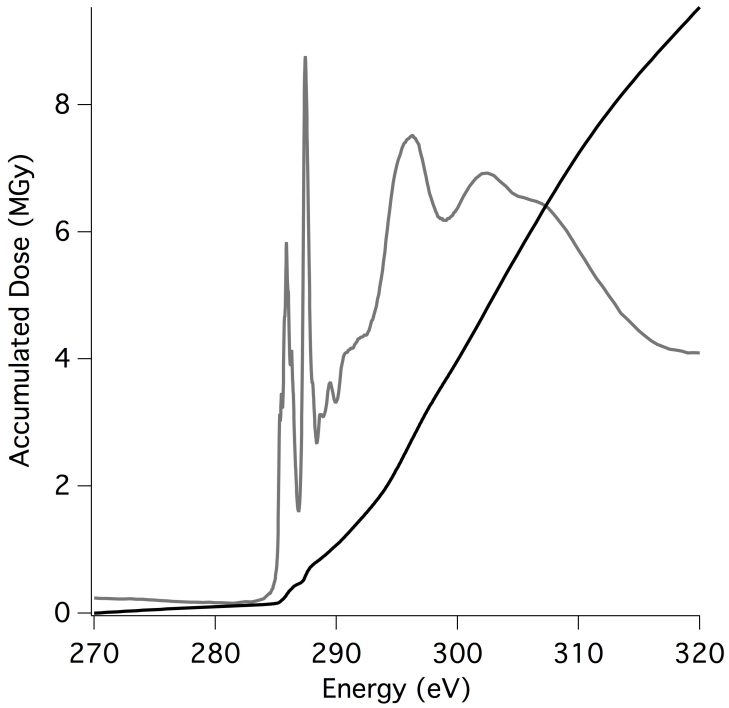

Figure 3.14: The estimated accumulated dose in the top 50 nm of a tetracene sample as a function of photon energy (black). Also plotted is the measured absorption cross section with arbitrary units (Gray).

approximately 99% when excited below the edge ($\rho = 1.19\frac{g}{cm^3}$, $\mu = 0.25\mu m^-1$) [18]. The beam spot size at the endstation was approximately 1 mm x 0.1 mm and the flux delivered was 1×10^{11} photons per second for the high resolution measurements performed. Using these parameters, the pre-edge dose, D, in a 1 second exposure was calculated to be

$$D_{1s}(270\text{eV}) = \frac{270\text{eV} \cdot 1.6 \times 10^{-19}\frac{\text{J}}{\text{eV}} \cdot 1 \times 10^{11} \cdot \left(1 - e^{-0.25\mu m^{-1} \cdot 50 \times 10^{-9}}\right)}{(0.1 \times 10^{-3}\text{m} \cdot 1 \times 10^{-3}\text{m} \cdot 50 \times 10^{-9}\text{m}) \cdot 1.19 \times 10^{3}\frac{\text{kg}}{\text{m}^3}} = 9\text{kGy} \tag{3.6}$$

Above the edge, the tabulated transmission through 50 nm of tetracene was 78%, which resulted in a post-edge dose of 191 kGy for a 1 second exposure.

To estimate the absorbed dose rate as a function of energy (or time) in a scan, Eq. 3.4 was used. The value for μ was generated by normalizing the tetracene XAS to the tabulated pre and post edge attenuation coefficients at 270 and 320 eV [18]. The accumulated dose was then calculated by integrating the absorbed dose rate, according to Eq. 3.5. This result is shown in Fig. 3.14 along with the tetracene absorption spectrum. While the total dose accumulated in the top 50 nm of the sample was 9.5 MGy, the dose delivered during the scan of the pre-edge was only 0.2 MGy.

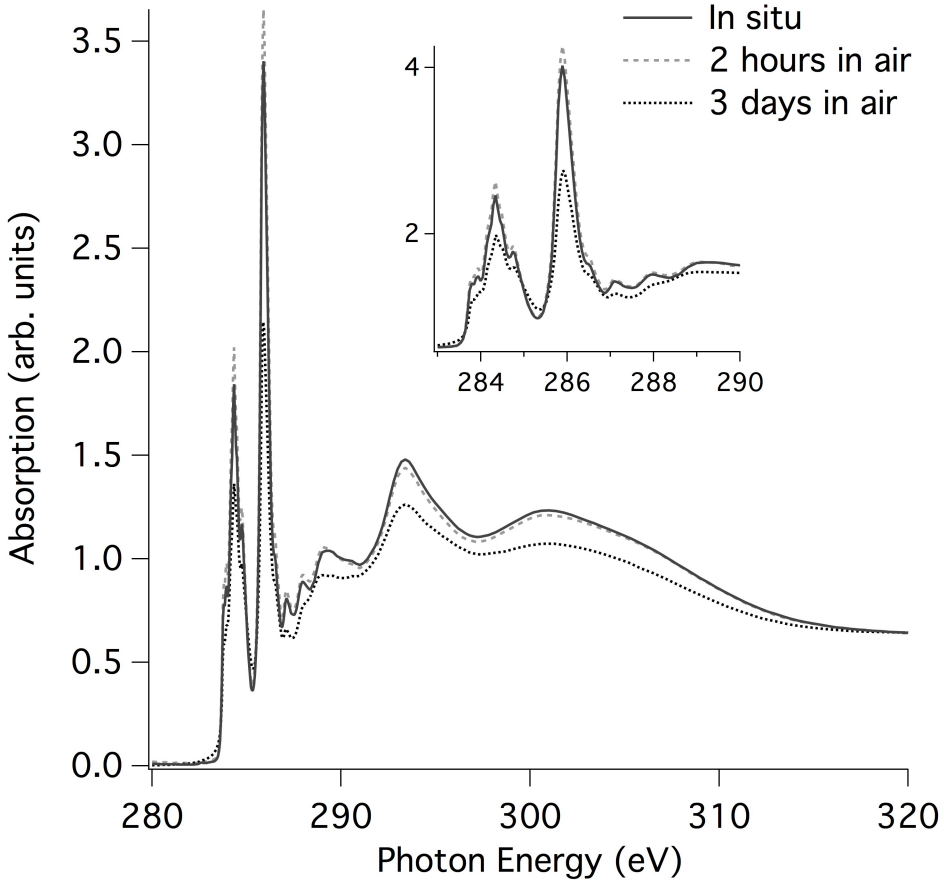

Figure 3.15: Comparison between the NEXAFS spectrum of a tetracene thin film prepared in-situ and the same film after exposure to air for 2 hours and 3 days. The inset shows the 283 to 290 eV region of the spectra in more detail.

3.3.5 Ex-situ versus in-situ measurements

To examine the stability of the surface of polyacene thin films, the SXAS spectra of a tetracene thin film was recorded in-situ, after exposure to air for two hours, and after exposure to air for three days. The three spectra, recorded with the beam incident at the magic angle, are compared in Fig. 3.15. The XAS of the sample removed from the vacuum for two hours showed almost no difference compared to the in-situ measurement. There were, however, differences between the XAS prepared in-situ and the measurement taken after three days of exposure to air. A reduction in the π^* intensity relative to the post-edge was observed along with modification of the peaks in the 288 to 292 eV portion of the spectrum.

3.3.6 XRS of the polyacenes

The XRS of the full linear PAH series have not been measured, but the XRS of benzene and naphthalene and several other polyacenes have been reported by Bergmann et al. in their study on asphaltenes [107]. Using a photon energy between 6 and 10 keV at ID-18 of the APS, Bergmann and collaborators were able to

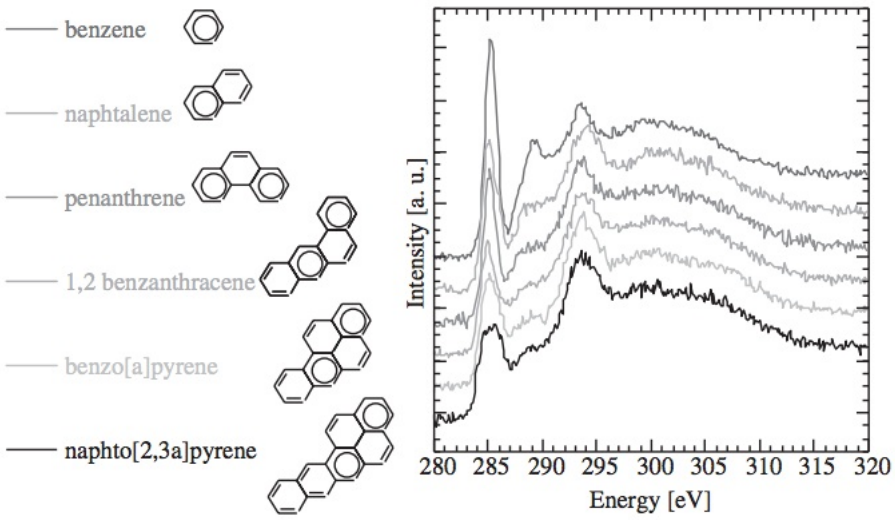

Figure 3.16: The XRS of several PAHs. Reprinted with permission from [107].

measure XRS at the C K-edge with a resolution between 1 and 2 eV. Their measurements, shown in Fig. 3.16, suggest that XRS can be a useful technique at differentiating different organic compounds in asphaltenes. The primary advantages of XRS for these types of studies are the assurance of bulk sensitivity and the ability to study samples under ambient conditions or using in-situ apparatus.

While the XRS measurements of Bergmann and collaborators are good for basic chemical speciation, they lack the resolution necessary to examine the multi-electronic effects that are of interest in this thesis. The benzene and naphthalene spectra in Fig. 3.16 do not exhibit any of the vibronic effects and chemical separation that is clearly observed in the XAS. In fact, the XRS measurement of naphthalene is not even able to resolve the two separate LUMO and LUMO+1 manifolds. Furthermore, XRS measurements require long integration times, likely 8 hours or more, to achieve reasonable signal to noise levels. This is in stark contrast to XAS measurement, which typically take no more than 1/2 hour and have been demonstrated to be achievable in 30 seconds or less using the fast scanning mode on the SGM. Future development of XRS instrumentation at low emittance storage rings like PETRA III in Hamburg and NSLS II at Brookhaven National Laboratory on Long Island may allow for faster measurement times and higher resolutions. But until these capabilities are demonstrated, XRS measurements at the C K-edge lack the resolution necessary for detailed studies of core hole effects.

Rings	Nonequivalent Sites	C1$s \rightarrow \pi^*_{LUMO}$ Transitions	DFT FCH	DFT HCH
1	1	1	1	1
2	3	2	2	2
3	4	4	4	4
4	5	4	4	4
5	6	5	5	5

Table 3.6: The number of rings in the linear polyacenes and the number of transitions measured and predicted by DFT.

3.4 Discussion

3.4.1 Contributions from non-equivalent carbon sites

The C $1s \rightarrow \pi^*$ regions of the SXAS spectra recorded for benzene, naphthalene, anthracene, tetracene and pentacene showed a progressing double-manifold structure with an energy separation that increased as a function of the number of conjugated benzene rings. By comparing the measured and calculated transition energies these two manifolds can be assigned to transitions from the C $1s$ electrons on the non-equivalent sites into the LUMO and the LUMO+1. It was also apparent that not all non-equivalent sites contributed to the first manifold. The two end atoms, C1 and C2, contribute to the LUMO peak in all molecules, forming the salient three peak feature in all spectra. The C3 does not contribute to the naphthalene spectrum but does contribute in the formation of the spectra of the other three larger molecules. In both tetracene and pentacene the C5 atom does not contribute. The number of observed transitions and the number of non-equivalent carbon sites are summarized for each polyacene in table 3.6.

The absence of the transition intensity from certain atoms in the polyacenes can be shown to result from the symmetry of the LUMO. In the case of anthracene, the LUMO for the core excited state exhibits a node at the C3 position resulting in no overlap for the integral described in Eq. 1.9. This is shown in Fig. 3.17 where the wavefunction of the LUMO from the FCH DFT calculation is plotted on top of the molecular structure. A similar situation is encountered for the C5 atom in tetracene and pentacene, as shown in Fig. 3.19 and Fig. 3.20.

It should be noted that the symmetry of the molecule is not the same as the symmetry of the LUMO involved in the transition, as the latter has been broken by the formation of the core hole. The symmetry breaking is most pronounced in anthracene when excited at the C3 site. As shown in Fig. 3.17, wavefunction intensity is shifted toward the C3 site, overlapping slightly with the C1s at C3. This results in a small contribution to the LUMO manifold in the absorption spectrum as shown in Fig. 3.7.

The level of agreement between the observed and calculated number of transitions supports the validity

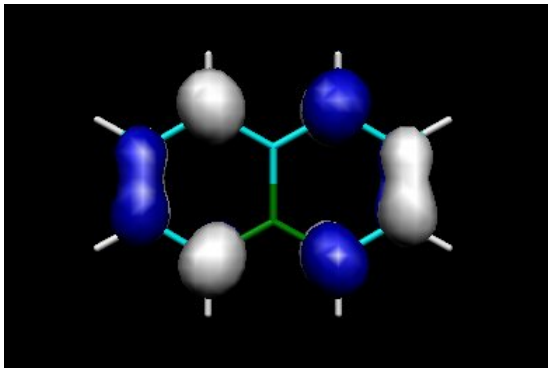

Figure 3.17: The LUMO of naphthalene. The electronic structure has been fully relaxed around a core hole at the C3 atom shown with green bonds. There is no overlap of the C1s of the C3 site and the LUMO.

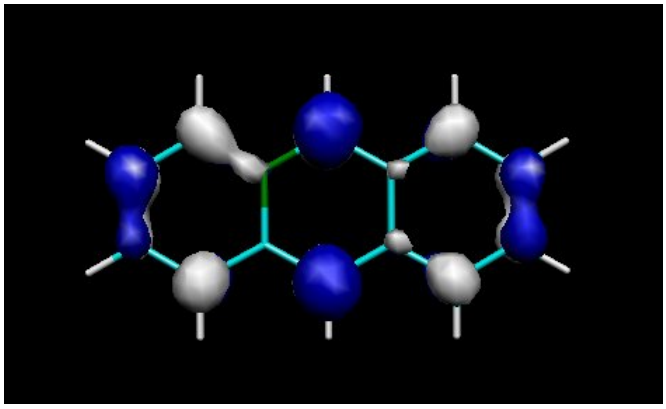

Figure 3.18: The LUMO of anthracene. The electronic structure has been fully relaxed around a core hole at the C3 atom shown with green bonds. Overlap of the C1s of the C3 tom and the LUMO is observed giving rise to transition intensity from this atom in the LUMO manifold.

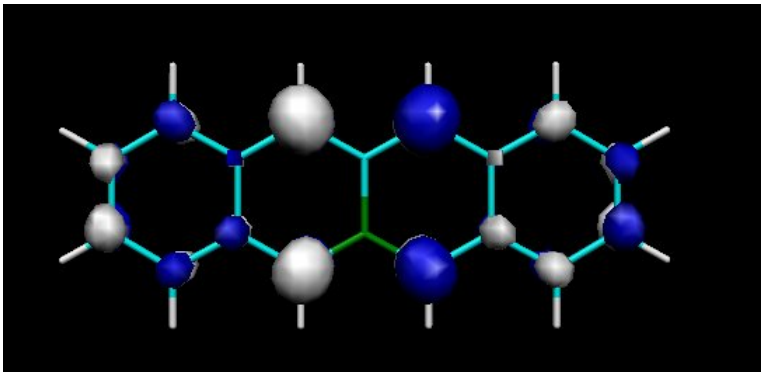

Figure 3.19: The LUMO of tetracene calculated with the FCH approximation for a core hole at the C5 atom shown with green bonds. No overlap of the C1s of the C5 site and the LUMO is observed leading to no transition intensity for the C5 atom in the LUMO manifold.

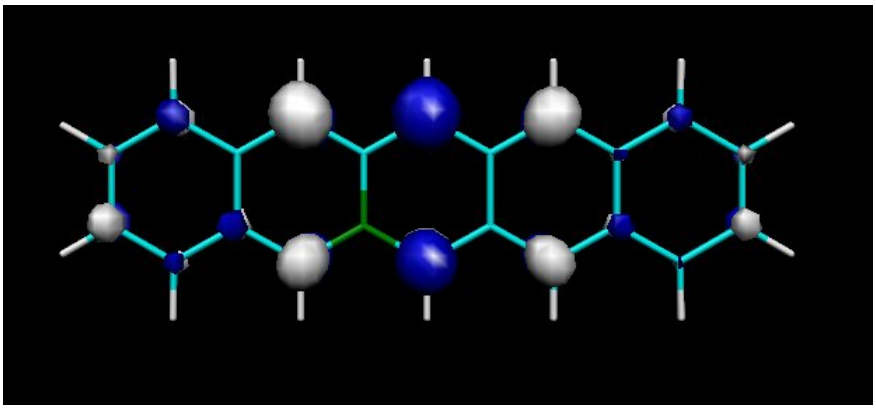

Figure 3.20: The LUMO of pentacene. The electronic structure has been fully relaxed around a core hole at the C5 atom shown with green bonds. As in tetracene, the C1s of the C5 site and the LUMO do not overlap.

of the DFT approach for determining the structure of the LUMO in the polyacenes. Differences in the relative transition intensities and energies are expected because of the one electron treatment of the electronic structure reconfiguration resulting from core hole formation. But, for the polyacenes, it is clear that the level of the orbital reconfiguration is approximated well by the FCH method. If the effect of the core hole was much weaker than predicted by the calculation, transitions from the C3 site in anthracene would not be observed in the measurement. If the core hole effects were much stronger, transitions from the C5 site in tetracene and pentacene would likely be observed.

It is interesting to note that the occurrence of suppressed transitions is partially responsible for the observation of the fine structure in these spectra. Without this suppression, an additional, chemically shifted, resonance would be added to the LUMO manifold of naphthalene, tetracene and pentacene. This additional transition and the corresponding vibrational broadening would likely wash out some of the observed fine structure, making the assignment of the spectra more complicated.

3.4.2 Transition energies

Having analyzed the LUMO manifold in terms of the number of observed and calculated transitions, we will now turn our attention to the specific transition energies. This permits a more detailed evaluation of the core hole effects and exposes the limitations of the FCH and HCH methods for calculating absorption spectra. Specific attention will be given to the transitions arising from the C1 and C2 atoms because they give rise to the three peak motif that is clearly observed in all spectra. In this way, the multi-electronic effects involved in core hole formation can be examined as a function of molecular size or, rather, as a function of the extent and complexity of the electronic structure.

In naphthalene, the LUMO manifold is composed of transitions resulting from the excitation of only the C1 and C2 atoms. As was previously demonstrated by Hubner *et al.*, the sum of two benzene lineshapes does an excellent job of reproducing the manifold and allows for the precise determination of the chemical

shift and transition intensity ratio for these sites [90]. Some discrepancy is seen between the fit and the measurement, particularly for the two peaks at the high energy side of the manifold. The disagreement can attributed to differences in the vibrational progressions expected for naphthalene and benzene [108]. Taking this into consideration, the error in the extracted transition energy separation was estimated to be ± 0.01 eV and the error in the extracted transition intensity ratio was taken to be ± 0.1. In the larger molecules, the discrepancies between the fit and the measurement become slightly worse because the vibrational modes deviate more from those in benzene. This leads to more uncertainty in the C1 and C2 transition energy separations and ratios. An error of ± 0.02 eV is estimated for the energy separation in anthracene, tetracene and pentacene. For the intensity ratio in these molecules, an error of ± 0.25 is estimated.

The observed separation between the transition energies for the C1 and C2 sites in the polyacenes is attributed to difference in the ionization potentials for the two sites and energy differences in the final states involved in the excitation. Shifts in the binding energies of the $1s$ electrons from the two non-equivalent carbon atoms occur due to their position on the molecule. In the one electron picture, this corresponds to different initial states, $|i\rangle$, and initial state energies involved in the transition in Eq.1.9. Different final states, $|f\rangle$, are involved in the transition because localization of the core hole at either the C1 or C2 results in the electronic structure relaxing differently. Depending on which atom contains the core hole, the rearrangement of the remaining electronic structure proceeds differently and the energy of the LUMO can be different.

The C1 and C2 atoms are chemically very similar (sp^2 bonded to two other carbons and one hydrogen), and, from Tab. 3.5, they are calculated to have very similar ionization potentials in all the polyacenes. Ideally, the ionization potentials could be measured with XPS, but even state of the art core level photoelectron spectroscopy measurements [109] don't have sufficient resolution to separate the individual binding energies[1].

Because the C1 and C2 sites are very so close to being equivalent, it is reasonable to assume that the transition energy separation (see table 3.3) for these sites is almost completely due to a difference in the relaxation of the electronic structure depending on where the core hole is placed. When the excitation occurs at the C2 site, the reorganization of the remaining electronic structure results in a LUMO with lower energy than when the excitation occurs at the C1 site. This observation can be explained phenomologically by the positions of the C1 and C2 atoms: because the C1 atom is at the edge of the molecule, the core hole is not shielded as well as it is in the C2 atom which is in a more central position on the molecule. The concept of differential shielding for the two sites is also supported by the size dependence of the C1 and C2 energy separation. As the molecule size is increased, the measured energy separation between the transitions is observed to decrease. This suggests that the effects of differential screening are greater for the smaller molecules than the larger molecules.

The C1-C2 energy separation trend is modelled well by both the FCH and HCH calculations for naphthalene, anthracene and tetracene. In pentacene, the calculated C1-C2 energy separation increases, contrary

[1]Even if the instrumental resolution were sufficient to resolve the binding energies of the non-equivalent core level electrons, vibrational broadening and final state effects would also affect the XPS measurement

to the measured trend. This discrepancy is more pronounced for the FCH calculation than it is for the HCH calculation. This result indicates that there is some limit to the ability of the one electron picture to model the core hole screening in larger systems. While the FCH approach seems to calculate the trend in LUMO energies adequately for naphthalene, anthracene and tetracene, it is not able to account for the reorganization of the electronic structure in pentacene.

Overall, the measured transition energies have better agreement with the HCH calculation results but the trends in the spectra are more accurately calculated using the FCH method. The HCH method over estimates the transition energies by less than 1 eV while the FCH method over estimates them by around 4 eV. This is unsurprising as the HCH calculations are consistent with the Slater transition state method which approximates the effects of core hole relaxation on the ionization potentials to the second order [110]. But for core to bound state transitions it is necessary to model the effect of the core hole on the unoccupied molecular orbitals, which for the polyacenes is done more adequately using the FCH approximation than the HCH approximation.

3.4.3 Transition intensities

The transition intensities can be evaluated in terms of the ratio of the intensity of the C2 atom transition to the C1 atom transition. This ratio can be accurately determined from the fit of the measured data in all the polyacenes and can be used to further investigate the core hole screening as a function of molecule size.

The measured C2/C1 values are observed to decrease with increasing molecular size as indicated in Figures 3.6 to 3.9. For naphthalene and anthracene, the ratio is greater than 1 and for tetracene and pentacene, the ratio is less than 1. Because the $1s$ orbitals for both sites are very nearly equivalent in all molecules, the observed decrease in the C2/C1 values can be used to probe the structure of the LUMO in the final states. The reorganization of the electronic structure when a core hole is placed at the C1 site results in more LUMO intensity at this position for the larger molecules versus the smaller molecules. At the same time, placing a core hole at the C2 site results in a final state with less LUMO intensity at the C2 position in the larger molecules than it does for the smaller molecules.

Both the FCH and HCH calculations fail to capture the changing C2/C1 intensity ratios for the different polyacenes. The FCH method is able to accurately calculate the intensity ratio for naphthalene and shows better agreement with the measured values than the HCH method. But it incorrectly calculates the decreasing C2/C1 trend with increasing molecule size, showing instead an almost constant C2/C1 ratio for all molecules. Because both methods are inadequate in capturing the proper trend, it is reasonable to assume that multi-electron effects play an increasing role in the electronic structure reconfiguration of the larger molecules. This highlights the inadequacy of the one electron picture for properly determining the LUMO in the larger polyacenes. The proper theoretical treatment of these systems must therefore include multi-electronic effects as is done in the Bethe-Salpeter equation.

3.4.4 Sample stability

The decomposition of tetracene was clearly observed in XAS when several scans were taken at one position on the sample. The observation of isosbestic points in the spectra of both the room temperature and the cooled samples suggests that the decomposition involves the conversion of tetracene to only one other product [111]. From the comparison of the difference spectra in Figures 3.12 and 3.13, it is likely that the damage product is polystyrene or some other similar polymer containing benzene rings. While the damage rate is reduced by cooling, the actual damage process does not appear to be effected by sample temperature.

The dose accumulated in the top 50 nm of tetracene in the process of one scan was estimated to be on the order of 10 MGy. Therefore, the potential for damage occurring on the timescale of a single measurement, and affecting the results of the core hole effect study, existed. But from the calculated accumulated dose as a function of energy, shown in Fig. 3.14, it is clear that most of the dose is applied after measurement of the $1s \rightarrow \pi^*$ region. This suggests that as long as the measurement was not made on a part of the sample that had been previously exposed to the beam, the NEXAFS of the LUMO would only see slight effects due to beam damage. It is, however, quite likely that the higher energy portion of the spectrum contains some contribution from the damage product.

Comparison of the in-situ and ex-situ XAS for these samples show that the sample surface is modified by exposure to atmospheric conditions, but only on the time scale of days. As there is almost no change between the in-situ sample and the sample exposed to air for 2 hours, it is clear that there is no fast chemical modification of the tetracene film. The small differences observed in the XAS of the sample exposed to air for 3 days also showed that there is no dramatic chemical modification occurring on these time scales. Instead, the observations of some slight spectral modification suggest that a very small fraction of the carbon in the sample is being affected by exposure to air.

Evidence for the stability of the tetracene films in air is provided by the observation of the LUMO and LUMO+1 manifolds and the fine structure contained in the LUMO. If the surface layers of the tetracene film decomposed into other forms of carbon or reacted with O_2 to form a quinone, there would be some modification of the LUMO manifold. As described in 2.3.2, the TEY method only probes the top several nanometers of the sample, so the presence of the double manifold and the vibrational features indicates the surface is stable, even after several days exposure to air.

3.5 Conclusions

The polyacenes represent a well studied system of molecules with relevance in several fields of study including heath sciences, the environment, astronomy and physics. Although previous XAS studies of some of these molecules existed, a comprehensive high resolution investigation of the entire series had not been performed. It was found that each molecule exhibited a detailed fine structure that showed several size dependent trends. While there are many different materials that exhibit a fine structure, the spectra of the polyacenes were

unique, primarily due to the persistence of the fine structure in the larger molecules, which is not at all common. As was demonstrated in this chapter, the analysis of the C $1s \rightarrow \pi^*$ (LUMO) transition manifold resulted in a convincing assignment of all features in this portion of the spectra, and the interpretation of these features in terms of core hole effects and sample stability.

The assignment of the LUMO manifold was made possible by fitting each spectra with benzene vibrational lineshapes. This fitting technique, which had already been applied to naphthalene, was successful in simulating all of the fine structure in the spectra. It thereby allowed for the extraction of a) the number of non-equivalent excited atoms involved in the formation of the LUMO manifold in each molecule and b) the extraction of the transition energies and c) the determination of the transition intensities of the purely electronic transitions that made up the LUMO manifold. Calculation results permitted the assignment of each transition to a specific C atom in the molecule which suggested that the core holes were highly localized.

A detailed analysis of the core hole effects in the polyacenes was achieved by considering the energy separation and intensity ratio of the transitions arising from the two end atoms, labelled C1 and C2, which produced a salient three peak structure in all spectra. It was determined that the one electron picture, using the FCH calculation, was adequate for modelling the LUMO energies in the smaller molecules but was not successful for calculation of pentacene. The measured intensity ratios (C2/C1) showed a decreasing trend that was not properly modelled by either the FCH or HCH methods, indicating the need for more elaborate, dynamic screening calculations.

The stability of tetracene was studied under exposure to soft x-ray irradiation and air. It was found that tetracene was chemically modified by the beam, resulting in the formation of a single reaction product with a XAS fingerprint matching that of polystyrene. The comparison between the XAS of in-situ and ex-situ prepared tetracene thin films showed that there was no strong chemical modification of the surface resulting from exposure to air.

While this project explored a number of aspects related to core hole effects, other interesting problems related to multi-electron effects and the calculation of XAS spectra remain to be studied. Recent developments have been made on the calculation of the electron self energy and the application of the Bethe-Salpeter equation for the calculation of XAS [31,112,113]. The ability to extract the C1 and C2 transition energies and intensities from the de-convoluted polyacene spectra with great precision would make the dataset contained in this thesis a valuable test for these new calculation techniques. It would also be interesting to extend the study to the larger, less stable polyacenes, hexacene and heptacene. Future studies involving double excitation of these systems using free electron lasers (FELs) could also improve our understanding of core hole effects.

The application of XRS to the linear PAHs also presents some interesting possibilities for the future when new, high resolution XRS capabilities come online. If XRS measurements at resolutions of 100 meV were possible, new information on the electronic structure of the PAHs under high pressure on during operation in a FET device could be examined.

Applied studies also offer some interesting possibilities. The potential for using XAS for measuring operating devices made from pentacene and tetracene has already explored, but not at high resolution [114]. The high resolution fine structure is extremely sensitive to modification of the LUMO, so the quality of measurements shown in this study could be valuable for in-situ device characterization.

Future opportunities aside, the work in this chapter represents the state of the art application of high resolution XAS. The methods used, in terms of data acquisition and analysis demonstrate how, despite the fact that x-ray absorption spectroscopy had been around for a while, new applications and techniques continue to arise. In the next chapter, a novel technique for measuring bulk sensitive SXAS without self absorption distortions will be discussed.

Chapter 4

The application of partial fluorescence yields in soft x-ray absorption spectroscopy

4.1 Introduction

In Chapter 2, the use of secondary processes, specifically the electron and photon emission from core excited states, for probing the electronic structure of materials was discussed. The use of high resolution TEY measurements for studying the core hole effects and stability of the polyacenes was detailed in the previous chapter. While the TEY worked well for that particular system, electron yield measurements suffer from two principle drawbacks that limit its use. The first is the extreme surface sensitivity, which precludes the use of TEY for bulk measurements and in many in-situ apparatus, and the second is the requirement that the sample be conductive. The use of photon emission or fluorescence yields for probing the linear attenuation coefficient provide results that are inherently bulk sensitive results and not affected by the charge transport properties of the sample. Moreover, the theoretical description of the FLY is much simpler than that of TEY because it does not involve complex in-elastic scattering processes associated with electron emission. The application of FLY is therefore extremely valuable for the study of many systems where bulk sensitivity, in-situ instrumentation or quantitative results are desired.

But total fluorescence yield measurements also suffer from severe limitations. The first is the phenomenon commonly referred to as self absorption, which, as explained in Sec.2.3.3, is more accurately described as the saturation of the fluorescence signal from concentrated samples. This saturation effect has truly hampered the use of fluorescence yields in both hard and soft x-ray studies and has always been viewed as an unavoidable detriment. Strategies for minimizing or correcting for self absorption have been developed but are often not reliable or possible to apply [48, 115, 116].

The second limitation of TFY is the energy dependence in the background of TFY measurements. By the very nature of x-ray absorption, all possible electronic transitions occur upon excitation, leading to a background signal in the TFY from the *non-resonant emission* of the sample. Ideally, this background would be constant, i.e. it would not exhibit any intensity fluctuations as the incident photon energy is scanned through the absorption edge of interest. Unfortunately, this is not the case for most samples, and a distortion due to this non-resonant emission is introduced into the TFY spectrum.

One other limitation of fluorescence yield methods is that the fluorescence efficiency is not constant during resonant excitation. This was first pointed out by de Groot et al., who recognized that the two step model of fluorescence yield, where the excitation and decay of the core hole are viewed as two discrete events, is inadequate for the description of fluorescence yield resulting from resonant excitation [6, 54]. Instead, the fluorescence yield process must be described as a second order coherent x-ray scattering process, more often associated with resonant in-elastic scattering (RIXS). This give rise to distortions in the partial fluorescence yields from core excited atoms that can be described as a change in fluorescence efficiencies as a function of the intermediate state [1].

The problems with fluorescence yield measurements have long been considered to be unavoidable consequences of the measurement method [7]. High concentration samples could not be studied by fluorescence because of the saturation effect. In mixtures where there was a strong fluorescence emission background total fluorescence often appear distorted and was unusable. Finally, accurate comparison between theoretically calculated absorption spectra and fluorescence yield measurements were often not conclusive because the fluorescence yield contained distortions when compared to absorption due to changing fluorescence efficiencies.

Recent developments in detector technology have resulted in solid state x-ray fluorescence detectors (silicon drift detectors) with the ability to efficiently measure fluorescence spectra with energy resolutions better than 100 eV down to B K edge energies (185 eV) [69]. In 2009, one such detector was installed on the SGM beamline at the CLS and has been used to measure x-ray absorption spectra in the partial fluorescence mode, where the intensity of the emission from each element in the sample can be monitored independently. It was determined that saturation effects, the spectral distortions due to non-resonant emission and the effects of changing fluorescence efficiencies at resonance could all be overcome in many samples by the application the IPFY method [50]. PFY methods were also found to much more sensitive than total fluorescence yields in the measurement of dilute systems.

In this chapter, the use of the energy resolved fluorescence yields for electronic structure studies will be explored through the studies at the Fe L-edge. The effects of non-resonant emission will be examined through the use of PFY spectra for aqueous Fe samples. IPFY measurements of three iron oxide minerals will be provided and compared to x-ray Raman (XRS) measurements. The comparison between IPFY and XRS will be used to explore the bulk sensitivity and lack of self absorption in the former. The results of these studies will be used to highlight the important role of energy resolved fluorescence yield techniques in the future of soft x-ray absorption spectroscopy.

[1] In XAS, the final state is usually considered to be the core hole excited state with the core electron placed in an unoccupied valence orbital. But in RIXS, this state is called the intermediate state and the final state refers to the electronic configuration where the core hole has decayed and the originally excited electron remains in the valence band.

4.2 Experiment

4.2.1 Measurement of the partial yields at the Fe L-edge

Partial fluorescence yields were recorded at the Fe L-edge using the SGM beamline at the CLS and the apparatus described in Sec. 2.5.1. Commercial samples of FeO (Wüstite), α-Fe_2O_3 (Hematite) and Fe_3O_4 (Magnetite) were purchased from Sigma Aldrich and used without further purification. The powder samples were attached to the SGM sample holders with double sided carbon tape and loaded into the endstation vacuum chamber for measurement.

For measurement of aqueous $FeCl_3$, a simple liquid cell apparatus was employed. This system uses an HPLC pump to generate a continuous flow of sample through a small cell body that can be placed in the endstation. A 100 nm thick Si_3N_4 window is used to separate the flow path from the chamber vacuum while still allowing the incident and fluorescence x-rays to pass through. Solution of $FeCl_3$ were prepared with concentrations of 500, 200 and 50 mM and maintained at a pH of 1. Careful monitoring of the spectra was used to ensure that reduction of the Fe^{+3} and plating of the window was not occurring.

For each solid sample the TEY and TFY were recorded simultaneously in a single scan along with the PFY and the flux normalization current (I_o). The TEY measurements were made using the drain current method discussed in Sec.2.3.2. For the TFY measurements, the output from a chevron stacked micro-channel plate (MCP) detector, operating with a bias voltage of -1600 V, was used. Measurement of the Fe 2p absorption resonance was made by scanning the incident beam energy from 700 to 730 eV in 0.1 eV steps. The beamline exit slit was set to 20 μm, resulting in an incident photon resolution of approximately 50 meV. Multiple scans, each taking roughly 15 minutes, were made at the same spot on each sample in order to test for sample decomposition. Wide range scans (600 eV to 730 eV) were also performed so that the effect of the changing attenuation coefficient of O, $\mu_O(E_i)$, could be determined for normalization of the IPFY. The liquid cell measurements were made in the same fashion but only the SDD was used.

To extract the IPFY, the O K $_\alpha$ emission was isolated from the excitation-emission matrix (see Sec. 2.5.1). Before extraction, the intensity in the excitation-emission matrix was normalized to the I_o. While the centre of the O K edge is at 525 eV, the O_{PFY} was determined by summing the emission energies from 450 to 500 eV. This was done because there is a weak emission from the $3s$ to $2p$ decay in Fe at 630 eV which can give rise to distortions in the IPFY.

The 600 to 700 eV portion of the wide range scans for each sample were fit to determine the energy dependence in $\mu_O(E_i)$. This energy dependence was then divided out of the O_{PFY} to account for the slight decrease in the O absorption cross section. Finally, the corrected O_{PFY} was inverted to yield the IPFY.

XRS

XRS measurement of the same three iron oxide samples were made using the LERIX 1-b[2] spectrometer on the 20ID beamline at the APS (see Sec. 2.4). A thin layer of the powder sample was placed between kapton tape and loaded into the LERIX sample holder. This was then placed into the spectrometer and the area around the sample was purged with He to reduce the scatter background.

Measurement of the $S(\mathbf{q},\omega)$ for the iron oxides were obtained by the inverse scanning mode. In this mode, the incident beam energy is scanned from 9950 eV to 10 keV while the spectrometer analyzer energies are kept fixed. This allows for the determination of the energy loss in the scattered photons by scanning the beamline monochromator, rather than the 19 individual analyzers on LERIX. The estimated resolution in the energy loss of the analyzers was 1.3 eV. He filled ionization chambers were used to monitor the incident flux.

The XRS spectra were acquired using the sum of all 19 analyzers, covering the $\mathbf{q}$ range from 0.8 to 10.1 Å^{-1}. As discussed in Sec. 1.3.2, XRS can have a $\mathbf{q}$ dependence because higher order transitions (quadrupole and octapole) can occur for high $\mathbf{q}$ scattering. This was not expected or observed for Fe 2p excitation, so the addition of the signal from all 10 analyzers, in order to improve signal quality, was warranted.

The α-Fe_2O_3 and Fe_3O_4 scans were run for approximately 12 hours but the FeO measurement was limited to only 8 hours due to beamline access restrictions. Data processing was performed by normalizing the scattered signal intensities to the incident flux and then subtracting the Thomson scattering background.

4.3 Results

4.3.1 Solid sample PFY

Excitation-emission matrices

The excitation-emission matrices for α-Fe_2O_3, Fe_3O_4 and FeO are shown in Figs. 4.1, 4.2 and 4.3 along with the Fe PFY, the TFY and the O PFY. Each matrix shows the strong emission lines from the O at 525 eV and the Fe L_3 and L_2 emission at 705 and 718 eV. The TFY, and Fe PFY exhibit the expected distortions due to self absorption and the energy dependent background due to the O PFY. In the TFY measurements, a small sub-background dip is observed at the onset of the Fe absorption. These sub-background features are consistent with the O PFY being reduced more at resonance than the Fe PFY is increased. The Fe PFY for all samples is immune to this background effect, but shows a strong saturation due to self absorption.

[2]The 1-b indicates that the spectrometer is the first version but has been upgraded from its original form.

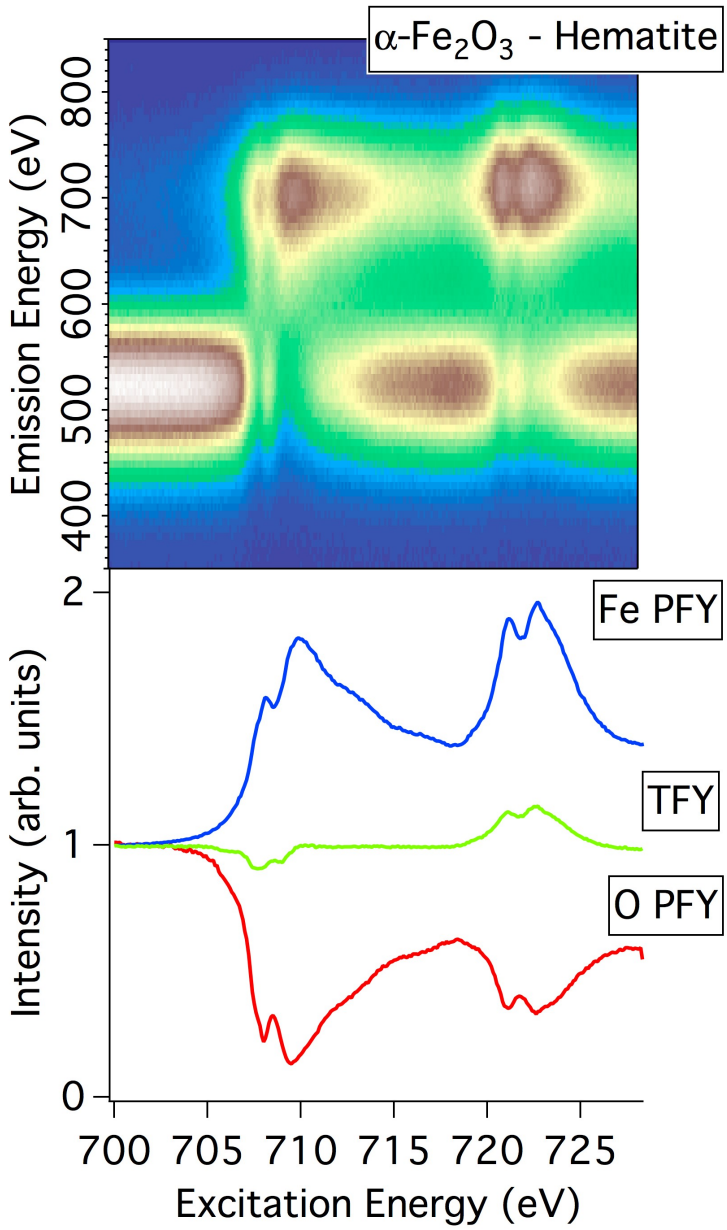

Figure 4.1: The excitation-emission matrix for Fe_2O_3. The Fe PFY was extracted by summing the counts from 425 to 525 eV, the O PFY was extracted by summing the counts from 660 to 760 eV and the TFY is the sum of all counts.

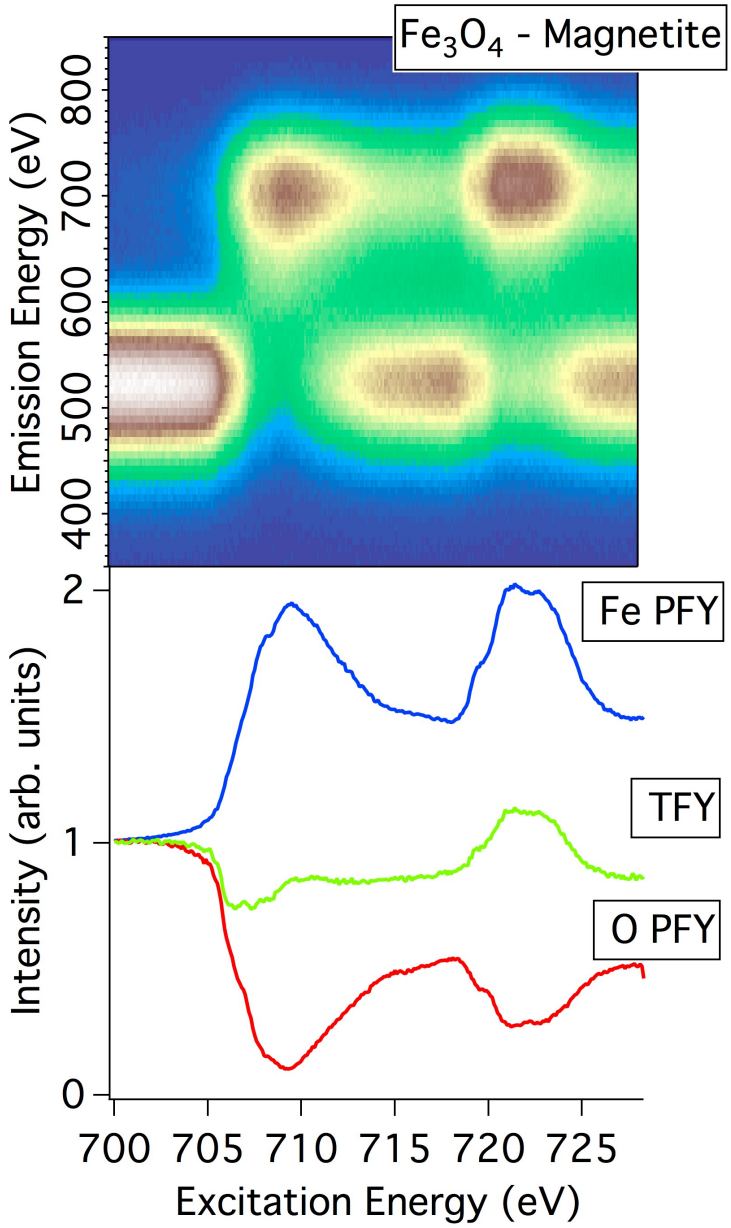

Figure 4.2: The excitation-emission matrix for Fe_3O_4. The Fe PFY was extracted by summing the counts from 425 to 525 eV, the O PFY was extracted by summing the counts from 660 to 760 eV and the TFY is the sum of all counts.

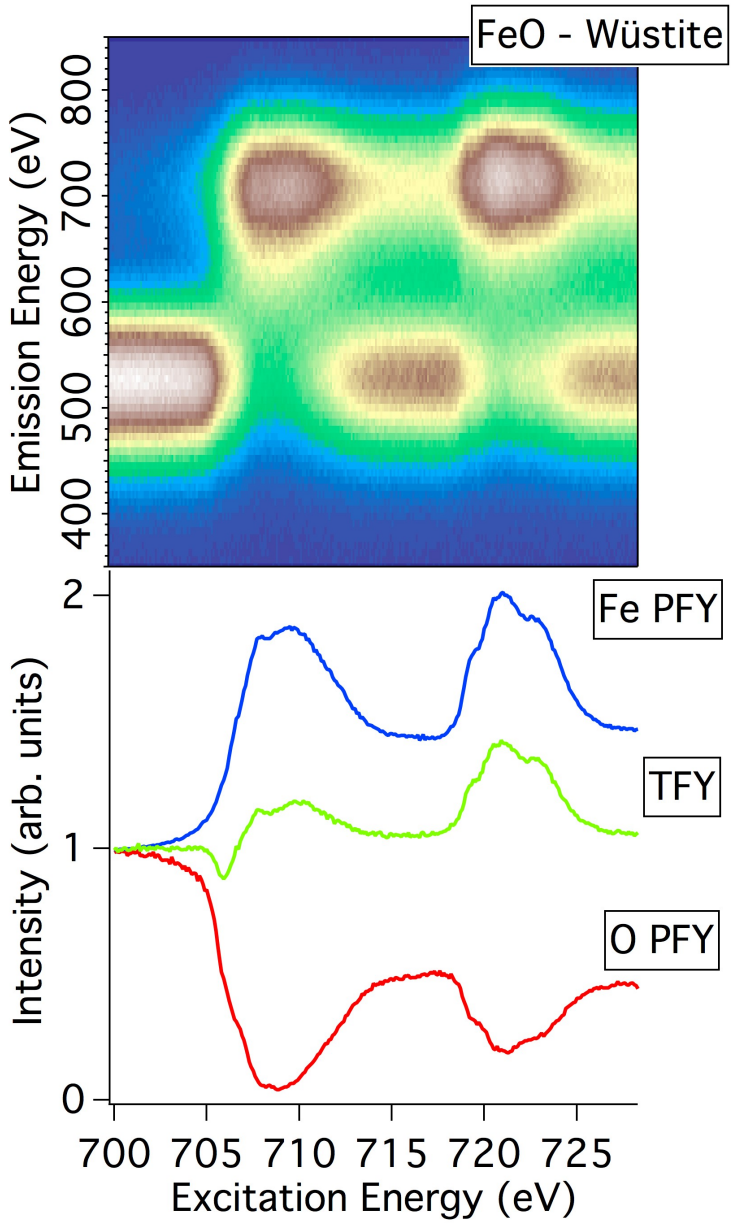

Figure 4.3: The excitation-emission matrix for FeO. The Fe PFY was extracted by summing the counts from 425 to 525 eV, the O PFY was extracted by summing the counts from 660 to 760 eV and the TFY is the sum of all counts.

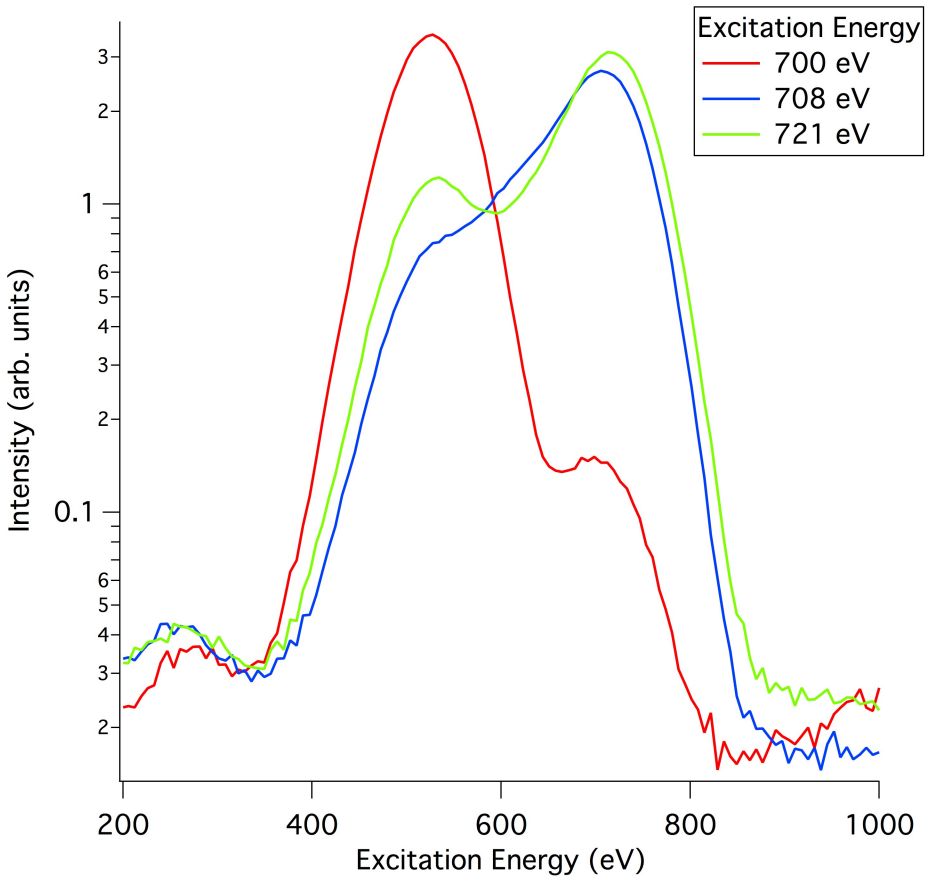

Figure 4.4: X-ray fluorescence spectra for FeO excited at 700 eV, 708 eV and 721 eV.

X-ray fluorescence

To highlight the composition of the x-ray excitation emission matrices, XRF spectra have been extracted from the FeO data set for excitation energies below the L3 resonance, at the L3 resonance and at the L2 resonance. As shown in Fig. 4.4, the XRF spectrum for excitation below the Fe L edge is primarily composed of O K emission with some C and Fe emission. This C emission is attributed to the carbon tape used to mount the powdered sample and the Fe emission is attributed to excitation of the Fe 2p electrons by second order light in the beamline. The XRF spectra show that for excitation at the Fe L3 and L2 edges, the O K emission is weakened and the Fe L emission is enhanced. A clear shift in the Fe emission energies is noted for excitation at the L3 and L2 edges. This shift was measured to be approximately 9 eV and is explained by considering the contribution of both the Fe L_α and L_β emission lines. When the excitation energy is at the L3 edge, only Fe L_α emission at 705 eV occurs. When the excitation energy is tuned to the L2 edge, Fe L_β emission at 718 eV also occurs, resulting in the shift in the measured Fe L emission energy.

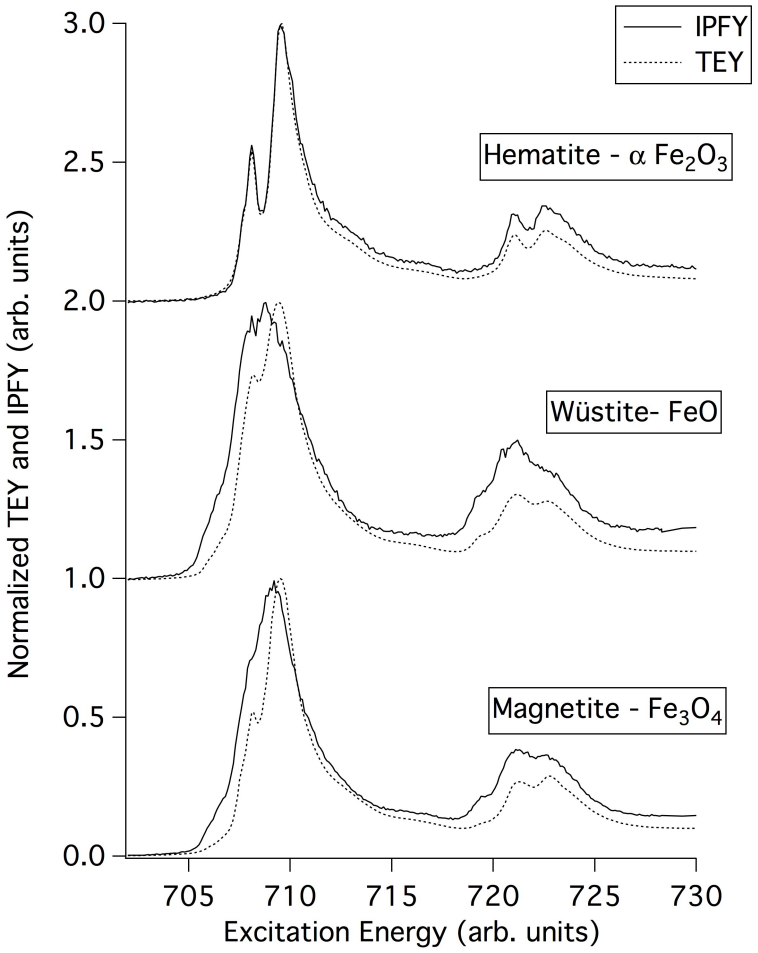

Figure 4.5: The Fe L edge of α-Fe_2O_3, Fe_3O_4 and FeO measured using TEY and IPFY.

IPFY and TEY

In Fig. 4.5 the IPFY and TEY are compared for the three iron oxide minerals. The overall structure of these measurements is consistent with previously published spectra for these samples [117]. Each spectrum is clearly resolved into L3 and L2 components separated by the expected spin orbit splitting of 13 eV.

All of the Fe sites in α-Fe_2O_3 are in octahedral co-ordination and have a valence of 3+. For this sample, there is close agreement between the TEY and IPFY. Both spectra show two well resolved features in the L3 edge that have been attributed to the division of the d orbitals into the t_{2g} and e_g levels as a result of crystal field splitting.

Fe_3O_4 is a mixed valence compound with one third of the Fe being octahedral Fe^{2+}, one third being octahedral Fe^{3+} and the remaining third being tetrahedral Fe^{3+}. The IPFY for Fe_3O_4 shows a broad transition at the L3 edge with two noticeable shoulders. The TEY for this sample shows a weak low energy shoulder at the L3 edge, but contrary to the IPFY, two additional well resolved peaks are observed. In addition, the overall width of the L3 peak is narrower in the TEY measurement than it is in the IPFY

measurement.

In FeO, the iron is formally Fe^{2+} and octahedrally co-ordinated. The IPFY spectrum shows a single broad peak at the L3 edge with a small low energy shoulder. This shoulder, and an additional well resolved peak are both observed in the TEY of the L3 edge.

Saturation effects

Saturation effects were examined by plotting the Fe PFY and the IPFY, as shown in Fig. 4.6. The spectra for each sample were normalized in the pre and post edge to permit a qualitative evaluation of the saturation in each sample. The PFY spectra show the expected behaviour for concentrated samples: the peak heights are suppressed but the features in the L3 or L2 edge retain their peak height ratios.

It is important to note that the L3 peaks are suppressed much more than the L2 peaks. This behaviour is related to the relative attenuation coefficient for the emission from Fe L_α and Fe L_β. The L_α emission at 705 eV does not have sufficient energy to excite the Fe 2p electrons in the sample whereas the L_β emission, at 718 eV, does. Therefore the absorption cross section for the L_α is lower than the absorption cross section for the L_β, resulting in more saturation in the L3 edge than in the L2 edge. This demonstrates another drawback related to the measurement of PFY: the L3 to L2 peak height ratios will always be incorrectly determined using PFY. IPFY, which uses the intensity of the O K_α emission to probe penetrated depth directly, is immune to this problem. This same feature of IPFY and PFY will be highlighted in the following section where the L3 to L2 peak height ratios are incorrectly measured in aqueous $FeCl_3$, even in dilute systems.

4.3.2 Aqueous $FeCl_3$ PFY

The excitation-emission matrix for aqueous 500 mM $FeCl_3$ at pH 1 is shown in Fig. 4.7 along with the extracted O and Fe PFY and the TFY. Due to the relatively low concentration of Fe saturation effects are weak so the Fe PFY more accurately reflects $\mu(E)$ across the Fe L-edge. The O PFY shows the expected trend of decreasing intensity across the edge as the photons that were previously available for excitation of O are now being absorbed by Fe. The TFY shows very little structure compared to the O and Fe PFY as the latter two emissions simply trade off intensity. A small negative feature is noted in the TFY when it is magnified which arises due to the O K_α emission decreasing more than the Fe L_α emission increases when the Fe is resonantly excited.

The PFY and IPFY for 500, 200 and 50 mM concentrations of aqueous $FeCl_3$ are shown in Fig. 4.8. Two interesting trends are noted. The first is that, as discussed above, the L3 to L2 ratio is always slightly greater in IPFY than in PFY due to the difference in the absorption cross section for the L_α and L_β. This highlights that saturation is present in the spectra, even at these low concentrations. The second trend is that the e_g and t_{2g} peak height ratios are different for the PFY and IPFY measurements. IPFY consistently observes a higher t_{2g} to e_g peak height ratio than the PFY.

To evaluate the presence of concentration effects, the spectra of the three different concentrations studied

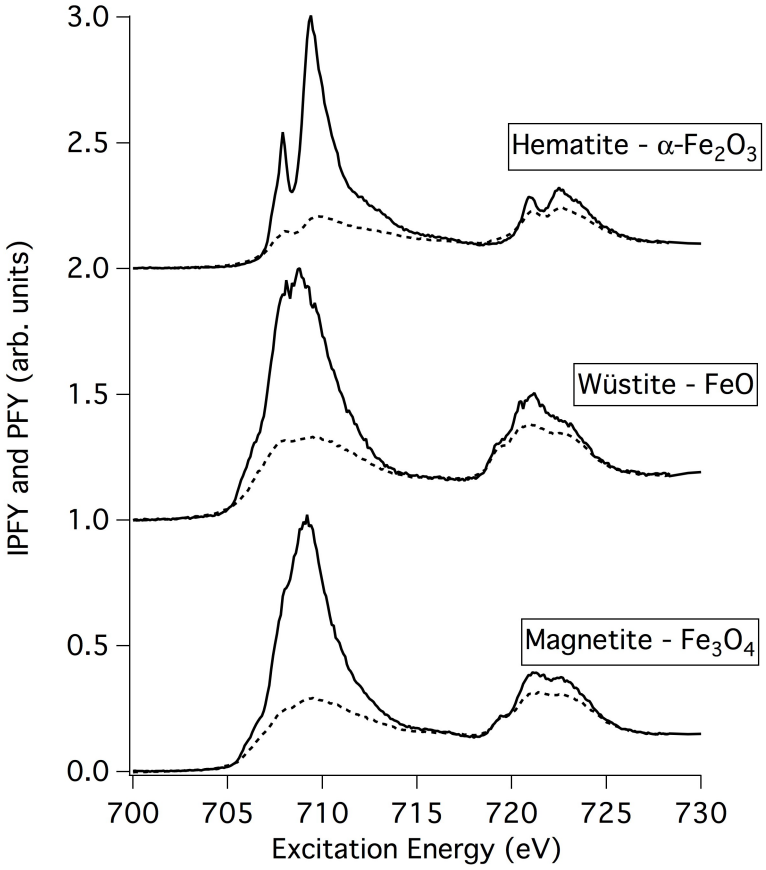

Figure 4.6: The Fe L edge of α-Fe_2O_3, Fe_3O_4 and FeO measured using IPFY (solid line) and Fe PFY (dotted line). The spectra have been scaled and offset in order to permit a qualitative evaluation of saturation effects.

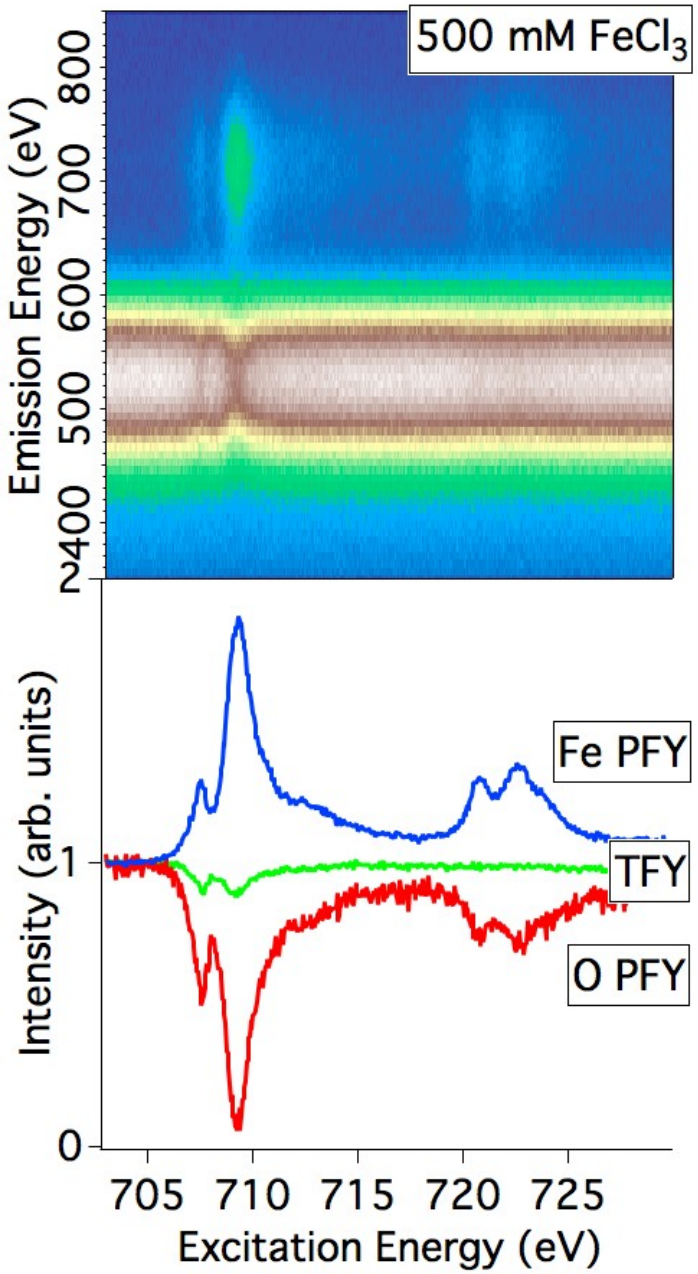

Figure 4.7: The excitation-emission matrix for 500 mM $FeCl_3$. The Fe PFY was extracted by summing the counts from 425 to 525 eV, the O PFY was extracted by summing the counts from 660 to 760 eV and the TFY is the sum of all counts. For clarity, the TFY has been scaled in intensity relative to the Fe and O PFY by a factor of 10.

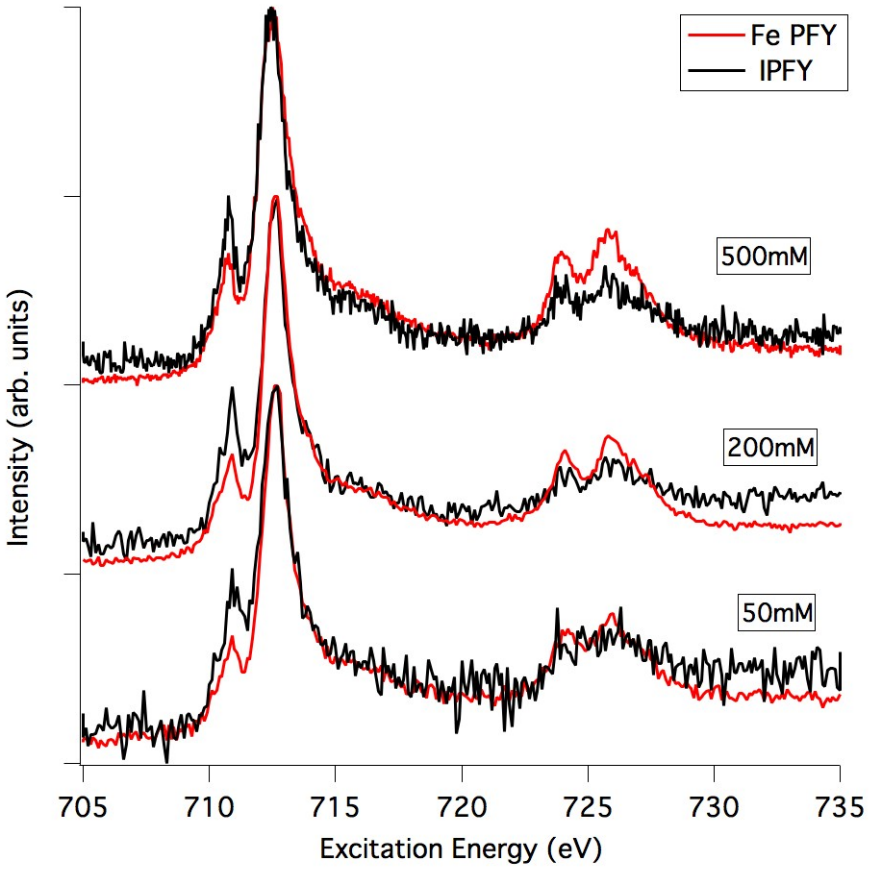

Figure 4.8: The IPFY and PFY of 500, 200 and 50 mM concentrations of aqueous $FeCl_3$.

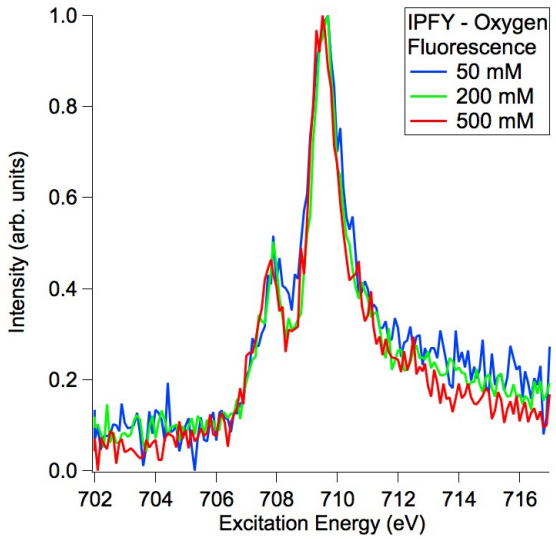

Figure 4.9: The L3 edge IPFY for 500, 200 and 50 mM concentrations of aqueous $FeCl_3$. The spectra have been normalized for comparison.

are plotted together for both the PFY and IPFY in Fig. 4.9 and Fig. 4.10. No noticable differences are noted in the spectra of the three different concentration samples.

4.3.3 Solid sample XRS and IPFY

Finally, the XRS results are shown with the IPFY in Fig. 4.11. The XRS and IPFY data agree well with the primary differences being the signal to noise quality and the spectral resolution. The effect of the decreased spectral resolution is highlighted by the t_{2g} and e_g splitting in the α-Fe_2O_3. While IPFY clearly resolves the two levels into distinct peaks, the XRS shows only a shoulder.

One interesting discrepancy between the IPFY and XRS data is in the width of the L3 peak of FeO. Despite the decrease in resolution, the XRS measures a slightly sharper resonance than IPFY. This observation suggests that one of the two measurements is in error. The most likely cause of the disagreement is a surface versus bulk effect in the IPFY. The IPFY technique assumes a homogeneous distribution in the sample which, as shown by the TEY measurement, is not the case for FeO. The implications for IPFY measurement will be discussed in the following section.

4.4 Discussion

4.4.1 Effects of non-resonant emission

The effects of non-resonant emission on the TFY of the iron oxides are clear when studied with an energy resolving fluorescence yield detector. Use of the SDD for measuring a complete XRF spectra at each excitation energy in an x-ray absorption scan showed that there is a strong energy dependence in the O PFY. When

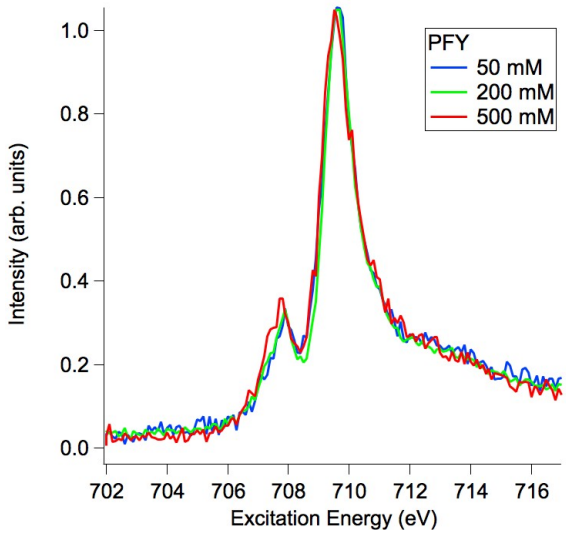

Figure 4.10: The L3 edge PFY for 500, 200 and 50 mM concentrations of aqueous $FeCl_3$. The spectra have been normalized for comparison.

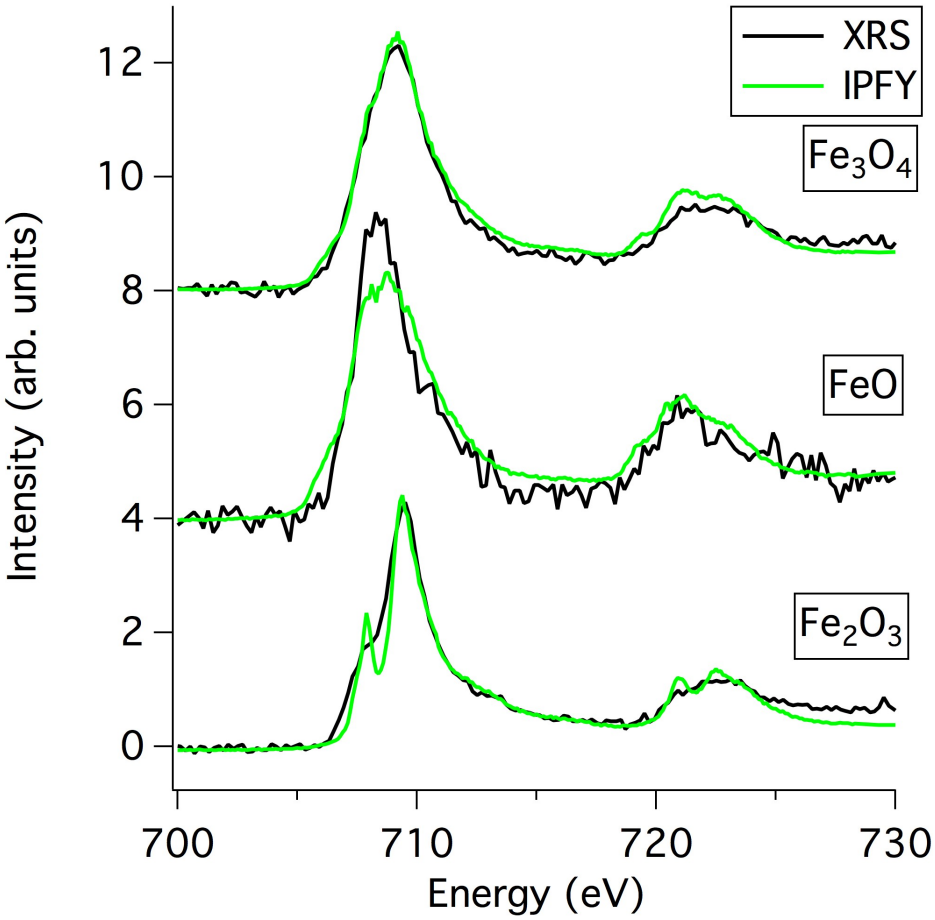

Figure 4.11: The Fe L edge of α-Fe_2O_3, Fe_3O_4 and FeO measured using X-ray Raman and IPFY.

added to the Fe PFY, this energy dependent background introduces distortions to the TFY spectra that include a small sub-background intensity at the Fe $2p$ pre-edge, as shown in Figures 4.1, 4.2 and 4.3. These distortions are also observed in the TFY of the aqueous $FeCl_3$ samples.

The non-resonant emission plays a large role in the formation of the TFY spectra of the iron oxides and aqueous $FeCl_3$ because of the relative attenuation coefficients of O and Fe and their relative fluorescence efficiencies. As the Fe L edge is only separated from the O K edge by 200 eV, the O attenuation coefficient is still considerable for photons that resonantly excite the Fe 2p electrons. This means that there are a considerable number of O atoms that are core excited when the Fe L edge is being probed, giving rise to a stronger non-resonant background than if the Fe compound contained another atom, like C for instance. The relative fluorescence efficiencies of O and Fe are also important in accounting for the strength of the non-resonant emission. Because the fluorescence efficiency of K shell core hole decay is higher than L shell core hole decay [21], the strength of the non-resonant emission from O is enhanced with respect to the resonant emission from Fe.

These factors can be used to interpret the XRF spectra shown in Fig. 4.4. For Fe 2p pre-edge excitation at 700 eV, the non-resonant emission from O is actually stronger than the L3 or L2 resonant emission from Fe. For excitation at the L3 edge, the O emission is still considerable, contributing roughly 1/3 the number of counts to the TFY from the sample.

4.4.2 Saturation

The use of the SDD for PFY and IPFY measurements also allows for a detailed examination of the saturation effects in the iron oxides. The TFY spectra alone do not probe saturation because they incorporate the aforementioned effects of the non-resonant emission background. Fe PFY, extracted from the excitation-emission matrices, must be used so that the true Fe fluorescence signal can be used.

As discussed in Sec. 2.3.3, saturation effects arise due to an energy dependence in both the total attenuation coefficient μ_T and the attenuation coefficient of the atom being probed, in this case μ_{Fe}. When the incident photon energy is scanned through the Fe absorption edge, the energy dependence of μ_{Fe} introduces an increase in the fluorescence from the sample. But at the same time, the energy dependence in μ_T results in a change in the penetration depth of the incident photon beam. As μ_T is the weighted sum of the attenuation coefficients of all of the components of the sample, if μ_{Fe} makes up even a small portion of the sample, the change in the penetration depth will mirror the resulting increase in fluorescence, resulting in a loss of contrast in the measurement.

The measurements shown in Fig. 4.6 highlight that the effects of saturation are clearly different for the Fe L3 and L2 edges. This can be understood by considering the equation for fluorescence yield from a single element in a sample (Eq. 2.4) that was introduced in Sec. 2.3.3. If one considers that the emission from the L3 and L2 edges are separated by 13 eV, the the PFY equation for Fe becomes the sum of the individual

spin orbit components:

$$\mathrm{PFY}_{Fe} = \mathrm{PFY}_{FeL3} + \mathrm{PFY}_{FeL2}. \tag{4.1}$$

Given that the rough emission energies for the components are known to be 705 eV and 718 eV, the PFY relationship becomes

$$\mathrm{PFY}_{Fe} = \left(C \frac{\omega_{FeL3}(E_i, 705eV)\mu_{FeL3}(E_i)}{\mu_{tot}(E_i) + \mu_{tot}(705eV)\frac{\sin\alpha}{\sin\beta}} \right) + \left(C \frac{\omega_{FeL2}(E_i, 718eV)\mu_{FeL2}(E_i)}{\mu_{tot}(E_i) + \mu_{tot}(718eV)\frac{\sin\alpha}{\sin\beta}} \right). \tag{4.2}$$

Recall that the absorption energy of Fe is around 709 eV, which means that μ_{tot} is very different for fluorescence photons at 705 eV and 718 eV. The 705 eV fluorescence from the L_α emission has a much better chance of making it out of the sample than the 718 eV emission from the L_β (For α-Fe_2O_3, the attenuation length is 0.25 μm at 705 eV and 0.08 μm at 718 eV [18]). Because saturation effects occur due to loss of contrast (the absorption happends so near the surface that all fluorescence can escape from the sample), the L3 edge will undergo much more severe saturation than the L2 edge.

4.4.3 IPFY and TEY

The comparison between the IPFY and the TEY, shown in Fig. 4.5, can be used to support the hypothesis of IPFY as a bulk sensitive probe of absorption. As TEY probes only the surface of the sample due to the short mean free path for inelastically scattered electrons, distortions are expected to arise in the TEY due to surface oxidation. But IPFY measurements are composed from the absorption and fluorescence of photons, which should penetrate hundreds of nanometers into the sample. The effects of surface oxidation should contribute to the IPFY spectrum but the contribution is expected to be only a small fraction of the total signal.

α-Fe_2O_3 is well known to be a highly stable form of iron oxide with all of the Fe present as octahedrally co-ordinated Fe^{3+} and no surface modification expected. For both FeO and α-Fe_3O_4, however, contain octahedral Fe^{2+}, which can oxidize at the surface to form octahedral Fe^{3+} [118, 119]. This is reflected in the TEY spectra for these three materials, where the L3 edge in both samples shows resolved splitting into e_g and t_{2g}, indicative of the presence of octahedral Fe^{3+} at the surface.

In contrast to the TEY, the IPFY measurements of FeO and Fe_3O_4 show no resolved e_g and t_{2g} splitting suggesting little or no contribution from octahedrally co-ordinated Fe^{3+}. In addition, the IPFY of FeO and Fe_3O_4 exhibit a low energy shoulder on both the L3 (706 eV) and L2 (718 eV) peaks that is consistent with Fe^{2+} [117]. These observations indicate that the IPFY is not sensitive to small levels of surface modification and are able to probe hundreds of nanometers into the sample.

In all three samples, the TEY spectra exhibit a slightly smaller edge step than the IPFY suggesting an energy dependent background. This would be consistent with the effects a change in $\mu_O(E_i)$, which shows a steady decrease at the Fe L-edge energies. But since the energy dependence in μ_O has been corrected for as described in Sec.2.3.3, more investigation is required to determine if this disagreement is due to a problem with the correction procedure or some other phenomenon.

4.4.4 IPFY and XRS

The agreement between the XRS and IPFY can be used as further verification of the bulk sensitivity of the latter. XRS spectra are measured using 10 keV photons and are therefore representative of the entire thickness of the sample. In contrast, IPFY measurements are made with photon energies of 710 eV, which are only expected to penetrate to a depth of around 100 nm [18]. As discussed in the previous section, the oxidation of Fe^{2+} in FeO and Fe_2O_3 generates a surface layer of octahedral Fe^{3+} on these samples. The agreement between the IPFY and XRS measurements suggests that IPFY is not sensitive to these surface effects and can be viewed as a bulk sensitive probe.

There is one noticeable discrepancy between the two measurement methods that is noted in the L3 peak of FeO, which appears slightly narrower when measured with XRS versus IPFY. Given that the instrumental resolution of IPFY is on the order of 10 times greater than that of XRS, it is not logical that the XRS peak is narrower than that measured by IPFY. While both measurement methods appear to produce the same basic shape, the IPFY measurement seems to exhibit some level of saturation (loss of contrast) in the L3 peak.

A possible explanation of the saturation observed in the IPFY of FeO is the effect of the surface oxidation layer. Since the IPFY spectrum is created by inverting the O PFY, the observation of signal saturation (the peak not going high enough), would be caused by the O K_α emission intensity not getting small enough at the Fe resonance. This could happen if the O to Fe ratio was not homogeneous, but was higher at the surface than in the bulk. It is important to recall that the attenuation length of the soft x-ray beam below the Fe-L edge is roughly 300 nm and only 100 nm above the edge. At the resonance, the penetration depth would be expected to fall to around 10 nm. A higher O to Fe ratio in this 10 nm surface region would inflate the O K_α emission intensity over what would be expected from a homogenous sample. As the O K_α intensity does not dip as low as it would in a homogeneous sample, inverting the spectrum results in a suppression of the peak height.

This saturation effect in IPFY can be modelled by considering 10 nm surface layer of Fe_2O_3 on a thick FeO substrate. The O to Fe ratio at the surface is 1.5, while in the bulk it is 1. In the pre-edge and post-edge regions of the spectrum the O K_α intensity will only see slight distortion due to the surface layer and will remain largely proportional to the linear attenuation coefficient of the FeO. But at the peak of the Fe L-edge the penetration depth drops significantly and the O K_α emission intensity is now more representative of the Fe_2O_3 at the surface. As the O to Fe ratio is 1.5 in the surface region, the O PFY intensity will not drop as low as it would have if the O to Fe ratio was 1. The resulting IPFY spectrum will therefore not increase to the level that it would have in a homogeneous FeO sample and the spectrum will exhibit some peak height saturation that is consistent with the observations in Fig. 4.11. This highlights an important limitation of the IPFY method that should be considered in the application of the technique.

4.4.5 Aqueous measurements

The aqueous measurements at the Fe L-edge are consistent with octahedrally co-ordinated Fe^{3+} and showed no variation for all three of the concentrations measured. The similarity of all of the measurements suggests that no complexation was occurring in the samples, as was expected for the concentrations used given that the pH was maintained at 1.

The discrepancy between the e_g and t_{2g} peak height ratios in the PFY and IPFY could not be linked to any problems with the experiment or data processing. The observation that the IPFY consistently reported a higher t_{2g} to e_g ratio than the PFY was therefore attributed to a difference in the resonant scattering cross section for the two different intermediation states involved. Changes in the resonant scattering cross section could affect the PFY, but because the IPFY is measured using the non-resonant emission from the O in the sample, the IPFY is not complicated by resonant scattering effects.

4.5 Conclusions

Fluorescence yields are an important experimental tool for the measurement of soft x-ray absorption spectra, particularly when bulk sensitivity is required or TEY spectra are unavailable. But the proper use of fluorescence yield for measurement of the linear attenuation coefficient requires careful attention to ensure that spectral distortions arising from an energy dependent emission background and signal saturation do not affect the measurement. This chapter highlighted some of the potential problems that can be faced when using fluorescence yields and showed the value of using partial fluorescence methods as opposed to total fluorescence yields. The application of an energy discriminating fluorescence yield detector to the study of the Fe L-edge in iron oxide minerals and aqueous Fe samples highlighted the advantages of the IPFY method over TEY, TFY and even Fe PFY methods.

TFY detectors are inexpensive and easy to use but because they are often applied incorrectly, without proper consideration of the non-resonant emission from the other elements in the sample, they are not valuable for probing the true linear attenuation coefficients. The mis-interpretation of TFY spectra due to this deficiency was observed in a recent study on the Fe L edge spectra of aqueous $FeCl_3$ solutions. In work published in *Nature Chemistry* in 2010, changes in a sub-background region of the Fe L-edge TFY in different concentrations of aqueous $FeCl_3$, were incorrectly attributed to changes in the relative fluorescence efficiency of Fe and O due to charge transfer [49]. The authors of this work proposed that concentration dependent modifications of the sub-background were evidence of ultra-fast electron transfer from the excited Fe to the surrounding water, resulting in an increase in the fluorescence efficiency of O and, hence, a larger sub-background. While on the surface the trends in their data support this hypothesis, the authors neglected to consider the change in the intensity of the non-resonant background that result from changing the sample concentration. By changing the $FeCl_3$ concentration, the Fe-O ratio is altered, which can also result in a changing sub-background structure [120]. Because the authors of this study did not employ par-

tial fluorescence yields, they were not able to make the distinction between charge transfer and background effects.

The aqueous measurements of three different concentrations of $FeCl_3$ contained in this work also disagree with the work of Aziz and co-workers. Our measurements showed virtually no difference between the the different concentration samples when measured in PFY, suggesting that charge transfer rates are not probed by these methods.

The most significant outcome of the application of energy resolving fluorescence detectors at the soft x-ray energies is the development of the IPFY method. While non-resonant emission can often make TFY measurement unusable, IPFY exploits this signal in order to avoid saturation effects. The IPFY measurements of the Fe L-edge of three iron oxide minerals and aqueous $FeCl_3$ were presented and the ability for IPFY to provide bulk information, free of saturation effects, was verified by comparing the TEY and IPFY spectra for the samples.

A direct comparison between the PFY and IPFY measurements allowed for an interesting examination of self absorption effects that was previously not possible. Differential saturation at the L3 and L2 edges was unambiguously observed and explained due to a difference in the absorption cross section for L_α and L_β emission. This outcome is significant because it shows that partial yield measurements will never properly recover the correct L3 to L2 ratios. In addition, differential saturation due to spin orbit coupling should be expected in the L, M and N edges measured with PFY for all samples, as the cross section for the L_α, M_α and N_α emission is necessarily lower than the cross section for the L_β, M_β and N_β emission.

One interesting possibility that was not fully explored in this work is the potential for using the difference between PFY and IPFY measurements for the determination of elemental concentrations. Because the level of saturation is proportional to the magnitude of the attenuation coefficient of resonantly excited element with respect to the total attenuation coefficient, measuring the degree of saturation (by subtracting PFY from IPFY) provides information on the sample composition. This may be an additional piece of information that can be obtained with no extra effort while performing the absorption spectroscopy of samples.

The comparison of the XRS and IPFY was a valuable test of the bulk sensitivity of IPFY and was also able to highlight a deficiency of the newly developed method. The overall agreement between the XRS and IPFY provided indisputable confirmation that IPFY is bulk sensitive. But a small discrepancy between the two measurement method for FeO suggested that IPFY may be susceptible to a type of saturation effect that arises when the sample composition is not homogeneous. This result highlights the need for more exhaustive testing of the IPFY method. One useful experiment would be the comparison of IPFY measurements for samples with different known thicknesses of thin films.

While this work was able to demonstrate some of the capabilities of energy resolving fluorescence yield detectors for soft x-ray absorption spectroscopy, there are many related areas yet to be explored. Quantification in soft x-ray spectroscopy is one area where the SDD and IPFY may be useful. Additional work by the developers of the IPFY technique is showing that IPFY can be used in the determination of absolute

attenuation coefficients by exploiting its angular dependence [51,121]. Other studies making use of the SDD for novel in-situ measurements of liquids at soft x-ray wavelengths are also underway at the CLS and other synchrotrons, where grating based spectrometers have been utilized for IPFY [122]. A great deal of other work that uses IPFY to study systems previously not accessible using TFY or TEY is also ongoing, including the development of the technique at the intermediate and hard x-ray wavelengths. All of the recent activity involving IPFY suggest that this new measurement method has become part of the standard toolkit for x-ray spectroscopists.

Chapter 5

Conclusions

5.1 Overview

The scientific value of x-ray absorption spectroscopy has been known since the early 20th century. The ability to probe the local electronic structure around specific elements in almost any type of sample has resulted in many significant discoveries of both applied and fundamental significance. But, like all analytical methods, there are limitations related to the measurement and the interpretation of absorption spectra that have restricted its applicability. This is particularly true at the soft x-ray wavelengths where large absorption cross sections make accurate measurements difficult and the reliance on theoretical calculation of near edge structure is important. It is has been the focus of this thesis to investigate some of the problems faced in the accurate measurement and modelling of soft x-ray absorption spectra and to demonstrate recent improvements in these areas.

Chapter 1 presented a review of the standard practise involved in the measurement and simulation of XAS was presented along with a fundamental overview of the measurement methods and basic simulation techniques. Of key importance in this chapter was the description of the relationship between the attenuation length of a photon in a material and the electronic structure of that material (Eqs. 1.9 and 1.11). These relationships show how electronic structure information is encoded into the energy dependence of the penetration depth of the photons into the material - the absorption spectrum.

The ability to decode the electronic structure information from the absorption spectrum is highly reliant on the accuracy of the measurement. The basic problem comes down to how to correctly measure x-ray penetration depths on the order of tens or hundreds of nanometers. As discussed in sections 2.3.4 to 2.3.3, there are many complications with the available methods for measuring penetrations depth. Transmission measurements are often not compatible with the sample system and secondary methods like TEY and TFY have problems related to charging, surface sensitivity and saturation. Overcoming the limitations to the measurement is crucial because artifacts related to the measurement method most often prohibit meaningful interpretation.

One of the main roadblocks in the interpretation of soft x-ray absorption spectroscopy is the lack of theoretical models that can properly treat the core hole excited state. In the past decades there have been great advances in hard x-ray absorption spectroscopy because the multiple scattering theory can be used to

reliably model the extended absorption portion of the spectrum. But soft x-ray absorption (and hard x-ray near edge) spectroscopy lack the same type of reliable and accessible calculation tool. While the near edge spectra are rich in information on the electronic structure, much of it is inaccessible because the theoretical models for how to treat multi-electronic effects are not available.

The ongoing development of soft x-ray absorption spectroscopy is therefore reliant on overcoming two separate, but equally important, challenges: 1) the measurement of the true x-ray absorption cross section, free from artifacts and distortion, and 2) moving beyond the one electron picture in the calculation of x-ray absorption structure. While these are formidable problems, tackling them will result in many benefits in many fields of science. This thesis only begins to addresses these two issues, first by investigating new measurement methods and then by examining the high resolution absorption spectra of a model series of molecules to examine the limitations of the one electron picture.

5.2 Instrumentation development

Chapter 2 discussed details related to the instrumentation involved in the various x-ray based measurement techniques that probe the electronic structure in low Z elements. Theoretical development of the electron and fluorescence intensities was provided along with a description of the instrumentation used in XRS measurements. New developments in solid state fluorescence yield detectors with energy resolving capability was discussed and examples of how these detectors can be used for the measurement of partial fluorescence yields were provided. Development of the IPFY method was also described to show that saturation effects can be overcome in concentrated samples by monitoring the non-resonant emission intensity.

The importance of the IPFY method for accurate determination of the bulk electronic structure cannot be overstated. Quantification in soft x-ray absorption spectroscopy has been elusive because of the problems associated with the standard total yield methods. IPFY provides new opportunities for quantitative analysis due to its interesting geometry dependence as was discussed in Sec. 2.3.3. Further development of SDD instrumentation promises to improve the ability to perform quantitative soft x-ray absorption measurements.

In Ref. [51], Achkar and collaborators explored the IPFY geometry dependence by collecting IPFY spectra for various different sample orientations. These experiments involved rotation of the sample with respect to both the beam and the detector, thus changing the relative path length of the incident and fluorescence x-rays. While this method, which uses a single SDD, can work, the inclusion of additional detector elements in a well defined geometry can greatly simplify the quantitative measurements. A prototype SDD array, shown in Fig. 5.1, has been developed for this purpose.

The prototype detector employs four identical SDDs arranged in a linear fashion so that each detector observes a different geometry with respect to the sample. As shown in Fig. 5.2, the detector closest to the incident beam (detector 4) measures fluorescence that has to pass through much less sample material than the detector positioned at a more glancing angle (detector 1). From the IPFY relationship in Eq. 2.10,

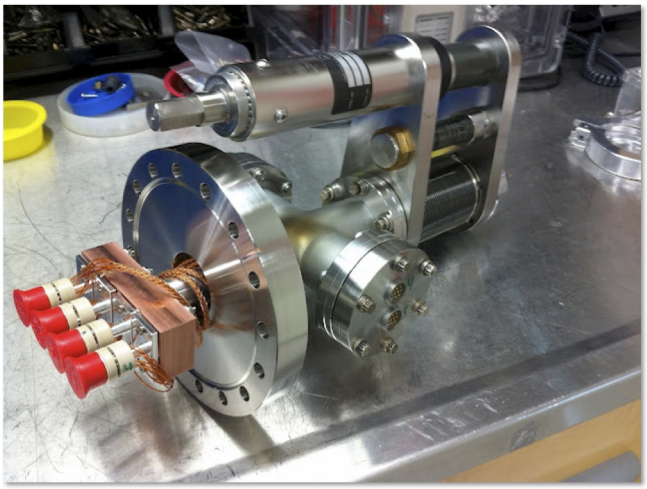

Figure 5.1: A prototype SDD array for quantitative soft x-ray absorption.

the expected response of each detector will be a simple offset from the others due to the $sin\beta$ term in the numerator. Because the detector geometry is known, the difference in the IPFY from each detector can be used to determine and remove the offsets. The result is a quantitative probe of the absolute magnitude of the change in the linear attenuation coefficient of the incident photon beam. This can be normalized to tabulated values in the non-resonant pre or post-edge region to produce quantitative absorption spectra.

While quantitative measurements using IPFY are a reality, many challenges remain to be overcome before they become common place. One of the primary difficulties with these types of measurements is that they require homogeneous samples that are smooth on the order of the penetration depth of the x-rays. Any surface roughness will distort the measurements and introduce error into the measurements. Other complications can arise from nonlinear detector response.

The measurement of quantitative absorption spectra presents many new opportunities for comparison between theoretical and experimental results. In particular, the absolute magnitude of calculated transition moments can be compared to measurement. Quantitative spectra can also be reliably transformed to scattering intensities using the Kramers-Kronig relationship and compared to resonant scattering measurements [123].

One of the other options that exists for improving the quantitative measurement of the absorption spectrum of low Z elements is to push the development of XRS. XRS has no problems with surface sensitivity or saturation and they can be used in combination with a wide variety of in-situ apparatus. While there are currently no XRS beamlines in the world that can match the spectral quality and resolution of a soft x-ray absorption beamline, there are no technical restrictions that prohibit their development. Increasing the resolution of XRS instruments will require more brilliant light sources, better monochromators, larger spectrometers and better detectors. There is little doubt that all of these requirements will be eventually met.

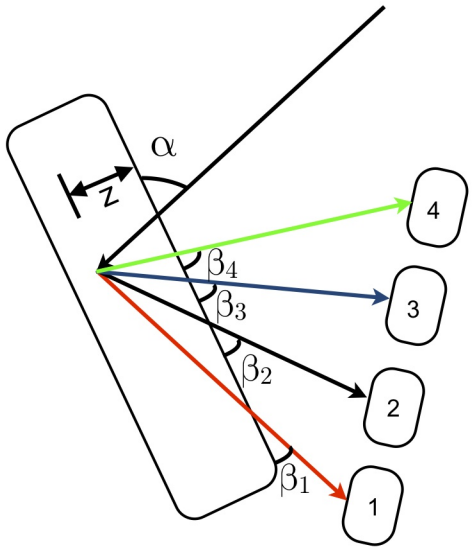

Figure 5.2: A sketch of the geometry in an absorption measurement employing a linear SDD array. Fluorescence photons reaching each detector have to traverse a different amount of sample. The difference

5.3 Core hole effects in the polyacenes

If accurate absorption spectra can be measured, a careful comparison to simulated absorption spectra, calculated from ab-inito electronic structure codes, can be used to determine structure. But, as discussed in Sec. 1.4, the calculation of excited state electronic structure is made difficult due to the many body physics involved. An overview of the application of DFT to the calculation of soft x-ray absorption spectra was provided in Sec. 1.4, with emphasis on the the approximations needed in the formation of the exchange-correlation term. While these approximations (LDA or GGA) are sufficient for most ground state calculations, they do not incorporate the strong multi-electronic effects that occur during core excitation.

Exploration of the limits of the one electron picture in the modelling of the XAS of the polyacenes was the main focus of Chapter 3. The high resolution structure in the XAS of the polyacenes contained sufficient detail to allow for the transition energies and intensities for the $1s \rightarrow \pi^*$ transitions from the non-equivalent carbon sites for each molecule in the series. Comparison between the extracted energies and intensities with values calculated from DFT shows the limitations of the calculation.

Moving beyond the one electron picture in modelling core level excitation involves the application of TD-DFT or BSE levels of theory. Currently, the BSE has been implemented in XAS calculations in a code package called OCEAN [124]. This package seems to show the most promise for improving XAS modelling as it accounts for the screened electron-hole interaction by solving the BSE.

Future work will involve comparison between the high resolution XAS of the polyacenes and spectra calculated using the OCEAN code. Of key importance will be an evaluation of how well the BSE calculation can model the energy difference and intensity ratio of the C1 and C2 excitations as the molecules become

larger. As was discussed in Sec. 3.4.3, the final state model of core hole screening using the HCH and FCH approximations failed to recover the proper C2/C1 intensity ratios for the large molecules. Modelling of this intensity ratio for the PAH series would be a useful test of the BSE level of theory for modelling core hole effects.

5.4 Stability of the polyacenes

Chapter 3 also discussed the decomposition of the polyacenes under irradiation and the stability of the sample surface after exposure to air. A novel method of estimating the dose to the sample as the scan progressed suggested that the bulk of the beam damage that occurred to the surface of tetracene only occurred after measurement of the $1s \rightarrow \pi^*$ portion of the spectrum. In-situ measurements were compared to those taken of samples exposed to air and it was determined that there is little chemical modification of the surface layers of the thin film samples.

The main reason that these results are presented as part of this thesis is to demonstrate the importance of understanding the potential for beam damage on samples. It is often incorrectly assumed that because soft x-rays are low in energy, they do not do as much damage to samples as hard x-rays. But because soft x-ray absorption cross sections are so large, all of their energy is dumped into a very small sample volume, leading to a very high dose. Furthermore, because the Auger emission channel is the highly favoured decay channel for low Z elements, soft x-ray absorption results in a much higher number of ionizing electrons being released inside the sample. This ionizing radiation has a much better chance of dumping its energy in the sample through in-elastic scattering of electrons than a fluorescence photon, which can often escape the sample.

Beam damage will always be an issue for soft x-ray measurements and should always be tested for. Measurements should always be performed on new spots on the sample to minimize dose and beamline efficiency has to be optimized. As described in Sec. 2.5.2, continuous scanning methods can be used to increase the duty cycle of the measurement. In recent years, the fast scanning mode on the SGM beamline has become the standard method for measuring organic systems. Through careful testing and optimization, beam damage effects can effectively be avoided.

5.5 Partial fluorescence yields

The development of partial fluorescence yield capabilities and the IPFY method have been essential for the proper evaluation of the Fe L-edge in iron oxides and aqueous Fe samples. The use of the SDD allows for the acquisition of the excitation-emission maps, which can be post-processed to extract both the resonant and the non-resonant emission from the sample. This method of data aquisition has been performed on many other sample at the SGM beamline and has resulted in a much better understanding of the close relationship between x-ray absorption and x-ray emission.

The Fe L-edge work demonstrates that PFY and IPFY measurements demonstrate a basic conservation between the number of photons incident on the sample and the number of fluorescence photons coming from the sample. When the Fe in the sample is being excited at resonance, photons that were previously available for the excitation of O 1s electrons are now being used in the excitation of Fe 2p electrons. Hence there is a decrease in the number of O core holes that are able to generate fluorescence.

The same concept can be explained by considering the pentration depth of the incident photon beam. Below the Fe L-edge, the linear attenuation coefficient is small and the photons penetrate relatively deep into the sample. The bulk of the absorption is done by the O in the sample, which generates a large O K_α emission background. At the Fe 2p resonance energy, the penetration depth drops because the Fe becomes the dominant absorber. Because the O 2p absorption cross section does not have any large features at the Fe 2p excitation energies, the O K_α emission intensity is *directly proportional to the penetration depth of the x-ray beam*! Inversion of the O K_α intensity will produce the IPFY which is directly proportional to the x-ray linear attenuation coefficient.

Perhaps the most interesting feature of the IPFY is one of its more subtle characteristics: because the IPFY is produced by monitoring *non-resonant* emission from the sample, it is not affected by changes in the *resonant* scattering cross section. As was pointed out by de Groot in 1994 [54], the two step model of fluorescence yield, where excitation and fluorescence can be considered two distinct processes, is not valid for excitation at resonance. Instead, fluorescence at resonance must be modelled as a second order coherent scattering process where the scattering cross section (analogous to the fluorescence efficiency in the two step model) is highly dependent on the intermediate states involved. This means that the intensity of the PFY from a sample, even if it is dilute and not suffering from saturation effects, may not be proportional to the linear attenuation coefficient. IPFY, on the other hand, is not affected by resonant excitation and will not suffer such distortions.

Finally, the comparison between XRS and IPFY is an interesting example of the use of complimentary techniques. Experimentally, x-ray absorption and x-ray Raman are two very different techniques but they can be used to probe exactly the same properties of the sample. While XRS still has a long way to come before it can measure with sufficient energy resolution for detailed studies, it is still a valuable tool for studies where bulk sensitivity is required or in-situ apparatus are not compatible with soft x-ray beamlines.

References

[1] Jin Suntivich, Hubert A. Gasteiger, Naoaki Yabuuchi, Haruyuki Nakanishi, John B. Goodenough, and Yang Shao-Horn. Design principles for oxygen-reduction activity on perovskite oxide catalysts for fuel cells and metal–air batteries. *Nat Chem*, 3(7):546–550, 07 2011.

[2] J. Zaanen, G. A. Sawatzky, and J. W. Allen. Band gaps and electronic structure of transition-metal compounds. *Phys. Rev. Lett.*, 55:418–421, Jul 1985.

[3] Seung-Hoon Jhi, Steven G. Louie, and Marvin L. Cohen. Electronic properties of oxidized carbon nanotubes. *Phys. Rev. Lett.*, 85:1710–1713, Aug 2000.

[4] National Research Council (U.S.). Committee on Bioavailability of Contaminants in Soils and Sediments. *Bioavailability of contaminants in soils and sediments: processes, tools, and applications*. National Academies Press, 2003.

[5] G. van der Laan, B. T. Thole, G. A. Sawatzky, and M. Verdaguer. Multiplet structure in the L_2, *3* x-ray-absorption spectra: A fingerprint for high- and low-spin ni^{2+} compounds. *Phys. Rev. B*, 37:6587–6589, Apr 1988.

[6] F. Groot and A. Kotani. *Core level spectroscopy of solids*. Advances in condensed matter science. CRC Press, 2008.

[7] Joachim Stöhr. *NEXAFS Spectroscopy*. Springer, Berlin, 1992.

[8] Winfried Schlke. *Electron Dynamics by Inelastic X-Ray Scattering*. Oxford Series on Synchrotron Radiation. Oxford Univ. Press, Oxford, 2007.

[9] Johannes Lehmann and Dawit Solomon. Chapter 10 - organic carbon chemistry in soils observed by synchrotron-based spectroscopy. In Balwant Singh and Markus Grfe, editors, *Synchrotron-Based Techniques in Soils and Sediments*, volume 34 of *Developments in Soil Science*, pages 289 – 312. Elsevier, 2010.

[10] A. Tersigni, J. Shi, D. T. Jiang, and X. R. Qin. Structure of tetracene films on hydrogen-passivated si(001) studied via stm, afm, and nexafs. *Physical Review B (Condensed Matter and Materials Physics)*, 74(20):205326, 2006.

[11] Michael Pravica, Ognjen Grubor-Urosevic, Michael Hu, Paul Chow, Brian Yulga, and Peter Liermann. X-ray raman spectroscopic study of benzene at high pressure. *The Journal of Physical Chemistry B*, 111(40):11635–11637, 2007.

[12] Won-Sub Yoon, Kwang-Bum Kim, Min-Gyu Kim, Min-Kyu Lee, Hyun-Joon Shin, Jay-Min Lee, Jae-Sung Lee, and Chul-Hyun Yo. Oxygen contribution on li-ion intercalationdeintercalation in licoo2 investigated by o k-edge and co l-edge x-ray absorption spectroscopy. *The Journal of Physical Chemistry B*, 106(10):2526–2532, 2002.

[13] J.G Chen, J Eng Jr., and S.P Kelty. Nexafs determination of electronic and catalytic properties of transition metal carbides and nitrides: From single crystal surfaces to powder catalysts. *Catalysis Today*, 43(12):147 – 158, 1998.

[14] Cole F. Petersburg, Robert C. Daniel, Cherno Jaye, Daniel A. Fischer, and Faisal M. Alamgir. Soft X-ray characterization technique for Li batteries under operating conditions. *Journal of Synchrotron Radiation*, 16(5):610–615, Sep 2009.

[15] William Crookes. The bakerian lecture: On the illumination of lines of molecular pressure, and the trajectory of molecules. *Philosophical Transactions of the Royal Society of London*, 170:135–164, 1879.

[16] W. Kossel. Zum bau der rntgenspektren. *Zeitschrift fr Physik A Hadrons and Nuclei*, 1:119–134, 1920. 10.1007/BF01881031.

[17] P. A. M. Dirac. The quantum theory of the emission and absorption of radiation. *Proceedings of the Royal Society of London. Series A, Containing Papers of a Mathematical and Physical Character*, 114(767):pp. 243–265, 1927.

[18] B.L. Henke, E.M. Gullikson, and J.C. Davis. X-ray interactions: photoabsorption, scattering, transmission, and reflection at e=50-30000 ev, z=1-92. *Atomic Data and Nuclear Data Tables*, 54(2):181–342, July 1993.

[19] BK Teo. SLAC Research Library — Community Pages, 1986.

[20] J. Stöhr, L. Johansson, I. Lindau, and P. Pianetta. Extended-x-ray-absorption-fine-structure studies of low-z atoms in solids and on surfaces: Studies of si_3n_4, sio_2, and oxygen on si(111). *Phys. Rev. B*, 20:664–680, Jul 1979.

[21] M.O. Krause and J.H. Oliver. Natural widths of atomic k and l levels, k x-ray lines and several kll auger lines. *J. Phys. Chem Ref. Data 8*, page 329, 1979.

[22] H. Wadati, D. G. Hawthorn, T. Z. Regier, G. Chen, T. Hitosugi, T. Mizokawa, A. Tanaka, and G. A. Sawatzky. Valence evaluation of limno[sub 2] and related battery materials by x-ray absorption spectroscopy. *Applied Physics Letters*, 97(2):022106, 2010.

[23] C V RAMAN and K S KRISHNAN. A New Type of Secondary Radiation. *Nature*, 121(3048):501–502, mar 1928.

[24] Adolf Smekal. Zur Quantentheorie der Dispersion. *Die Naturwissenschaften*, 11(43):873–875, oct 1923.

[25] K Gupta. Smekal-Raman Type Modified X-Ray Scattering. *Physical Review Letters*, 3(1):38–40, jul 1959.

[26] Yukio Mizuno and Yoshihiro Ohmura. Theory of x-ray raman scattering. *Journal of the Physical Society of Japan*, 22(2):445–449, 1967.

[27] H. Kramers and W. Heisenberg. ber die streuung von strahlung durch atome. *Zeitschrift fr Physik A Hadrons and Nuclei*, 31:681–708, 1925. 10.1007/BF02980624.

[28] Donald Allen McQuarrie. *Statistical Mechanics*. University Science Books, Sausalito, California, USA, second edition edition, 2000.

[29] P. Hohenberg and W. Kohn. Inhomogeneous Electron Gas. *Physical Review*, 136:864–871, November 1964.

[30] J. Stöhr and R. Jaeger. Absorption-edge resonances, core-hole screening, and orientation of chemisorbed molecules: Co, no, and n_2 on ni(100). *Phys. Rev. B*, 26:4111–4131, Oct 1982.

[31] Eric L. Shirley. Bethe-salpeter treatment of x-ray absorption including core-hole multiplet effects. *Journal of Electron Spectroscopy and Related Phenomena*, 144-147:1187 – 1190, 2005. Proceeding of the Fourteenth International Conference on Vacuum Ultraviolet Radiation Physics.

[32] P. M. Th. M. van Attekum and G. K. Wertheim. Excitonic effects in core-hole screening. *Phys. Rev. Lett.*, 43:1896–1898, Dec 1979.

[33] G. Margaritondo. *Introduction to synchrotron radiation*. Oxford University Press, 1988.

[34] H. Wiedemann. *Synchrotron radiation*. Advanced texts in physics. Springer, 2003.

[35] H. Winick. *Synchrotron Radiation Sources: A Primer*. Series on synchrotron radiation techniques and applications. World Scientific, 1995.

[36] Proceedings of the Joint Accelerator Conferences. Geneva, 2004. JACoW.

[37] C T Chen and F Sette. High Resolution Soft X-Ray Spectroscopies with the Dragon Beamline. *Physica Scripta*, 1990:119–126, jan 1990.

[38] J.H Underwood and E.M Gullikson. High-resolution, high-flux, user friendly vls beamline at the als for the 50-1300 ev energy region. *Journal of Electron Spectroscopy and Related Phenomena*, 92(1-3):265 – 272, 1998.

[39] H. Ohashi, E. Ishiguro, Y. Tamenori, H. Okumura, A. Hiraya, H. Yoshida, Y. Senba, K. Okada, N. Saito, I.H. Suzuki, K. Ueda, T. Ibuki, S. Nagaoka, I. Koyano, and T. Ishikawa. Monochromator for a soft x-ray photochemistry beamline bl27su of spring-8. *Nuclear Instruments and Methods in Physics Research Section A: Accelerators, Spectrometers, Detectors and Associated Equipment*, 467-468(Part 1):533 – 536, 2001. 7th Int.Conf. on Synchrotron Radiation Instrumentation.

[40] T. Regier, J. Paulsen, G. Wright, I. Coulthard, K. Tan, T. K. Sham, and R. I. R. Blyth. Commissioning of the spherical grating monochromator soft x-ray spectroscopy beamline at the canadian light source. *AIP Conference Proceedings*, 879(1):473–476, 2007.

[41] T. Regier, J. Krochak, T.K. Sham, Y.F. Hu, J. Thompson, and R.I.R. Blyth. Performance and capabilities of the canadian dragon: The sgm beamline at the canadian light source. *Nuclear Instruments and Methods in Physics Research Section A: Accelerators, Spectrometers, Detectors and Associated Equipment*, 582(1):93 – 95, 2007. Proceedings of the 14th National Conference on Synchrotron Radiation Research - SRI 2007.

[42] Steve Heald, Edward Stern, Dale Brewe, Robert Gordon, Daryl Crozier, Detong Jiang, and Julie Cross. XAFS at the Pacific Northwest Consortium-Collaborative Access Team undulator beamline. *Journal of Synchrotron Radiation*, 8(2):342–344, Mar 2001.

[43] S. M. Heald, D. L. Brewe, E. A. Stern, K. H. Kim, F. C. Brown, D. T. Jiang, E. D. Crozier, and R. A. Gordon. XAFS and micro-XAFS at the PNC-CAT beamlines. *Journal of Synchrotron Radiation*, 6(3):347–349, May 1999.

[44] K.V. Kaznatcheev, Ch. Karunakaran, U.D. Lanke, S.G. Urquhart, M. Obst, and A.P. Hitchcock. Soft x-ray spectromicroscopy beamline at the cls: Commissioning results. *Nuclear Instruments and Methods in Physics Research Section A: Accelerators, Spectrometers, Detectors and Associated Equipment*, 582(1):96 – 99, 2007. Proceedings of the 14th National Conference on Synchrotron Radiation Research - SRI 2007.

[45] Janos Kirz and Chris Jacobsen. Soft x-ray microscopes and their biological applications list of figures. *Quarterly Reviews of Biophysics*, 1995.

[46] H Ade, X Zhang, S Cameron, C Costello, J Kirz, and S Williams. Chemical contrast in x-ray microscopy and spatially resolved xanes spectroscopy of organic specimens. *Science*, 258(5084):972–975, 1992.

[47] S. Hüfner. *Photoelectron spectroscopy: principles and applications*. Springer series in solid-state sciences. Springer, 2003.

[48] S. Eisebitt, T. Böske, J.-E. Rubensson, and W. Eberhardt. Determination of absorption coefficients for concentrated samples by fluorescence detection. *Phys. Rev. B*, 47(21):14103–14109, Jun 1993.

[49] Emad F Aziz, M Hannelore Rittmann-Frank, Kathrin M Lange, Sébastien Bonhommeau, and Majed Chergui. Charge transfer to solvent identified using dark channel fluorescence-yield L-edge spectroscopy. *Nature Chemistry*, 2(10):853–857, aug 2010. 10.1038/nchem.768.

[50] A. J. Achkar, T. Z. Regier, H. Wadati, Y.-J. Kim, H. Zhang, and D. G. Hawthorn. Bulk sensitive x-ray absorption spectroscopy free of self-absorption effects. *Phys. Rev. B*, 83(8):081106, Feb 2011.

[51] A. J. Achkar, T. Z. Regier, E. J. Monkman, K. M. Shen, and D. G. Hawthorn. Determination of total x-ray absorption coefficient using non-resonant x-ray emission. *Scientific Reports*, 1, December 2011.

[52] P.D. Hatton, S.B. Wilkins, T.A.W. Beale, T.K. Johal, D. Prabhakaran, and A.T. Boothroyd. Resonant soft x-ray scattering a new probe of charge, spin and orbital ordering in the manganites. *Journal of Magnetism and Magnetic Materials*, 290291, Part 2(0):891 – 897, 2005.

[53] P. Abbamonte, L. Venema, A. Rusydi, G. A. Sawatzky, G. Logvenov, and I. Bozovic. A structural probe of the doped holes in cuprate superconductors. *Science*, 297(5581):581–584, 2002.

[54] F.M.F. de Groot, M.A. Arrio, Ph. Sainctavit, Ch. Cartier, and C.T. Chen. Fluorescence yield detection: Why it does not measure the x-ray absorption cross section. *Solid State Communications*, 92(12):991 – 995, 1994.

[55] Derek Peak and Tom Z Regier. Direct observation of tetrahedrally coordinated fe(iii) in ferrihydrite. *Environmental Science and Technology*, 0(ja):null, 0.

[56] T. Mairoser, A. Schmehl, A. Melville, T. Heeg, W. Zander, J. Schubert, D. E. Shai, E. J. Monkman, K. M. Shen, T. Z. Regier, D. G. Schlom, and J. Mannhart. Influence of the substrate temperature on the curie temperature and charge carrier density of epitaxial gd-doped euo films. *Applied Physics Letters*, 98(10):102110, 2011.

[57] T. Mairoser, A. Schmehl, A. Melville, T. Heeg, L. Canella, P. Böni, W. Zander, J. Schubert, D. E. Shai, E. J. Monkman, K. M. Shen, D. G. Schlom, and J. Mannhart. Is there an intrinsic limit to the charge-carrier-induced increase of the curie temperature of euo? *Phys. Rev. Lett.*, 105:257206, Dec 2010.

[58] E. M. Gullikson, R. Korde, L. R. Canfield, and R. E. Vest. Stable silicon photodiodes for absolute intensity measurements in the vuv and soft x-ray regions. *Journal of Electron Spectroscopy and Related Phenomena*, 80:313 – 316, 1996. Proceedings of the 11th International Conference on Vacuum Ultraviolet Radiation Physics.

[59] J. M. Gottfried, K. J. Schmidt, S. L. M. Schroeder, and K. Christmann. Adsorption of carbon monoxide on au(110)-(12). *Surface Science*, 536(1-3):206 – 224, 2003.

[60] Duane A. Outka and R.J. Madix. The oxidation of carbon monoxide on the au(110) surface. *Surface Science*, 179(2-3):351 – 360, 1987.

[61] B. Beden, A. Bewick, K. Kunimatsu, and C. Lamy. Infrared study of adsorbed species on electrodes: Adsorption of carbon monoxide on pt, rh and au. *Journal of Electroanalytical Chemistry and Interfacial Electrochemistry*, 142(1-2):345 – 356, 1982.

[62] B. Watts, L. Thomsen, and P.C. Dastoor. Methods in carbon k-edge nexafs: Experiment and analysis. *Journal of Electron Spectroscopy and Related Phenomena*, 151(2):105 – 120, 2006.

[63] E.A. Stern, W.T. Elam, B.A. Bunker, Kun quan Lu, and S.M. Heald. Ion chambers for fluorescence and laboratory exafs detection. *Nuclear Instruments and Methods in Physics Research*, 195(1-2):345 – 346, 1982.

[64] J. H. Hubbell, Wm. J. Veigele, E. A. Briggs, R. T. Brown, D. T. Cromer, and R. J. Howerton. Atomic form factors, incoherent scattering functions, and photon scattering cross sections. *Journal of Physical and Chemical Reference Data*, 4(3):471–538, 1975.

[65] J. H. Hubbell, H. A. Gimm, and I. Overbo. Pair, triplet, and total atomic cross sections (and mass attenuation coefficients) for 1 mev-100 gev photons in elements z=1 to 100. *Journal of Physical and Chemical Reference Data*, 9(4):1023–1148, 1980.

[66] Tetsuya Ishikawa, Yoshitaka Yoda, Koichi Izumi, Carlos Kenichi Suzuki, Xiao Wei Zhang, Masami Ando, and Seishi Kikuta. Construction of a precision diffractometer for nuclear bragg scattering at the photon factory. *Review of Scientific Instruments*, 63(1):1015 –1018, January 1992.

[67] T. T. Fister, G. T. Seidler, L. Wharton, A. R. Battle, T. B. Ellis, J. O. Cross, A. T. Macrander, W. T. Elam, T. A. Tyson, and Q. Qian. Multielement spectrometer for efficient measurement of the momentum transfer dependence of inelastic x-ray scattering. *Review of Scientific Instruments*, 77(6):063901, 2006.

[68] Emilio Gatti and Pavel Rehak. Semiconductor drift chamber an application of a novel charge transport scheme. *Nuclear Instruments and Methods in Physics Research*, 225(3):608 – 614, 1984.

[69] R. Alberti, A. Longoni, T. Klatka, C. Guazzoni, A. Gianoncelli, D. Bacescu, and B. Kaulich. A low energy x-ray fluorescence spectrometer for elemental mapping x-ray microscopy. pages 1564 –1566, oct. 2008.

[70] R. Jenkins, R.W. Gould, and D. Gedcke. *Quantitative x-ray spectrometry*. Practical spectroscopy. M. Dekker, 1995.

[71] R. Frahm. New method for time dependent x-ray absorption studies. *Review of Scientific Instruments*, 60(7):2515 –2518, jul 1989.

[72] Christina Tnshoff and HolgerF. Bettinger. Photogeneration of octacene and nonacene. *Angewandte Chemie International Edition*, 49(24):4125–4128, 2010.

[73] JohnE. Anthony. The larger acenes: Versatile organic semiconductors. *Angewandte Chemie International Edition*, 47(3):452–483, 2008.

[74] J Szczepanski and M Vala. Laboratory evidence for ionized polycyclic aromatic hydrocarbons in the interstellar medium. *Nature*, 363, 1993.

[75] Uma P. Vijh, Adolf N. Witt, and Karl D. Gordon. Discovery of blue luminescence in the red rectangle: Possible fluorescence from neutral polycyclic aromatic hydrocarbon molecules? *The Astrophysical Journal Letters*, 606(1):L65, 2004.

[76] R.G. Harvey. *Polycyclic aromatic hydrocarbons: chemistry and carcinogenicity*. Cambridge monographs on cancer research. Cambridge University Press, 1991.

[77] Hans gren, Olav Vahtras, and Vincenzo Carravetta. Near-edge core photoabsorption in polyacenes: model molecules for graphite. *Chemical Physics*, 196(1-2):47 – 58, 1995.

[78] Masatoshi Kitamura and Yasuhiko Arakawa. Pentacene-based organic field-effect transistors. *Journal of Physics: Condensed Matter*, 20(18):184011, 2008.

[79] G. Comelli, J. Stöhr, C. J. Robinson, and W. Jark. Structural studies of argon-sputtered amorphous carbon films by means of extended x-ray-absorption fine structure. *Phys. Rev. B*, 38(11):7511–7519, Oct 1988.

[80] G. Comelli, J. Stöhr, W. Jark, and B. B. Pate. Extended x-ray-absorption fine-structure studies of diamond and graphite. *Phys. Rev. B*, 37(9):4383–4389, Mar 1988.

[81] Y. Ma, F. Sette, G. Meigs, S. Modesti, and C. T. Chen. Breaking of ground-state symmetry in core-excited ethylene and benzene. *Phys. Rev. Lett.*, 63(19):2044–2047, Nov 1989.

[82] A. C. Liu and C. M. Friend. The structure and reactivity of chemisorbed aromatics: Spectroscopic studies of benzene on mo(110). 89(7):4396–4405, 1988.

[83] P. Yannoulis, R. Dudde, K.H. Frank, and E.E. Koch. Orientation of aromatic hydrocarbons on metal surfaces as determined by nexafs. *Surface Science*, 189-190:519 – 528, 1987. Proceedings of the Ninth European Conference on Surface Science.

[84] A. P. Hitchcock and C. E. Brion. Carbon k-shell excitation of c2h2, c2h4, c2h6 and c6h6 by 2.5 kev electron impact. *Journal of Electron Spectroscopy and Related Phenomena*, 10(3):317 – 330, 1977.

[85] A. P. Hitchcock, G. Tourillon, R. Garrett, and N. Lazarz. Carbon 1s excitation of azulene and polyazulene studied by electron-energy-loss spectroscopy and x-ray absorption spectroscopy. *The Journal of Physical Chemistry*, 93(22):7624–7628, 1989.

[86] F. X. Gadea, H. Köppel, J. Schirmer, L. S. Cederbaum, K. J. Randall, A. M. Bradshaw, Y. Ma, F. Sette, and C. T. Chen. Vibronic coupling and core-hole localization in k-shell excitations of ethylene. *Phys. Rev. Lett.*, 66(7):883–886, Feb 1991.

[87] Y. Ma, C. T. Chen, G. Meigs, K. Randall, and F. Sette. High-resolution k-shell photoabsorption measurements of simple molecules. *Phys. Rev. A*, 44(3):1848–1858, Aug 1991.

[88] T. Yokoyama, K. Seki, I. Morisada, K. Edamatsn, and T. Ohta. *Physica Scripta*, 41(189), 1990.

[89] I. Minkov, F. Gel'mukhanov, R. Friedlein, W. Osikowicz, C. Suess, G. Ohrwall, S. L. Sorensen, S. Braun, R. Murdey, W. R. Salaneck, and H. Agren. Core excitations of naphthalene: Vibrational structure versus chemical shifts. *The Journal of Chemical Physics*, 121(12):5733–5739, 2004.

[90] D. Hbner, F. Holch, M.L.M. Rocco, K.C. Prince, S. Stranges, A. Schll, E. Umbach, and R. Fink. Isotope effects in high-resolution nexafs spectra of naphthalene. *Chemical Physics Letters*, 415(1-3):188 – 192, 2005.

[91] Stephen G. Urquhart, Harald Ade, M. Rafailovich, J. S. Sokolov, and Y. Zhang. Chemical and vibronic effects in the high-resolution near-edge x-ray absorption fine structure spectra of polystyrene isotopomers. *Chemical Physics Letters*, 322(5):412 – 418, 2000.

[92] Michele Alagia, Chiara Baldacchini, Maria Grazia Betti, Fabio Bussolotti, Vincenzo Carravetta, Ulf Ekstrom, Carlo Mariani, and Stefano Stranges. Core-shell photoabsorption and photoelectron spectra of gas-phase pentacene: Experiment and theory. *The Journal of Chemical Physics*, 122(12):124305, 2005.

[93] A. Vollmer, O. D. Jurchescu, I. Arfaoui, I. Salzmann, T. T. M. Palstra, P. Rudolf, J. Niemax, J. Pflaum, J. P. Rabe, and N. Koch. The effect of oxygen exposure on pentacene electronic structure. *The European Physical Journal E: Soft Matter and Biological Physics*, 17:339–343, 2005. 10.1140/epje/i2005-10012-0.

[94] Adam W. Gillespie, Richard E. Farrell, Fran L. Walley, Andrew R.S. Ross, Peter Leinweber, Kai-Uwe Eckhardt, Tom Z. Regier, and Robert I.R. Blyth. Glomalin-related soil protein contains non-mycorrhizal-related heat-stable proteins, lipids and humic materials. *Soil Biology and Biochemistry*, 43(4):766 – 777, 2011. Knowledge gaps in soil C and N interactions.

[95] Jun Shi. *Growth, structural and electrical characterizations of organic thin films on Si-based substrates*. PhD thesis, University of Guelph, 2010.

[96] Y. Ma, C.T. Chen, G. Meigs, K. Randall, and F. Sette. *Phys. Rev. A*, (44):137, 1979.

[97] D A Shaw, G C King, D Cvejanovic, and F H Read. Electron impact excitation of inner-shell excited states of co. *Journal of Physics B: Atomic and Molecular Physics*, 17(10):2091, 1984.

[98] *Radiation Effects on Polymers, Copyright, ACS Symposium Series, Foreword*, chapter 0, pages i–iv.

[99] J. Wang, C. Morin, L. Li, A.P. Hitchcock, A. Scholl, and A. Doran. Radiation damage in soft x-ray microscopy. *Journal of Electron Spectroscopy and Related Phenomena*, 170(1-3):25 – 36, 2009. Radiation Damage.

[100] K. Hermann, L.G.M. Pettersson, M.E. Casida, C. Daul, A. Goursot, A. Koester, E. Proynov, A. St-Amant, D.R. Salahub, V. Carravetta, H. Duarte, C. Friedrich, N. Godbout, J. Guan, C. Jamorski, M. Leboeuf, M. Leetmaa, M. Nyberg, S. Patchkovskii, L. Pedocchi, F. Sim, L. Triguero, and A. Vela. Stobe-demon version 3.0. 2009.

[101] R. B. Campbell, J. M. Robertson, and J. Trotter. The crystal structure of hexacene, and a revision of the crystallographic data for tetracene. *Acta Crystallographica*, 15(3):289–290, Mar 1962.

[102] D. W. J. Cruickshank. A detailed refinement of the crystal and molecular structure of anthracene. *Acta Crystallographica*, 9(11):915–923, Nov 1956.

[103] D. W. J. Cruickshank. A detailed refinement of the crystal and molecular structure of naphthalene. *Acta Crystallographica*, 10(8):504–508, Aug 1957.

[104] Lars G. M. Pettersson, Ulf Wahlgren, and Odd Gropen. Effective core potential calculations using frozen orbitals. applications to transition metals. *Chemical Physics*, 80(1-2):7 – 16, 1983.

[105] *NMR Basic Principles and Progress*, volume 23. Springer Heidelberg, 1990.

[106] J. Kikuma and B. P. Tonner. Xanes spectra of a variety of widely used organic polymers at the c k-edge. *Journal of Electron Spectroscopy and Related Phenomena*, 82(1-2):53 – 60, 1996.

[107] Uwe Bergmann, Henning Groenzin, Oliver C. Mullins, Pieter Glatzel, John Fetzer, and S. P. Cramer. X-ray raman spectroscopy a new tool to study local structure of aromatic hydrocarbons and asphaltenes. *Petroleum Science and Technology*, 22(7-8):863–875, 2004.

[108] Jan M. L. Martin, Jamal El-Yazal, and Jean-Pierre Franois. Structure and vibrational spectrum of some polycyclic aromatic compounds studied by density functional theory. 1. naphthalene, azulene, phenanthrene, and anthracene. *The Journal of Physical Chemistry*, 100(38):15358–15367, 1996.

[109] M. L. M. Rocco, M. Haeming, D. R. Batchelor, R. Fink, A. Schll, and E. Umbach. Electronic relaxation effects in condensed polyacenes: A high-resolution photoemission study. 129(7):074702, 2008.

[110] J. C. Slater. Atomic shielding constants. *Phys. Rev.*, 36(1):57–64, Jul 1930.

[111] J.W. Moore, R.G. Pearson, and A.A. Frost. *Kinetics and mechanism*. Wiley-interscience publication. Wiley, 1961.

[112] J. J. Rehr and A. L. Ankudinov. Time-dependent density functional theory calculations of x-ray absorption, 2003.

[113] O. Wessely, O. Eriksson, and M. I. Katsnelson. Dynamical core-hole screening in the x-ray absorption spectra of graphite, c[sub 60], and carbon nanotubes: A first-principles electronic structure study. *Physical Review B (Condensed Matter and Materials Physics)*, 73(7):075402, 2006.

[114] C. Hub, M. Burkhardt, M. Halik, G. Tzvetkov, and R. Fink. In situ stxm investigations of pentacene-based ofets during operation. *J. Mater. Chem.*, 20:4884–4887, 2010.

[115] L. Tröger, D. Arvanitis, K. Baberschke, H. Michaelis, U. Grimm, and E. Zschech. Full correction of the self-absorption in soft-fluorescence extended x-ray-absorption fine structure. *Phys. Rev. B*, 46(6):3283–3289, Aug 1992.

[116] Atsuo Iida and Takashi Noma. Correction of the self-absorption effect in fluorescence x-ray absorption fine structure. *Japanese Journal of Applied Physics*, 32(Part 1, No. 6A):2899–2902, 1993.

[117] J. P. Crocombette, M. Pollak, F. Jollet, N. Thromat, and M. Gautier-Soyer. X-ray-absorption spectroscopy at the fe $l2,3$ threshold in iron oxides. *Phys. Rev. B*, 52(5):3143–3150, Aug 1995.

[118] Robert M. Hazen and Raymond Jeanloz. Wüstite (Fe1-x O): A review of its defect structure and physical properties. *Rev. Geophys.*, 22(1):37–46, 1984.

[119] K J GALLAGHER, W FEITKNECHT, and U MANNWEILER. Mechanism of Oxidation of Magnetite to -Fe2O3. *Nature*, 217(5134):1118–1121, mar 1968. 10.1038/2171118a0.

[120] T.Z. Regier, A. Achkar, D Hawthorn, D Peak, and J Tse. Correspondence regarding "Charge transfer to solvent identified using dark channel fluorescence-yield L-edge spectroscopy". *Nature Chemistry*, Accepted.

[121] A. J. Achkar, T. Z. Regier, E. J. Monkman, K. M. Shen, and D. G. Hawthorn. Determination of total x-ray absorption coefficient using non-resonant x-ray emission. *ArXiv e-prints*, April 2011.

[122] Malte D. Gotz, Mikhail A. Soldatov, Kathrin Maria Lange, Nicholas Engel, Ronny Golnak, Rene Knnecke, Kaan Atak, Wolfgang Eberhardt, and Emad Flear Aziz. Probing coster-kronig transitions in aqueous fe+2 solution using inverse partial and partial fluorescence yield at the l-edge. *The Journal of Physical Chemistry Letters*, 3(12):16191623, 2012.

[123] D. G. Hawthorn, K. M. Shen, J. Geck, D. C. Peets, H. Wadati, J. Okamoto, S.-W. Huang, D. J. Huang, H.-J. Lin, J. D. Denlinger, Ruixing Liang, D. A. Bonn, W. N. Hardy, and G. A. Sawatzky. Resonant elastic soft x-ray scattering in oxygen-ordered yba2cu3o6. *Phys. Rev. B*, 84:075125, Aug 2011.

[124] J. Vinson, J. J. Rehr, J. J. Kas, and E. L. Shirley. Bethe-salpeter equation calculations of core excitation spectra. *Phys. Rev. B*, 83:115106, Mar 2011.